



HAL
open science

Estimation of the radiation risk to aircrew and aircraft passengers associated with atmospheric electricity events such as terrestrial gamma ray flashes and gamma ray glows
Mélody Pallu

► **To cite this version:**

Mélody Pallu. Estimation of the radiation risk to aircrew and aircraft passengers associated with atmospheric electricity events such as terrestrial gamma ray flashes and gamma ray glows. High Energy Astrophysical Phenomena [astro-ph.HE]. Université d'Orléans, 2022. English. NNT : 2022ORLE1024 . tel-04107918

HAL Id: tel-04107918

<https://theses.hal.science/tel-04107918>

Submitted on 26 May 2023

HAL is a multi-disciplinary open access archive for the deposit and dissemination of scientific research documents, whether they are published or not. The documents may come from teaching and research institutions in France or abroad, or from public or private research centers.

L'archive ouverte pluridisciplinaire **HAL**, est destinée au dépôt et à la diffusion de documents scientifiques de niveau recherche, publiés ou non, émanant des établissements d'enseignement et de recherche français ou étrangers, des laboratoires publics ou privés.

UNIVERSITÉ D'ORLÉANS

*ÉCOLE DOCTORALE ÉNERGIE, MATÉRIAUX,
SCIENCES DE LA TERRE ET DE L'UNIVERS*

LABORATOIRE DE PHYSIQUE ET CHIMIE,
DE L'ENVIRONNEMENT ET DE L'ESPACE (LPC2E)

THÈSE présentée par :

Mélody PALLU

soutenue le : 7 juillet 2022

pour obtenir le grade de : **Docteur de l'Université d'Orléans**

Discipline/ Spécialité : Sciences de l'Univers

ESTIMATION OF THE RADIATION RISK TO AIRCREW AND AIRCRAFT PASSENGERS ASSOCIATED WITH ATMOSPHERIC ELECTRICITY EVENTS SUCH AS TERRESTRIAL GAMMA RAY FLASHES AND GAMMA RAY GLOWS

THÈSE dirigée par :

M. CELESTIN Sébastien

Professeur, Université d'Orléans

Co-encadrant :

M. TROMPIER François

Ingénieur-Chercheur, Institut de radioprotection et de sûreté nucléaire

Tuteur :

M. KLERLEIN Michel

Médecin Coordonnateur Santé au travail, Air France

RAPPORTEURS :

M. MARISALDI Martino

Professeur, Université de Bergen, Norvège

M. SMITH David

Professeur, Université de Californie, Santa Cruz, USA

Président du JURY :

M. LAURENT Philippe

Directeur de recherche, CEA, Président du jury

JURY :

M. BUFFLER Andy

Professeur, Université de Cape Town, Afrique du Sud

UNIVERSITY OF ORL ANS

LABORATOIRE DE PHYSIQUE ET CHIMIE,
DE L'ENVIRONNEMENT ET DE L'ESPACE (LPC2E)

PHD THESIS

by

M lody PALLU

Defended on: 7th July 2022

**ESTIMATION OF THE RADIATION RISK TO AIRCREW
AND AIRCRAFT PASSENGERS ASSOCIATED WITH
ATMOSPHERIC ELECTRICITY EVENTS SUCH AS
TERRESTRIAL GAMMA RAY FLASHES
AND GAMMA RAY GLOWS**

Advisor:

M. CELESTIN S bastien

Professor, University of Orl ans

Co-advisor:

M. TROMPIER Fran ois

Researcher, Institute of Radiation Protection and Nuclear Safety

Air France mentor:

M. KLERLEIN Michel

Head of Occupational Health Services, Air France

Reviewers:

M. MARISALDI Martino

Professor, University of Bergen, Norway

M. SMITH David

Professor, University of California, Santa Cruz, USA

Committee members:

M. LAURENT Philippe

Senior researcher, CEA

M. BUFFLER Andy

Professor, University of Cape Town, South Africa

Abstract

The current radiation risk assessment of flight crews is performed using software, taking into account the galactic component and intense solar energetic proton events. In the 1980s and 1990s, the discovery of high-energy events, namely gamma ray glows and terrestrial gamma ray flashes (TGFs), produced in thunderstorms have opened a new field of research called high-energy atmospheric electricity. TGFs are intense bursts of high-energy photons, mostly detected by satellite, which last approximately 100 μ s. Photon energies in TGFs and gamma ray glows can reach \sim 40 MeV. Gamma ray glows are increases of the background radiation level in thunderstorms, with longer durations, i.e., from seconds to tens of minutes, but generating much weaker photon fluxes than TGFs. Both are produced through the same basic physical processes implying runaway electrons, and named relativistic runaway electron avalanches (RREAs). They are produced between 10 and 15 km of altitude, coincident with commercial flight altitudes, raising the question of a possible additional exposure associated with these events that is not taken into account for flight crews.

In this thesis, we use a set of approaches to study this question involving different tools. The first step is to estimate theoretically radiation doses delivered by TGFs. In that purpose, numerical simulations were developed and are used to simulate the propagation of runaway electrons and photons in the Earth atmosphere. Two different production models are implemented. We show that TGF sources, namely the runaway electrons, generate high doses, approaching 1 Sv (dose value that can trigger acute radiation sickness) for both models. However, we show that these high doses are delivered in compact regions of \sim 200 m radius. Therefore, we investigate the probability for an aircraft to find itself in the electron beam of a TGF. In this purpose, we present a statistical study using satellite data and flight route data. Particularly exposed routes are cited such as the route between Atlanta

Abstract

(Georgia, USA) and Santiago (Chile) for which an aircraft is estimated to be hit by a TGF every ~ 250 years or more. Using real flight data of Air France airline, we estimate that one flight is hit every ~ 390 years or more in the whole Air France fleet. Both these estimates do not take into account evasive actions taken by pilots. The probability of such an event is therefore concluded to be weak.

Then, we present the work we performed to develop a gamma ray spectrometer to detect these events in close proximity. The performances attained: rapidity, energy span, and maximum count rate of 1 MHz show that the detector is capable to detect TGFs and gamma ray glows. In addition to these characteristics, the spectrometer is able to discriminate photons and neutrons using a pulse shape discrimination (PSD) method with the plastic scintillator, which has been tested successfully using a neutron source. Several instrumental effects are presented with solutions found to avoid them. Finally, we predict the configurations for which we are able to detect a gamma ray glow and the probability to detect a TGF during a long-duration super-pressurized balloon campaign flying at 20 km of altitude. Depending on the direction of the RREAs, a detector flying at 20 km of altitude is able to detect gamma ray glows with sources above 14 (for upward photons) and 18 km of altitude (for downward photons). Concerning TGFs, using balloon trajectories of a previous campaign we estimate that there is about a one-in-two chance to be able to detect a TGF during the same campaign.

Therefore, we expect very promising observational results in the coming years during the various balloon campaigns planned. Such measurements would bring important information that would confirm or invalidate the results presented in this thesis but also help study and understand the relation between TGFs, gamma ray glows, the interaction between thunderstorm electrical system and cosmic rays, as well as explore the runaway electron acceleration processes driving these events.

Keywords: TGFs, thunderstorm, doses, aircrew, gamma spectrometry, high energy atmospheric electrodynamic

Acknowledgments

I am very grateful to have been able to carry out this PhD and to have met all the people I have met during the last 3.5 years. For that I am going to start this PhD thesis thanking all the persons that contributed directly or indirectly to this work.

First, I would like to thank Air France for the funding of this PhD thesis. This thesis as part of an Air France employee has been very interesting and useful to discover the working of such a large company.

I would like to thank also CNES for funding the projects related to this PhD, namely OREO, STRATELEC and Stratéole-2.

I really want to thank the two reviewers of this thesis, Martino Marisaldi and David Smith, who spent some of their time on my manuscript to give me very interesting and useful comments to improve it. I thank also Philippe Laurent and Andy Buffler for being part of my committee and for the interesting discussions addressed during the defense.

I thank Michel Klerlein for taking part of my PhD supervision in Air France, and the discussions about, among other, Air France, farming, and pastry.

I thank also François Trompier for being my co-advisor for this PhD, for helping discussions about doses and detectors and being always enthusiastic about new projects.

Finally, I really thank Sébastien Célestin, my PhD advisor who always pushed me to learn and develop new skills during this PhD, always available for discussions, and opened to new ideas. It was a great pleasure for me to work and carry out this PhD with you, always in a nice working atmosphere (at the lab or eating octopus with Jimmy and Toby in the middle of the Indian Ocean before launching balloons).

I spent most of the 3.5 years in the LPC2E, which is a particularly pleasant place to work, that is why I want now to cite all my colleagues (and now friends) that I have met there.

Acknowledgments

So first, many thanks to my first colleague team, that teaches me to speak english in taking time to speak and listen to my poor english when I arrived. We spent so much funny time together, such as *gouter*, lunches, playing darts, learning french, eating pizza, playing volley, and of course playing Stick Fight. Merci à Andrea, aka Monsieur Larosa, pour s'être supportés et aidés mutuellement pendant ces 3 ans, c'était trop cool d'avoir partagé tout ça avec toi ! Thanks to Vamsee, for your happiness everyday at the lab and even after, and for your favorite french question "qu'est-ce que tu as mangé hier soir?". Merci à Matthieu, pour ta compagnie quotidienne dans le bureau avec tes chers Pikachu et Raichu, nos discussions les plus perchées et tes coups de main pour la Raspberry Pi. Also thanks to Nini, for the French Friday (or Wednesday or Thursday, depending on the day it was), and all the discussions, thanks to Anna, to be my best enemy at Stick Fight (but especially for our team against the boys) and thanks to Minna for taking care of our dear Lama!

And also many thanks to my second colleague team which has lived the ending period of my PhD with me, playing UNO and going to *l'Irlandais*. Évidemment merci à Nina, pour ne pas m'avoir laissé faire la folle toute seule dans ce labo et ailleurs, et surtout pour m'avoir supportée mentalement pendant les derniers mois de la thèse (et après) ! Merci à Gaëtane, pour toutes les soirées et sorties, les histoires de Chihiro et les potins évidemment ! Merci à Pietro, pour nous avoir cuisiné des petits plats italiens, notamment pendant les confinements avec Fede. Merci à Fede pour les moments passés quand tu étais de passage au labo entre 2 voyages. Merci aussi à Pierre, car tout est super géniaaal, mais aussi Clara, Lucas et Camille, Jérémie, Manu, Luca, Julia, Alexander, Giuseppe (et ceux que j'oublie peut-être) pour tous les moments partagés !

Un petit clin d'oeil aussi aux étudiants stagiaires avec qui j'ai pris plaisir à travailler : Abdelhamid, Lorenzo and Eugen. Et aussi à ceux que j'ai côtoyés au labo et ailleurs : Ted, Gilles, Stéphane, Bertrand, Pedro au LPC2E, Marie-Pierre et Laurence à Air France, et Éric et Delphine de l'IRSN.

Merci aussi à Camille et Élise pour leur présence pendant ces 3 ans.

Et enfin, évidemment MERCI à ma famille, Maman, Papa, Meline, Flav, Mamie (même si je ne suis toujours pas hôtesse de l'air), tous mes cousins, cousines, oncles et tantes, de m'avoir (eux aussi) supportée, dans tous les sens du terme ! Et j'ai aussi une pensée pour ceux qui ne sont plus là mais qui m'auraient sans aucun doute soutenue.



Contents

Abstract	i
Acknowledgments	iii
List of Acronyms	xi
List of Figures	xiii
List of Tables	xxiii
1 Introduction	1
1.1 Context	1
1.2 Terrestrial Gamma ray Flashes	4
1.2.1 Physical Characteristics of TGFs	5
1.2.2 Observations of TGFs	6
1.3 Gamma ray Glows	8
1.3.1 Physical Characteristics of GRGs	9
1.3.2 Observations of GRGs	10
1.4 Relativistic Runaway Electron Avalanches	11
1.5 TGF Initiation Models	14
1.5.1 Leader-Based Model (or Thermal Runaway)	14
1.5.2 Large-Scale Field Model and Relativistic Feedback	16
1.6 Radiation Assessment of Flight Crews	16
1.6.1 Cosmic Radiation Origin	17
1.6.2 Exposure Assessment	18
1.6.3 Usual Radiation Dose Values	20
1.6.4 TGF Additional Exposure	21
1.7 Ongoing projects and campaigns	22

Contents

1.7.1	OREO balloon project	22
1.7.2	Strateole-2 balloon campaigns and the project STRATELEC	22
1.7.3	Ground-based campaigns	24
1.8	Motivation and Objectives	25
2	Methods	27
2.1	Dose Calculations of Chapter 3	27
2.1.1	Introduction on Radiation Doses	28
2.1.2	Doses Calculations	28
2.2	Models used in Chapter 3	30
2.2.1	Pure Leader Model	31
2.2.2	Homogeneous Electric Field with Leader Injection Model	33
2.2.3	Photons and Secondary Electrons	36
2.3	Statistical Method used in Chapter 4	38
2.3.1	TGF Data	39
2.3.2	Flight Route Data	44
2.3.3	Probability Calculations	46
2.4	Conclusions	47
3	Estimation of Radiation Doses Associated with TGFs	49
3.1	Previous Considerations	49
3.1.1	Radiation Doses Delivered by Gamma ray Glows	50
3.1.2	Radiation Doses Delivered by Neutrons	50
3.1.3	Configuration	50
3.2	Radiation Doses Results	51
3.2.1	Electron Doses: Pure Leader Model	52
3.2.2	Electron Doses: Homogeneous Field Model	54
3.2.3	Photon Doses	58
3.2.4	Secondary Electron Doses	59
3.3	Discussion	59

3.3.1	Calculated Doses	59
3.3.2	Intensity of TGFs	61
3.3.3	Attenuation Due to the Aircraft Cabin	62
3.4	Conclusions	64
4	Risk for Commercial Flights to be Hit by a TGF	67
4.1	Context	67
4.2	Probability for an aircraft to be hit by a TGF	68
4.2.1	Randomized Routes	69
4.2.2	Air France Fleet	71
4.3	Discussion	74
4.3.1	Lower Fluence TGFs	75
4.3.2	Overestimation Made by Ignoring the TGF Altitude Dependence	75
4.4	Conclusions	77
5	Gamma ray Spectrometer: Development & First Results	79
5.1	Science Objectives	80
5.1.1	Gamma ray Glows	80
5.1.2	Terrestrial Gamma ray Flashes	81
5.2	Instrument Overview	82
5.2.1	Design Philosophy and Overview	83
5.2.2	Energy Range and Time Performances	85
5.2.3	Pulse Shape Discrimination Method for Neutron Detection	87
5.2.4	On-board Software	91
5.3	First Measurements	96
5.3.1	Measurements of Radioactive Sources	96
5.3.2	Gamma ray Measurement Features	97
5.3.3	Lightweight Balloon Measurements in Fair Weather	100
5.3.4	Instrumental Effects Caused by Very Energetic Particles	102

Contents

5.4	Conclusions	106
6	Predictions on XStorm measurements	109
6.1	Photon propagation for gamma ray glows	109
6.2	Detectability of gamma ray glows	110
6.3	Probability to detect a TGF	117
6.4	Ground-based measurements	119
6.5	Conclusions	120
7	General Conclusion	123
7.1	Summary	123
7.2	Impact of the thesis	126
7.3	Perspectives	126
	Résumé en Français	127
	Appendices	139
	A XStorm packet encapsulation	141
	Bibliography	143

List of Acronyms

ADC Analog-to-digital Converter	103
ADELE Airborne Detector for Energetic Lightning Emissions	7
AGILE Astro-Rivelatore Gamma a Immagini Leggero	6
ASIM Atmosphere-Space Interactions Monitor	6
BGO Bismuth Germanium Oxide	82
CGRO Compton Gamma Ray Observatory	4
CNES French Space Agency	22
EAS Extensive Air Shower	14
FPGA Field-Programmable Gate Array	
GBM Gamma ray Burst Monitor	39
GCR Galactic Cosmic Radiation	17
GLE Ground-Level Enhancement	18
GRB Gamma ray Burst	4
GRG Gamma ray Glow	8
IC intracloud	5
IRSN Institute for Radiological Protection and Nuclear Safety	19
ISS International Space Station	6
LOFAR Low Frequency Array	3

List of Acronyms

LPC2E Laboratoire de Physique et Chimie de l'Environnement et de l'Espace .	24
LIS Lightning Imaging Sensor	xiii
MXGS Modular X and Gamma Ray Sensor	6
OREO Observation du Rayonnement Energétique dans les Orages	22
OTD Optical Transient Detector	xiii
PPS Pulse Per Second	85
PSD Pulse Shape Discrimination	84
RREA Relativistic Runaway Electron Avalanch	11
RHESSI the Reuven Ramaty High Energy Solar Spectroscopic Imager	5
SAA South Atlantic Anomaly	39
SCR Solar Cosmic Radiation	17
SiPM silicon photomultiplier	82
SEP Solar Energetic Proton	18
STRATELEC STRatéole-2 ATmospheric ELECtricity	23
TC telecommand	95
TEB Terrestrial Electron Beam	xiii
TGE Thunderstorm Ground Enhancement	3
TGF Terrestrial Gamma ray Flash	1
TLE Transient Luminous Event	2
UTC Coordinated Universal Time	

List of Figures

1.1	Global lightning density in $\text{km}^{-2} \text{yr}^{-1}$ [Christian et al., 2003]. Calculated using the Optical Transient Detector (OTD) and Lightning Imaging Sensor (LIS) satellite data for respectively 5 and 3 years in the 1990s.	2
1.2	Terrestrial Gamma ray Flash illustration. A thunderstorm producing a TGF is represented. Gamma rays are shown in magenta, electrons in yellow, and positrons in green. Charged secondary particles follow the magnetic field line to escape the atmosphere, and can be detected far away from the TGF source – they are then called Terrestrial Electron Beams (TEBs). Credit: NASA/Goddard Space Flight Center. J. Dwyer/Florida Inst. of Technology	6
1.3	Count rate as a function of time (light curve) of a TGF detected by Fermi-GBM. Reproduced from [Briggs et al., 2010].	7
1.4	Accumulated spectrum of 289 TGFs detected by RHESSI. Spectra from Monte Carlo simulations for four different atmospheric depths, corresponding to four different production altitudes are represented in colors. The black solid line is a simulation at 15 km with runaway electrons having an initial velocity contained in a cone beam of 45° of half width, whereas runaway electrons have vertical velocities in the other models. Reproduced from [Dwyer and Smith, 2005].	9

List of Figures

1.5	Count rate as a function of the time (light curve) of three gamma ray glows detected by an X-ray spectrometer flying on a NASA Storm Hazards Project F-106 aircraft. Reproduced from [McCarthy and Parks, 1985]. The first glow has been terminated by a flash that struck near the aircraft. The second one has been terminated by a flash that stroke the aircraft. The third one has probably been totally crossed by the aircraft, not ending in association with any lightning.	10
1.6	Friction force applied on electrons during their propagation at ground level, as a function of their energy. $E_b = 2.08$ kV/cm is the break-even field and $E_c = 263$ kV/cm is the electric field for which all the electrons will run away.	12
1.7	Representation of the two main models supported for TGF initiation. For the leader based model, RREAs are initiated and developed in the inhomogeneous electric field surrounding a leader tip, represented in red on the left figure. For the homogeneous field, RREAs are initiated in the inhomogeneous electric field produced by a leader tip (in red) and then develop in the large scale electric field of the thunderstorm (red arrow). Positrons (green) propagate backwards to the start of the avalanche creating relativistic feedback and participating to produce a high number of runaway electrons.	15
1.8	Illustration of the dose calculation in SIEVERT. Reproduced from [Clairand et al., 2009].	20
1.9	Chart with usual radiation exposure level in everyday life.	21
1.10	Picture of a balloon launch during the first scientific campaign of Strateole-2. The gondola is carried by the technical teams until the balloon can carry it entirely to avoid impacts with the ground. . . .	23
2.1	Illustration of three different radioprotection quantities used in this thesis.	29

2.2 Fluence-to-dose conversion coefficients as a function of the energy, taken from the Fluka database [Pelliccioni, 2000]. The solid lines correspond to the conversion coefficients for $H^*(10)$. The three other lines correspond to different exposure geometries: anteroposterior (AP), isotropic (Iso) and from the top (Top). 30

2.3 Reproduced from Figure 3 of [Dwyer, 2003]. Maximum static electric field magnitude in air as a function of the length of the electric field region at ground level. The value of the threshold electric field E_{th} is represented with the dotted line. Above the solid line, electric fields are unstable, and cannot be maintained. Between the solid line and the dotted line, the electric field may eventually discharge. Below the dotted line, the electric field is stable. 35

2.4 Cross sections in air of the three types of collisions taken into account in the Monte Carlo code used for the gamma ray simulations [Berger et al., 2010]. 37

2.5 Illustration of the horizontal rings used to collect photons in the Monte Carlo simulation used. 38

2.6 Scheme of the difference between flat and 3D-configuration. When a particle goes through the ICRU sphere (Figure 2.1), the corresponding flat surface is an ellipse (shown in gray) with parameters a and $b = r$, where r is the ICRU sphere radius. Using the scheme, we find: $a = \frac{r}{\cos(\theta)}$. The effective area of the sphere is then: πr^2 and the effective area of the ellipse (projection on the flat surface) is: $\pi ab = \pi \frac{r^2}{\cos(\theta)}$, hence the $\frac{1}{\cos(\theta)}$ correction factor corresponding to a weight on every incoming particle. 39

2.7 Position of Fermi for each of the 2807 TGFs detected by GBM between the 26 November 2012 and 31 July 2016. 40

List of Figures

2.8	(a) Simulated Fermi trajectory for 1 day. (b) Proportion of time spent by Fermi over each surface element as a function of latitude (averaged over the longitudes).	41
2.9	TGF density map calculated from Fermi detectable TGFs.	43
2.10	Number of flights per year in the world from 2004 to 2022 [statista.com , 2021]. We choose as a reference number of flights per year the number of flights performed in 2019 (red), before the COVID-19 crisis that caused a brutal decrease in the global air traffic in 2020.	45
3.1	Representation of the configuration studied. The pink area represents the TGF. The yellow area is the location of causative RREAs. Secondary electrons are electrons produced by collisions between TGF photons and air molecules. Reproduced from [Pallu et al., 2021]. . .	51
3.2	2-D cross-sectional view of the calculated ambient dose equivalent associated with runaway electrons producing a TGF, obtained within pure leader model. The leader tip is represented as a red diamond. The dashed lines are isocontours at 1, 6, and 20 mSv. Reproduced from [Pallu et al., 2021].	53
3.3	Energy spectrum of the RREA electrons contained in the 15-m diameter disk, 50 meters above the source. Reproduced from [Pallu et al., 2021].	53

3.4 Representation of the calculated ambient dose equivalent for electrons, within a homogeneous electric field model. The electric field value corresponds to: (A) 4 kV cm^{-1} and (B) 5 kV cm^{-1} at ground level. The dashed lines represent $H^*(10)$ isocontours. (Panels A.1 and B.1) Dose produced at the end of a 1-km avalanche, at an altitude of 13 km, as a function of the electron beam diameter at the end of the avalanche. (Panels A.2 and B.2) Dose produced inside the avalanche as a function of the electron beam diameter at the end of the avalanche. The black and striped area represents a non-physical situation considering the minimum diffusion diameter of a point source. (Panels A.3 and B.3) Dose as a function of the altitude inside the avalanche for a point source that ends with (A) a 130-m diameter and (B) a 107-m diameter, represented with a magenta line in panels A.2 and B.2. The avalanche length λ and the initial number of runaway electrons N_0 are, respectively, (A) 249 meters and $6 \cdot 10^{16}$ electrons, and (B) 138 meters and $4.1 \cdot 10^{15}$ electrons. Reproduced from [Pallu et al., 2021]. 55

3.5 2-D representation of the calculated ambient dose equivalent for runaway electrons accelerated in a homogeneous electric field region, assuming a point source, to illustrate the electron beam diffusion. The dose is thus shown as constant with the radial distant. (a) The electric field value is 4 kV cm^{-1} at ground level. The minimum dose delivered is 1.4 Sv. The dose at the end of the avalanche region is 7 Sv. (b) The electric field value is 5 kV cm^{-1} at ground level. The minimum dose delivered is 0.3 Sv. The dose at the end of the avalanche region is 18 Sv. The colorbar is the same for both plots and goes from 0.1 to 20 Sv. Reproduced from [Pallu et al., 2021]. 56

List of Figures

3.6	Ambient doses equivalent generated by photons as a function of the observation altitude and the radial distance. The red diamond is the position of the photon source, localized at 12 km of altitude. The maximum dose is reached at the closest point to the source region and reaches 90 μSv . Reproduced from [Pallu et al., 2021].	58
3.7	Attenuation of the electron dose by the cabin within the pure leader model, with the observation 50 m above the source (blue) and 100 m above the source (magenta). The calculation is made by subtracting 2 MeV from each electron. Electrons with energies lower than 2 MeV are simply removed as they stop in the aircraft's skin. Reproduced from [Pallu et al., 2021].	64
4.1	Representation of the calculated time (in years) separating two hits of aircraft by a TGF on each Air France routes; these results are plotted above the TGF density map presented in Figure 2.9.	70
4.2	Representation of the location of all in-flight Air France aircraft at the time of the detection of a TGF. The TGF plotted has been detected on the 22nd of July, 2015. The green stars represent the location of aircraft. The blue lines are the routes of the aircraft concerned. The red star (hidden by a green star) is the location of the TGF. The shortest distance between an aircraft and the TGF is 36 km.	72
4.3	Histogram of distances between a TGF and aircraft in flight at the time of the TGF. A total of 55,795 flights are used to calculate this histogram.	73
4.4	Time (in years) separating two hits of aircraft by a TGF on Air France routes.	74

4.5	Illustration of the events configuration. The proportion of the red hatched area of the light grey square corresponds to the probability that an aircraft is hit by a TGF, given that both are in the range 10-12 km. The magenta area corresponds to the area where the aircraft is constrained to be above the TGF. The dark grey area corresponds to the area where the aircraft is above but too far (>1 km) above the aircraft.	77
5.1	XStorm adapted for Strateole-2 campaign (mechanical, communication and power interfaces)	83
5.2	Spectrum acquired in 4 hours, at ground level, in Orléans, France. Three gamma ray lines from the background have been identified and used for the energy calibration: potassium 40 at 1.462 MeV, bismuth 214 at 2.204 MeV and thallium 208 at 2.615 MeV.	86
5.3	Integral calculations with the plastic channel. The first integral is calculated between 0 and 0.1 μ s and the second one is calculated between 0.1 and 1 μ s. This is made to perform the Pulse Shape Discrimination.	89
5.4	PSD representation that allows to discriminate neutrons from gamma rays. Data have been obtained with XStorm exposed to a neutron source (Californium ²⁵² Cf).	89
5.5	Simulation of neutron and gamma ray pulses. (a) PSD representation that allows to discriminate neutrons from gamma rays. (b) PSD representation, with addition of the two thresholds discussed in Section 5.2.3. Both representations have been obtained by simulating pulses with decay times of 240 ns and 360 ns, different amplitudes and a Poisson noise.	91

List of Figures

5.6	Illustration of the two working modes implemented, mainly to fly with balloons using satellite communication link. In the event mode, the detector type is indicated: plastic (detector 1) and BGO (detector 2).	92
5.7	Duration between two false positives Δt as a function of the threshold k and the radiation background R for (a) TGFs ($\tau = 100 \mu\text{s}$) and (b) gamma ray glows ($\tau = 1 \text{ s}$). The red dashed line corresponds to 1 month.	94
5.8	Illustration of a triggered gamma ray glow (simulated data). The blue shaded part corresponds to triggered counts. The green shaded part corresponds to the counts that are recorded and sent to the ground. The duration of the green part can be modified with a telecommand during the flight.	95
5.9	Energy spectra acquired with different radioactive sources. The expected gamma ray lines are shown by black dashed lines. An explanation concerning the “additional” lines than those specified is given in the text.	98
5.10	Energy spectra as a function of the temperature, with the use of the temperature correction function for the SiPM gains.	99
5.11	Measured energy of a pulse as a function of the count frequency. Pulses used are identical and generated by a pulse generator. The energy is attenuated from count frequency of $\sim 100 \text{ kHz}$.	100
5.12	Number of particles detected by XStorm as a function of time during a lightweight balloon in fair weather. The balloon has been launched on the 7th October, 2021 at Aire-sur-l’Adour (France).	101
5.13	XStorm lightweight balloon launch in fair weather.	101

5.14 Number of counts ($/s/cm^2$) with energy >1 MeV detected by XStorm as a function of altitude (green). The black line corresponds to a moving average calculated over a 15-min range. The red dashed line represents the count rate estimations made with EXPACS, taking into account gamma rays, electrons, positrons and protons (>1 MeV). 103

5.15 Instrumental effect detected during a balloon flight with XStorm. 104

5.16 Representation of the PSD on the BGO scintillator channel during a balloon flight. Black points represent “normal” counts. Green stars represent the counts generated by instrumental effects. Inequality 5.5, represented in red, is defined as the limit between “normal” and “instrumental” counts. 105

6.1 Proportion of photons that reach a given altitude (or ratios of photon fluxes observed at various altitudes to fluxes at the source in the case of an infinite source plane. The source is set at different altitudes between 1 and 20 km, with initial photon velocities directed upward (black triangles). 111

6.2 Proportion of photons that reach a given altitude (or ratios of photon fluxes observed at various altitudes to fluxes at the source in the case of an infinite source plane. The source is set at different altitudes between 1 and 20 km, with initial photon velocities directed downward (black triangles). 112

6.3 Simulation of a RREA with photon production in real time. The position of electrons and photons are plotted respectively in blue and red. The stationary photon flux at 14.1 km is reached within less than $5 \mu s$. In this simulation, the photons do not undergo collisions, hence photon flux observed above 14.1 km is constant. 115

List of Figures

6.4	Same as Figures 6.1 and 6.2 with upward (left) and downward (right) initial velocities for photons. Only the XStorm detectable glow configurations are filled, using the threshold calculation method presented in Section 5.2.4 and the background radiation level determined by EXPACS and fair weather balloon flights at Aire-sur-l'Adour (France). The glow used as a reference is the glow detected and described in Kelley et al. [2015].	118
6.5	Detectability of [Kelley et al., 2015]-like gamma ray glows for ground-based detections, depending on the source altitude and the observation site altitude.	120
A.1	Packet encapsulation format of the data produced by XStorm.	142

List of Tables

4.1	Table of probability for an aircraft to be hit by a TGF according to its flight type	71
5.1	Performances of the gamma ray spectrometer.	85

Introduction

Key Points

- Presentation of the high-energy events addressed in this thesis: terrestrial gamma ray flashes and gamma ray glows
- Presentation of the current assessment method for flight crew radiation exposure
- Presentation of research questions and objectives of the present thesis

The general context of research on lightning and related events is introduced in the first section. A presentation of Terrestrial Gamma ray Flashes (TGFs) is given in the second section, followed with the presentation of gamma ray glows in the third section. Physical processes leading to the production of these high-energy events and current proposed models are described in Section 1.4 and Section 1.5. In Section 1.7, we present the projects in which we are involved at the institute LPC2E related to TGF and gamma ray glow measurements. The current flight crew radiation assessment and the question of possible additional exposure due to TGFs is presented in Section 1.6. Finally, the motivation and the objectives of this work are presented in the last section of this chapter.

1.1 Context

Thunderstorms are atmospheric perturbations produced by the largest cloud type in terms of vertical extension, namely cumulonimbus. The latter can extend from several hundreds of meters from the ground, up to the tropopause (or even slightly

Chapter 1. Introduction

above). These dense clouds are associated with heavy rain or hail, strong winds, thunder, and lightning. Lightning density is defined as the number of lightning per unit time per unit area. This quantity is highly variable in space and time. The variability in space depends on the latitude, but also on the ground type below the storm (ocean or continent). The variability in time depends on the year, but also on smaller scales as the local season and time. A global map of total lightning flash density in $\text{km}^{-2} \text{yr}^{-1}$ is presented in Christian et al. [2003] (reproduced in Figure 1.1). The highest lightning densities are present at low latitudes above land masses. The mean number of lightning on Earth estimated from these data is 45 s^{-1} with an estimated uncertainty of $\pm 5 \text{ s}^{-1}$.

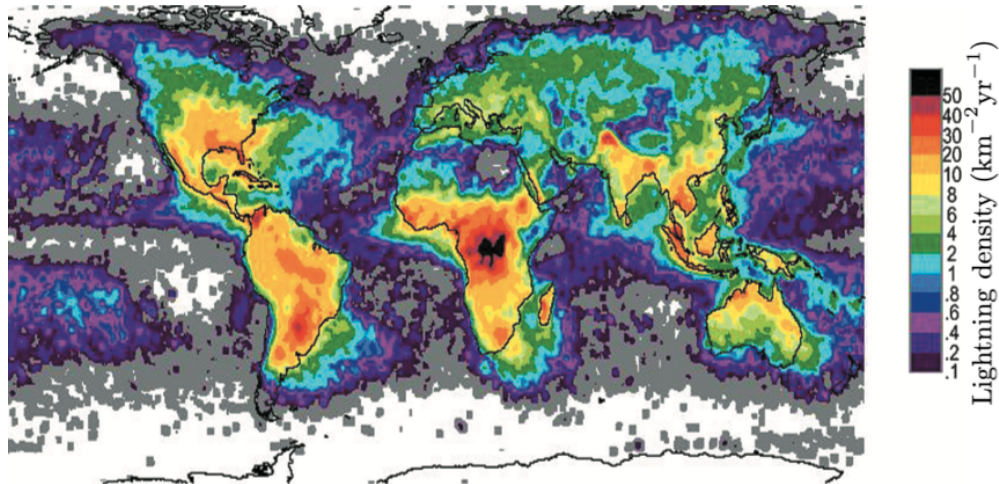


Figure 1.1: Global lightning density in $\text{km}^{-2} \text{yr}^{-1}$ [Christian et al., 2003]. Calculated using the Optical Transient Detector (OTD) and Lightning Imaging Sensor (LIS) satellite data for respectively 5 and 3 years in the 1990s.

Thunderstorms have been found to be responsible for peculiar electrical events, such as Transient Luminous Events (TLEs). TLEs had been predicted in the 1920s by Wilson [1924], concluding that large thunderstorms should produce electrical breakdown in the upper atmosphere. TLEs are a family of electrically induced forms of brief luminous plasma occurring between 40 and 100 km of altitude. Sprites are the most commonly observed, and have usually a reddish color, but other events called elves, blue jet, and gigantic jet also belong to this group.

Thunderstorms and lightning have also been detected over several decades on other planets of the Solar System [Yair et al., 2008] (especially on Jupiter and Saturn). The main evidence of lightning activity are optical emissions detected by cameras on-board spacecraft of the intense light emitted by the discharges. Indirect proof from electromagnetic measurements such as high frequency (HF) or low frequency (LF) emissions are also used to study extraterrestrial lightning. For instance, Voyager 1 was the first spacecraft to detect lightning optically on Jupiter [Cook et al., 1979], and thousands of sferics have been detected on Saturn by the instrument RPWS on Cassini [Gurnett et al., 2005; Fischer et al., 2006]. More recently, Juno detected optical emissions with its highly sensitive, visible wavelength camera called Stellar Reference Unit and Becker et al. [2020] estimated the lightning density on Jupiter to be $6.1 \cdot 10^{-2}$ flashes/km²/yr. Radio-telescopes such as the Low Frequency Array (LOFAR) are used to detect radio emissions on the gas giants from Earth (e.g., [Zarka et al., 2004]).

On Earth, Terrestrial Gamma ray Flashes (TGFs) have been first reported in 1994. They are flashes of high-energy photons [Fishman et al., 1994]. They are composed of high-energy photons in the gamma ray range ($\gtrsim 100$ keV) and are therefore not visible. Finally, gamma ray glows, also called Thunderstorm Ground Enhancements (TGEs) (e.g., [Chilingarian, 2011]) when observed from the ground, are other high-energy events produced in thunderstorms, observed as enhancements of the radiation background level. They are believed to be driven by the same acceleration mechanism as TGFs, or also by a mechanism based on the Modification Of the energy Spectra of cosmic rays by the thundercloud electric field, called the MOS mechanism [Chilingarian et al., 2012]. TGFs and gamma ray glows are the two types of events addressed in this thesis. Details in physical processes behind the production of those phenomena are still up for debate, but it has been showed that the multiplication and acceleration of electrons at relativistic velocities in the electric field of thunderstorms along with a bremsstrahlung emission producing gamma rays, explain the continuous energy spectra measured from these events

[Dwyer and Smith, 2005].

In 2010, Dwyer et al. was the first to estimate the radiological risk associated with TGFs for aircraft passengers. Indeed, the altitude ranges of the TGF sources and commercial flights overlap. In that study, Dwyer et al. [2010] showed that depending on the radius of the runaway electron beam, radiation doses delivered by TGF sources might approach or even exceed usual regulatory annual limits. These results call for precise assessment of the radiological risk associated with these high-energy events.

1.2 Terrestrial Gamma ray Flashes

TGFs are bursts of high-energy photons produced in thunderstorms (see illustration in Figure 1.2). They have been discovered in 1994 [Fishman et al., 1994] with the Compton Gamma Ray Observatory (CGRO). CGRO was a NASA space observatory dedicated to high-energy astrophysics. One of its instrument, BATSE, was in particular dedicated to the study of Gamma ray Bursts (GRBs) from deep space, but in 1991 BATSE detected gamma ray emissions coming from the Earth atmosphere. It was the first reported detection of a TGF. They appeared from the start to be related to thunderstorm activity and opened a new field of research crossing over high-energy physics, astrophysics, plasma physics, and atmospheric physics.

The terminology used in this manuscript for the terms *gamma rays* and *X-rays* follows the terminology used in the high-energy atmospheric electricity community, that is the same as in the high-energy astrophysics community. Indeed, the difference between *gamma rays* and *X-rays* is usually based on the source type. *X-rays* are usually defined as electromagnetic radiation with energy greater than ~ 1 keV, produced by the acceleration or deceleration of charged particles (called bremsstrahlung) and by electronic transitions in the deep layers of atoms, while *gamma rays* are usually assumed to come from nuclear transitions. In this thesis, *gamma rays* are defined as photons with energy greater than ~ 1 MeV, regardless of the source type.

1.2.1 Physical Characteristics of TGFs

Single TGF photons have energies from tens of keV to ~ 40 MeV [Briggs et al., 2010; Marisaldi et al., 2010]. TGFs are violent events that produce a number of 10^{18} photons on average. This number was estimated from satellite measurements (e.g., [Gjesteland et al., 2015; Mailyan et al., 2016, 2019]). They have a short duration, as they last less than 1 ms [Fishman et al., 2011; Marisaldi et al., 2015]. A light curve of a TGF detected by Fermi-GBM is represented in Figure 1.3. Their origin has been discussed for a long time, but we now know that TGF detected from space are associated with a common type of lightning discharges, namely normal polarity intracloud (IC) discharges that transport negative charges upward (+IC) [Stanley et al., 2006; Lu et al., 2010; Shao et al., 2010; Lu et al., 2011; Cummer et al., 2015]. However, their exact production mechanism remains uncertain. The main models proposed nowadays are presented in Section 1.5. The first TGF energy spectrum was built accumulating counts from 289 TGF detections by the Reuven Ramaty High Energy Solar Spectroscopic Imager (RHESSI) satellite [Dwyer and Smith, 2005]. It is shown in Figure 1.4. From this spectrum, TGFs have been estimated to be produced at thunderstorm altitudes, particularly between 10 and 15 km of altitude. The associated discharges emit radio atmospheric signals, called sferics, and it is possible to localize their origin with detection networks, and using detailed measurements (ionospheric reflections) it is possible to estimate TGF source altitudes (e.g., [Cummer et al., 2014, 2015]).

Because of the high energies involved, TGFs have been predicted to be able to trigger atmospheric photonuclear reactions producing neutrons and radionuclides [Babich, 2006; Carlson et al., 2010; Dwyer et al., 2015]. Observations of neutrons coincident with lightning [Bowers et al., 2017] and measurements of TGF afterglows from the positron annihilation peak at 511 keV [Enoto et al., 2017; Rutjes et al., 2017; Wada et al., 2019] have confirmed cases of neutron and positron production by TGFs. Finally, positrons produced by TGFs were first reported by Fermi

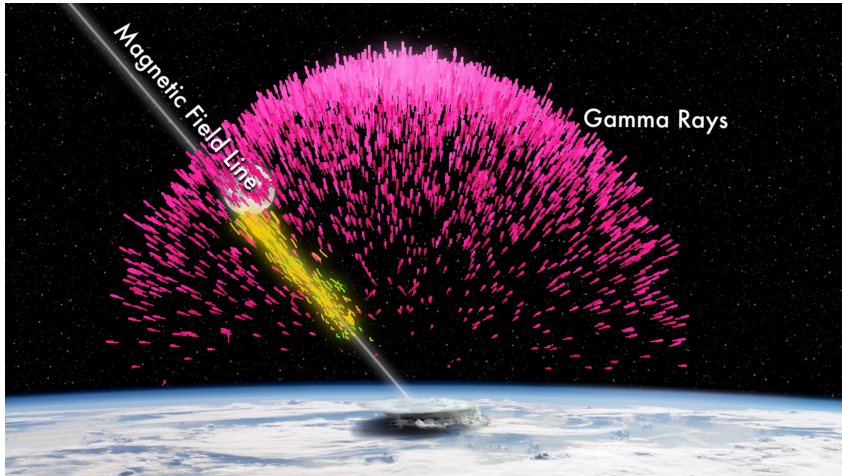


Figure 1.2: Terrestrial Gamma ray Flash illustration. A thunderstorm producing a TGF is represented. Gamma rays are shown in magenta, electrons in yellow, and positrons in green. Charged secondary particles follow the magnetic field line to escape the atmosphere, and can be detected far away from the TGF source – they are then called Terrestrial Electron Beams (TEBs). Credit: NASA/Goddard Space Flight Center. J. Dwyer/Florida Inst. of Technology

[Briggs et al., 2011], but it is worth mentioning that those ones were not due to photonuclear reactions, but were produced by pair production reactions.

1.2.2 Observations of TGFs

Different types of TGF observations have now been performed. TGFs have been detected first and are still mostly detected by satellite. Instruments on board CGRO [Fishman et al., 1994] (NASA), RHESSI [Smith et al., 2005] (NASA), Astro-Rivelatore Gamma a Immagini Leggero (AGILE) [Marisaldi et al., 2010] (Italian Space Agency) and Fermi [Briggs et al., 2010] (NASA) have detected several hundreds of TGFs each whereas it was not in their initial aims. More recently, the Atmosphere-Space Interactions Monitor (ASIM) (ESA) has been installed on the International Space Station (ISS) in 2018 and is the first space instrument designed to detect and study electricity atmospheric events with especially the Modular X and Gamma Ray Sensor (MXGS) instrument that was designed to detect TGFs. ASIM already detected 217 TGFs in the first 10 months [Østgaard et al., 2019b].

1.2. Terrestrial Gamma ray Flashes

Satellite observations have shown a flux of $\lesssim 1$ photon/cm² (e.g., [Briggs et al., 2010; Lindanger et al., 2021]) at low orbit altitudes (~ 500 km), and have been used to estimate that the number of photons produced at the source should be $\sim 10^{18}$ (e.g., [Gjesteland et al., 2015; Mailyan et al., 2016, 2019]).

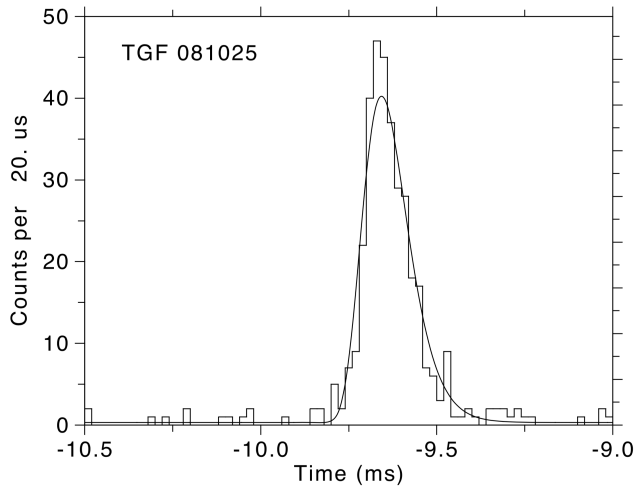


Figure 1.3: Count rate as a function of time (light curve) of a TGF detected by Fermi-GBM. Reproduced from [Briggs et al., 2010].

In addition to satellite measurements, two observations have been made on-board aircraft during the Airborne Detector for Energetic Lightning Emissions (ADELE) campaign [Smith et al., 2011a; Bowers et al., 2018]. For the first one, the aircraft accidentally flown toward the convective core of a thunderstorm. Finally, the number of ground-based detections has increased rapidly since the discovery of downward TGFs, for which the photon beam is directed downward. Downward TGFs have the advantage to be observable from the ground, and therefore offer the possibility for one event to be detected across several detectors [Dwyer et al., 2004, 2012; Abbasi et al., 2017, 2018; Belz et al., 2020]. These multipoint measurements allow to better study the spatial and temporal shape of TGFs [Berge and Celestin, 2019], that is not accessible with a single point measurement from a satellite or an aircraft. Indeed, TGF geometry is still an open question. The opening angle of the photon beam, the beam axis direction as well as the presence of a tilt for the beam axis

Chapter 1. Introduction

are still unknown parameters, although spectra and detection distances relative to their sources tend to point to a wide beam geometry (e.g., [Hazelton et al., 2009; Gjesteland et al., 2011; Mailyan et al., 2016, 2019; Lindanger et al., 2021]).

Firstly supposed to be rare events, TGFs are indeed quite frequent globally as their occurrence rate is estimated to be 400,000 per year [Briggs et al., 2013] (only for those events observable by Fermi-GBM, i.e., considering only events fluent enough to be detected from low Earth orbit). Indeed, the detection is not only limited by the capacity to the TGF photons to escape the atmosphere up to low Earth orbits, but it is also presumably limited by the detection sensitivity of spaceborne instruments. Using Fermi and RHESSI TGF data, Østgaard et al. [2012] estimated the ratio of IC lightning discharges that produce such detectable TGFs to be 2%, and that we cannot exclude the fact that all lightning could produce TGFs however too dim to be detectable from satellite. Dim TGF research have been undertaken, for instance Smith et al. [2014], McTague et al. [2015], Østgaard et al. [2015], Smith et al. [2016] and Albrechtsen et al. [2019] have searched for photon counts detected by spaceborne instruments statistically correlated to ground-based IC lightning detection. The results of these studies do not conclude unequivocally on the proportion of weak TGFs as it depends on the satellite and the ground-based lightning detection network used, but in principle, it could increase the known occurrence frequency of TGFs.

1.3 Gamma ray Glows

Gamma ray Glows (GRGs) are enhancements of the background radiation level in thunderstorms. They have been first reported by McCarthy and Parks [1985]. An example of their detection of three gamma ray glows is presented in Figure 1.5.

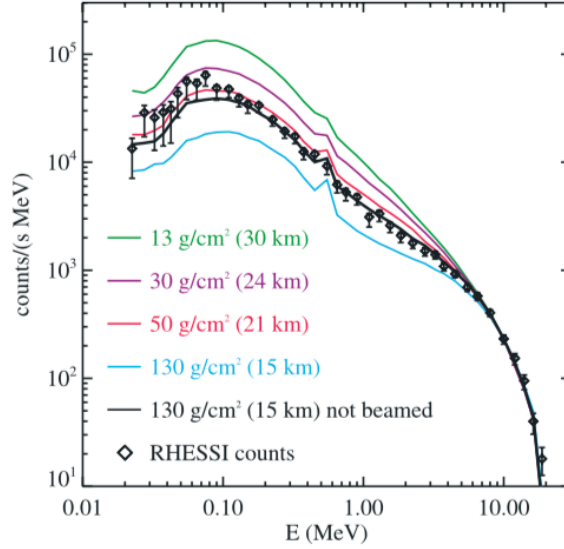


Figure 1.4: Accumulated spectrum of 289 TGFs detected by RHESSI. Spectra from Monte Carlo simulations for four different atmospheric depths, corresponding to four different production altitudes are represented in colors. The black solid line is a simulation at 15 km with runaway electrons having an initial velocity contained in a cone beam of 45° of half width, whereas runaway electrons have vertical velocities in the other models. Reproduced from [Dwyer and Smith, 2005].

1.3.1 Physical Characteristics of GRGs

GRGs are described as enhancements of the background radiation as they are less fluents than TGFs but have longer durations, usually from several seconds to tens of minutes. They are often studied together with TGFs since their energy spectrum is similar [Kelley et al., 2015], and therefore they have been thought to be driven by the same physical processes as TGFs [Tsuchiya et al., 2007; Tsuchiya et al., 2011], described in Section 1.4. As opposed to TGFs, production of glows have not been found to be positively correlated to lightning leaders. Only one case was reported by Eack et al. [1996] for which a lightning flash turned back on a glow previously terminated by a first lightning flash. Indeed, they are often terminated by lightning leaders discharging the electric field in the thunderstorm. This was the case for the two firsts glows presented in Figure 1.5.

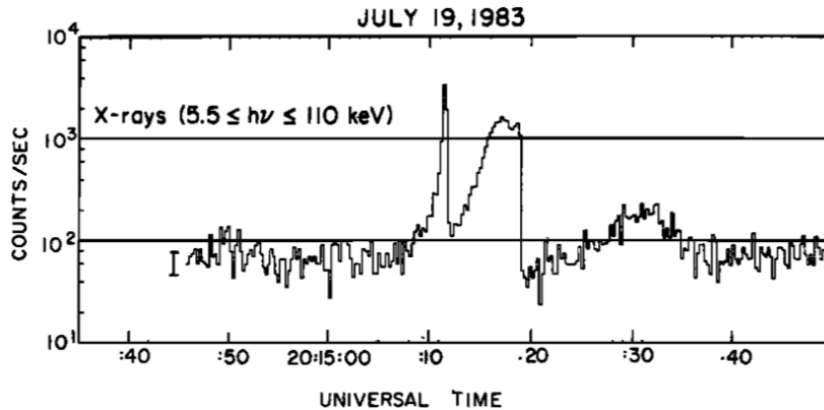


Figure 1.5: Count rate as a function of the time (light curve) of three gamma ray glows detected by an X-ray spectrometer flying on a NASA Storm Hazards Project F-106 aircraft. Reproduced from [McCarthy and Parks, 1985]. The first glow has been terminated by a flash that struck near the aircraft. The second one has been terminated by a flash that stroked the aircraft. The third one has probably been totally crossed by the aircraft, not ending in association with any lightning.

1.3.2 Observations of GRGs

Corresponding to lower fluxes, GRGs cannot be detected by satellite, and are usually detected with *in situ* measurements, either with balloons, aircraft, or ground-based measurements at high altitude. The measurement presented in Figure 1.5 has been realized on board an aircraft, such as the one discussed in Kelley et al. [2015] detected during the ADELE campaign mentioned in the previous section. Eack and Beasley [2015] have presented GRG measurements made in 1995 with balloon flights. Electric field measurements have also been performed simultaneously with X-ray measurements on this balloon flight. These data help to show precisely the link between the end of the glow and the brutal decrease of the electric field in the thunderstorm due to a lightning flash. In some special configurations, gamma ray glows can be detected from the ground and are sometimes called TGEs. This is the case mostly for high altitudes location where the thunderstorms are nearer from the ground. In the Aragats high-altitude station in Armenia, Chilingarian et al. [2019] reported more than 100 TGEs detected in 2007. Glows can also be detected

1.4. Relativistic Runaway Electron Avalanches

on the ground in Japan, where a special climate (e.g., [Takeuti et al., 1973; Goto and Narita, 1992; Rakov and Uman, 2007]) produce thunderstorms at very low altitudes, namely hundreds of meters from the ground [Goto and Narita, 1992]. Wada et al. [2019] for instance have detected a gamma ray glow with their ground-based gamma ray detectors distributed in several locations in Japan. They also reported the detection of a downward TGF at the end of the gamma ray glow, at the same time as a lightning discharge.

Gamma ray glows are assumed to be initiated by the cosmic ray background. Indeed, a high number of energetic particles called cosmic rays propagate through the atmosphere coming from the Sun, from outside of the Solar System in our own galaxy, and from distant galaxies. Electrons and positrons produced by their interaction with air molecules can then become seed particles of Relativistic Runaway Electron Avalanches (RREAs), as explained in more details in Section 1.4.

Gamma ray glows are estimated to be more frequent than TGFs. Kelley et al. [2015] conservatively estimated that more than 8% of the storms produce glows. Firstly supposed to be detected mainly in the close vicinity of thunderstorms, a gamma ray glow has been detected recently at 20 km of altitude, therefore several kilometers above the thunderstorm, by Østgaard et al. [2019a], which raises new questions about the production location and the detectability of these events.

1.4 Relativistic Runaway Electron Avalanches

Despite the remaining uncertainty on the complete set of physical processes producing TGFs and gamma ray glows, the energy spectrum shown in Figure 1.4 strongly suggests that they both originate as bremsstrahlung emission from RREAs. Indeed, the spectrum from bremsstrahlung emissions consists of a continuous spectrum of gamma rays, similar to Figure 1.4. Bremsstrahlung consists of the emission of photons by a charged particle, namely an electron, due to its acceleration or deceleration when deflected by other charged particles. The spectra in Figure 1.4 is

Chapter 1. Introduction

also characterized by an exponential high-energy cutoff, at ~ 7 MeV. This energy cutoff is theoretically explained by the presence of Relativistic Runaway Electron Avalanches (RREAs) in large-scale homogeneous electric fields (e.g., [Roussel-Dupré and Gurevich, 1996; Dwyer and Babich, 2011; Dwyer et al., 2012; Celestin et al., 2012; Cramer et al., 2014]).

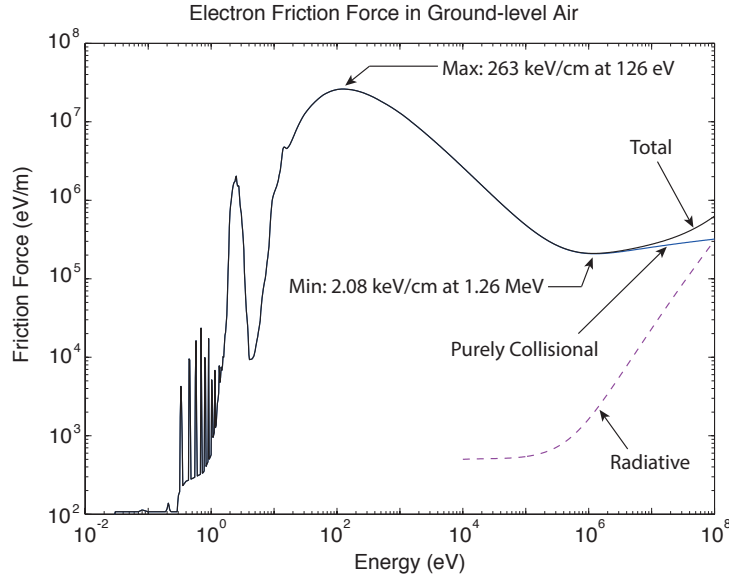


Figure 1.6: Friction force applied on electrons during their propagation at ground level, as a function of their energy. $E_b = 2.08$ kV/cm is the break-even field and $E_c = 263$ kV/cm is the electric field for which all the electrons will run away.

Electrons propagating in a medium such as the Earth atmosphere undergo a friction force that slows them down, due to collisions with air molecules. This friction force at ground level can be calculated from the collisional cross sections and the corresponding energy loss. It is represented as a function of the energy of the electron in Figure 1.6. The maximum at 126 eV usually prevents low-energy electrons from reaching high energies. However, the friction has a minimum for energies of ~ 1 MeV, which implies that electrons in this energy range, exposed to a sufficiently strong electric field in a thunderstorm would gain more energy through the electric field than that they lose to collisions propagating in the atmosphere. These electrons would therefore continuously accelerate. These accelerating elec-

1.4. Relativistic Runaway Electron Avalanches

trons have been named *runaway electrons*. Thunderstorms usually produce electric fields with amplitudes typically lower than or reaching $2 N/N_0$ kV cm⁻¹, where N is the local air density and N_0 is the air density at ground level (e.g., [Marshall et al., 1995]). The electric field magnitude threshold to produce runaway electrons in air, sometimes called the break-even field and visible in Figure 1.6, is:

$$E_b = 2.1 \text{ kV cm}^{-1} \times N/N_0 \quad (1.1)$$

However, simulations have shown that due to elastic scattering, the field required for runaway electrons to propagate over large distances is actually higher [Dwyer, 2003]:

$$E_{th} = 2.84 \text{ kV cm}^{-1} \times N/N_0 \quad (1.2)$$

Some measurements (e.g., [Marshall et al., 1995]) have confirmed amplitudes reaching E_{th} in thunderstorms, and therefore the possibility to produce runaway electrons. Once created, runaway electrons keep accelerating, and still experience collisions with Earth atmosphere molecules. These collisions produce secondary electrons, that are mainly low-energy electrons, but a small fraction of these secondary electrons have an energy sufficient to be accelerated by the electric field and also become runaway electrons. The principle of this avalanche multiplication of runaway electrons was proposed by Gurevich et al. [1992] and is now called Relativistic Runaway Electron Avalanch (RREA). The flux of runaway electrons at the altitude z in the avalanche can be written:

$$F_{RREA} = F_0 \exp(z/\lambda) \quad (1.3)$$

where F_0 is the flux of seed electrons and λ is the avalanche length. Coleman and Dwyer [2006] showed that for electric field greater than 3 kV cm⁻¹:

$$\lambda(E) \approx \frac{7.3 \text{ MV}}{E - 2.76 \text{ kV cm}^{-1} \times N/N_0} \quad (1.4)$$

where E is the electric field. After some avalanche lengths, a steady state is

reached by the energy spectrum f_{re} of the runaway electrons and is described by [Dwyer et al., 2012]:

$$f_{re}(\varepsilon) = \frac{F_{RREA}}{7.3 \text{ MeV}} \exp\left(\frac{-\varepsilon}{7.3 \text{ MeV}}\right) \quad (1.5)$$

On average, runaway electrons propagate at a relativistic speed of $\sim 0.89c$ [Coleman and Dwyer, 2006], with c that is the speed of light.

1.5 TGF Initiation Models

Theoretically, an electric field stronger than the maximum of the curve in Figure 1.6, can cause all the electrons to run away and create the avalanche. They are called *thermal runaway electrons*. However, such field magnitudes cannot be sustained for long durations. Some initial high-energy electrons are needed to seed RREAs over long timescales. High-energy electrons of cosmic ray showers could have been the seeds to explain the production of RREA, but for TGFs, the number of seed electrons needed is not sufficient even if considering Extensive Air Showers (EASs) [Dwyer, 2008]. Even though the RREA mechanism has been proved to be part of the process leading to TGFs and glows, two main theories are usually put forward to explain the initiation of RREAs with a number of electrons sufficient to generate TGFs. They are presented below and a representation of each model is given in Figure 1.7. Note that these models are not mutually exclusive and could act in concert.

1.5.1 Leader-Based Model (or Thermal Runaway)

The first model is based on the direct production of thermal runaway electrons in the strong inhomogeneous electric field in the vicinity of a lightning leader tip [Moss et al., 2006; Celestin and Pasko, 2011; Celestin et al., 2015]. More precisely, plasma filaments (named streamers) surrounding the lightning leader tip generate an electric field sufficiently strong to produce thermal runaway electrons. The RREAs

1.5. TGF Initiation Models

would then develop in the field produced by the leader. This model assumes that the potential difference between the leader tip and the ambient electric field of the thunderstorm is high enough to lead to energies consistent with TGFs. After the first thermal electrons are accelerated up to energies of several tens of keV, they can be further multiplied and accelerated to form RREAs. The electric field produced by a leader tip must be greater than the threshold electric field E_{th} to allow RREAs to initiate and develop.

This model is supported by comparing observations of TGFs with lightning detection networks, that demonstrate the strong time correlation between the detected TGF and the corresponding lightning. However, it has not been demonstrated to be able to fully explain all the features of observed radio emissions yet, but promising recent studies show that the acceleration configuration assumed in this model is not inconsistent with low-frequency emissions and can in fact accurately reproduce peculiar signals named slow LF pulses [Berge et al., 2022].

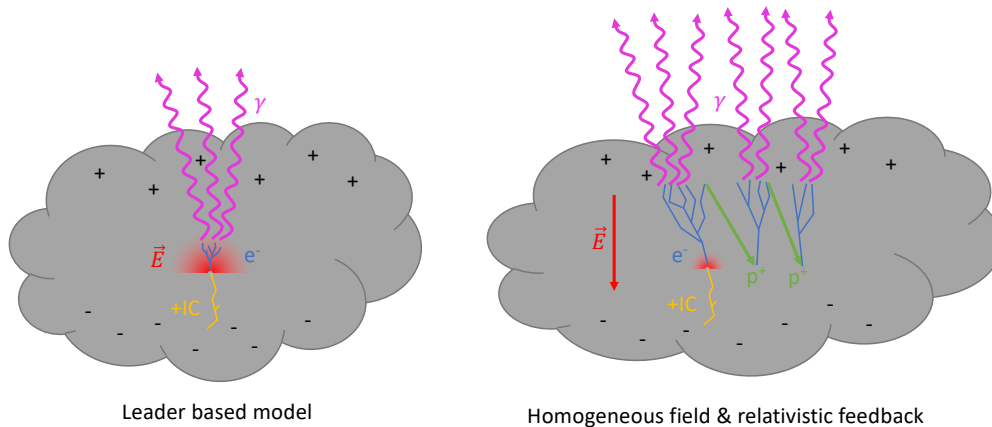


Figure 1.7: Representation of the two main models supported for TGF initiation. For the leader based model, RREAs are initiated and developed in the inhomogeneous electric field surrounding a leader tip, represented in red on the left figure. For the homogeneous field, RREAs are initiated in the inhomogeneous electric field produced by a leader tip (in red) and then develop in the large scale electric field of the thunderstorm (red arrow). Positrons (green) propagate backwards to the start of the avalanche creating relativistic feedback and participating to produce a high number of runaway electrons.

1.5.2 Large-Scale Field Model and Relativistic Feedback

The second model is based on the development of RREAs in a large-scale electric field of the thundercloud [Dwyer, 2008]. The RREAs would be seeded by cosmic-ray air showers or thermal runaway electrons produced by a lightning leader. As explained in the introduction of this section, given the limited number of runaway electron seeds a large-scale electric field cannot explain the energies and fluxes of TGFs without non-physical magnitudes of electric field or field extents. Dwyer [2003] proposed a new mechanism to explain the high number of RREAs needed to produce the great number of photons observed by satellite. It involves that strong large-scale electric field are highly unstable. Indeed, this high number of runaway electrons can discharge the charge layers of the thundercloud and the electric field is very quickly not sustained anymore. The model is based on the fact that positrons and gamma rays could propagate backward. Some positrons and gamma rays could propagate up to the start of the avalanche and seed secondary avalanches by producing new runaway electrons undergoing elastic scattering for positrons and mostly Compton scattering for gamma rays (see Figure 1.7). That way, RREAs are exponentially multiplied. This process is called relativistic feedback [Dwyer, 2007].

Relativistic feedback has been independently modeled by Skeltved et al. [2014], and confirm the results obtained in Dwyer [2003]. Moreover, this model has been claimed to explain and reproduce radio emissions [Dwyer and Cummer, 2013] and multipulse TGFs [Dwyer, 2012].

1.6 Radiation Assessment of Flight Crews

Some previous studies have already briefly estimated the risk for aircraft associated with TGFs. For instance, Tavani et al. [2013] have discussed the possible effects on aircraft electronic equipment of high-energy particles as TGF source electrons, and the secondary particles produced in penetrating an aluminium layer of the plane. They found that some effects as an increase of failure rates could be induced by high-

1.6. Radiation Assessment of Flight Crews

energy particles in electronic system in case of intense TGFs, including secondary neutrons produced by photonuclear reactions. However, these results have to be mitigated against the fact that this study uses a non-standard spectrum up to 100 MeV [Tavani et al., 2011] that is likely erroneous due to instrumental effects [Marisaldi et al., 2019]. Indeed, this spectrum certainly increased the number of neutrons produced and thus the failure rates calculated.

In addition to these effects on avionics, it seems reasonable to mention that TGFs could potentially deliver non-negligible radiation doses at typical commercial flight altitudes. In 2010, Dwyer et al. made the first estimation of the doses delivered by runaway electrons at a TGF source. They indicate that depending on the radius of the runaway electron beam, doses delivered might approach or even exceed annual safety limits (100 mSv). These works and the fact that TGFs and GRGs are found to be far more frequent than initially assessed call for a precise estimation of radiation doses that can be delivered by TGFs.

Aircrews and aircraft passengers in general are exposed to a higher quantity of natural radiation than on the ground. In fact, this natural radiation exposure at flight altitude is due to secondary cosmic radiation, depending on the atmosphere density that decreases with altitude and the proportion of secondary particles produced by collisions from cosmic rays. The exposure is also function of the latitude, the primary cosmic rays being more filtered at low latitudes because of highest cut-off magnetic rigidity.

1.6.1 Cosmic Radiation Origin

Historically, cosmic radiation has been first identified by balloon measurements equipped with ionisation chambers made by Hess [1912] and have then been proved in 1926 to have an extraterrestrial origin [Millikan and Bowen, 1926]. High-energy particles that come from outside the solar system, and for a few percents from outside the galaxy, namely Galactic Cosmic Radiation (GCR), and from the Sun, namely Solar Cosmic Radiation (SCR), go through the Earth atmosphere contin-

Chapter 1. Introduction

uously, in addition to some energetic particles emitted by the Sun in the form of bursts, called Solar Energetic Proton (SEP) events [ICRP, 2016].

Concerning cosmic rays, GCR is composed of 85% of high-energy protons that participate mostly to the radiation dose whereas SCR is composed of 99% of protons with energies lower than 1 MeV. Usually, only GCR is able to go through the magnetosphere. When they enter the atmosphere, GCR undergoes collisions with the atomic constituents and produce secondary particles along their trajectories. As charged particles compose GCR, the radiation depends on the solar activity modulation through its magnetic field that deflects the low-energy GCR, following an 11-year cycle, with a maximum and a minimum of solar activity. Because of the Earth magnetic field, the distribution of this radiation is not uniform in the Earth atmosphere and it is more important near the poles where the magnetic field is nearly vertical than at low latitudes where the magnetic field is nearly parallel to the ground and therefore efficiently acts as a shield. Exposure to cosmic radiation is then dependent on the altitude, on the geomagnetic latitude, and on the solar cycle.

SEP events are the second main contributor to radiation present at high altitudes. They last only several hours and are potentially very intense. They contribute to and can increase significantly the radiation dose received by aircraft passengers only when large solar flares occur on the Sun's surface. They are called Ground-Level Enhancements (GLEs) when they are observed by neutron monitors on the ground. Those are rarer events ($\sim 1/\text{year}$) and only 4 SEP events with GLE have been studied for their ionizing effect at aircraft altitudes in the last 20 years.

1.6.2 Exposure Assessment

The first exposure concerns came with the development of supersonic aviation, with the first flights of the Tupolev-144 prototype in 1968 and of the Concorde prototype in 1969, that were flying at higher altitude (~ 19 km of altitude) than usual flights. A radiometer was installed on the Concorde and some aircrews carried dosimeters

1.6. Radiation Assessment of Flight Crews

to monitor the radiation dose received during the flights. When the dose rate was higher than a fixed radiation level, the aircraft descended to a lower altitude to keep the dose rates to a minimum. It was the beginning of the exposure monitoring for aircrews.

Aircrews are now considered in most of the countries as exposed workers, and an assessment of their exposure is usually made. Currently, the aircrew exposure is estimated by calculations using software that are regularly validated by measurements. In fact, with the exclusion of rare events such as [EASs](#), [GCR](#) is well known and predictable. [SEP](#) events are however non predictable, and can have different intensities. That is why they are usually added to the radiation dose received retrospectively, after some observations and measurements to quantify the level of radiation delivered. Several software used to assess aircrew exposure are cited by [Bottollier-Depois et al. \[2012\]](#). In France, the SIEVERT (Système d'information et d'évaluation par vol de l'exposition au rayonnement cosmique dans les transports aériens – System of information and evaluation per flight of exposure to cosmic radiation in air transport) system [[Bottollier-Depois et al., 2007](#); [Clairand et al., 2009](#)], developed by the Institute for Radiological Protection and Nuclear Safety ([IRSN](#)), the French civil aviation agency ([DGAC](#)), the Paris Observatory, the French Institute for Polar Research–Institut Paul Emile Victor ([IPEV](#)) and Air France, is available since 2001. It is used by French airlines since the law of 8 December 2003 that requires airline company to monitor the exposure of their flight crews. Since 2002, the system is also opened to the public to allow every passenger to calculate the dose received during their flights. SIEVERT assumes a 3-D grid of the atmosphere. The dose rate is estimated in each box, as illustrated in [Figure 1.8](#). The flight routes are then used to calculate the time spent in each box which is multiplied by the dose rate of the box.

Annual maximal doses for aircrew exposure have been fixed to limit the health risk caused by a too significant exposure. Usually, three typical annual effective doses are used. For instance, according to French law regulation, workers suspected

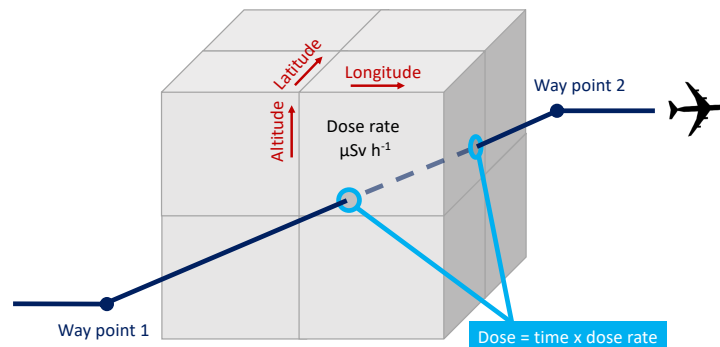


Figure 1.8: Illustration of the dose calculation in SIEVERT. Reproduced from [Clairand et al., 2009].

to receive an annual cumulated effective dose above 1 mSv are considered as exposed workers, and therefore their exposure has to be assessed. Then, for exposed workers, a management threshold is fixed at 6 mSv, defining two worker categories referred to as A and B. Category A workers potentially receive effective doses above 6 mSv and have reinforced medical follow-ups. Category B workers potentially receive an effective dose > 1 mSv but less than 6 mSv. However, for aircrews, the only annual regulatory limit is 20 mSv. Neither limits take natural and medical exposures into account.

1.6.3 Usual Radiation Dose Values

Figure 1.9 represents different usual level of exposure received in everyday life. This chart allows the comparison of the results of this study with usual events to give a better idea of the level of radiation produced by TGFs.

In some figures of the present thesis, the 1-Sv limit is plotted, corresponding to a highly dangerous dose implying acute health effects, including nausea as an example.

Although regulatory limits are established using effective doses, ambient dose equivalents $H^*(10)$ and effective doses have comparable values over the energy range considered in the present study (see Figure 2.2).

1.6. Radiation Assessment of Flight Crews

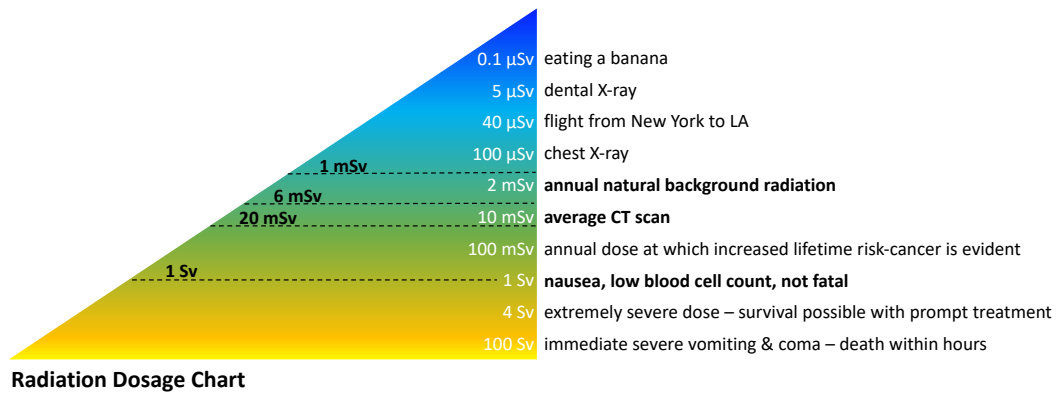


Figure 1.9: Chart with usual radiation exposure level in everyday life.

1.6.4 TGF Additional Exposure

Software like SIEVERT give precise calculations of the received doses for each flight. However, TGFs are not included in these evaluations, as they are a recently discovered phenomenon, and as they are localized events in time and space. The risk associated with TGFs could be evaluated through in-flight measurement monitoring programs. Nevertheless, the exposure from TGFs being localized and very short, assessing the associated risks as closely as possible with airline operating conditions will require collecting a large amount of data and develop new in-flight measurement monitoring programs, adapted to TGF characteristics. The association of simulation and flight measurement studies are necessary to evaluate the need to take TGFs into account as a new possible source of exposure. If TGF doses are assessed to be significant, this could challenge the paradigm of dose evaluation for aircrew. As a consequence, the implementation of measurement systems for on-board re-routing strategies, or individual dosimeters might be required. This could end up as significant costs for airlines, with additional lower performances, and higher uncertainties for individual dosimetry.

1.7 Ongoing projects and campaigns

In the framework of this thesis, we are involved in different projects. A gamma ray spectrometer, presented in Chapter 5, will fly on balloon campaigns and be installed on ground-based locations.

1.7.1 OREO balloon project

Observation du Rayonnement Énergétique dans les Orages (OREO) is a balloon project funded by the French Space Agency (CNES), whose aim is to launch clusters of lightweight balloons into thunderstorms. Those groups of 3 or 4 balloons would be equipped with two instruments: our new gamma ray spectrometer XStorm, and a field mill to measure the local electrostatic field. XStorm, for which instrument I served as co-PI, has been first developed to fly with this project, and therefore had to fit specific constraints such as a light weight, low power, and small size. The first cluster launch in thunderstorms should be planned as early as 2023, depending on the readiness of the electric field mill and the capacity of the CNES technical teams to launch balloons under thunderstorms.

1.7.2 Strateole-2 balloon campaigns and the project STRATELEC

Strateole-2 is a project funded by CNES and is a stratospheric balloon campaign with long duration superpressure balloons flying between 18 and 20 km altitude in the intertropical region. The objectives of this scientific campaign are to study exchanges between the high troposphere and the low stratosphere at low latitudes. A validation campaign has been realized in 2019 (8 flights only), and the first scientific campaign has been performed in 2021, where 17 flights have been done. A picture of a launch performed in 2021 is shown in Figure 1.10. The next and last scientific campaign is planned in 2024, for which we intend to deliver 4 flight models and one spare of XStorm to be flown on these balloons. XStorm has undergone several modifications to adapt to Strateole-2 gondolas, such as a modification of the power

1.7. Ongoing projects and campaigns

supply system, the development of a communication interface (in the form of a single board computer, namely an Arduino board) to communicate with the gondola's on-board computer and the mechanical interface.

Strateole-2 flights are long duration balloons, up to ~ 3 months. The flights are performed at low latitudes (launch from Mahé, Seychelles), with a constant altitude flight of 18 km or 20 km depending on the gondola type. These characteristics are ideal for our purposes. In fact, the 4 XStorm copies will fly for long durations at altitudes above thunderstorms and especially above the most electrically active regions, as can be seen with the lightning density map (Figure 1.1) and the TGF density map (Figure 2.9). Moreover, the flight altitudes correspond to the detection altitude of a high-altitude gamma ray glow detected by Østgaard et al. [2019a], and can allow to detect other such events (see Chapter 6).



Figure 1.10: Picture of a balloon launch during the first scientific campaign of Strateole-2. The gondola is carried by the technical teams until the balloon can carry it entirely to avoid impacts with the ground.

STRatéole-2 ATmospheric ELEctricity (STRATELEC) is another a project funded by CNES, which aims to develop an instrumental payload dedicated to the study of atmospheric electricity, to be flown during Stratéole-2 next scientific

Chapter 1. Introduction

campaign. This project associate *in situ* and remote sensing observation, as well as modeling, to understand the physical processes, such as TGFs and gamma ray glows link with the electrostatic field and with natural lightning activity, as well as their effects on the stratosphere. Several teams are involved as the Laboratoire d'Aérodologie (LAERO, Toulouse, France), the Institute of Atmospheric Physics (Prague, Czech Republic) and the Laboratoire de Physique et Chimie de l'Environnement et de l'Espace (LPC2E). XStorm is one of instruments involved in the project, and will be associated with a high-frequency electric field instrument called Radio Instrument Package (RIP-2), that is still in development by the IAP team. Both instruments will be linked to be triggered together when an event will be detected in XStorm data to save both the electromagnetic signal and the particle data belonging to the same event, and thus maximise the scientific output of the campaign. Finally, we have a collaboration plan with GLD360 to access their lightning detection data during the next campaign.

1.7.3 Ground-based campaigns

The development of such a gamma-ray spectrometer opens new opportunities to detect high-energy events. On the ground, using the same electronics that has been developed but thanks to less restrictive constraints concerning the weight and size, bigger scintillators will be used (BGO and plastic scintillators up to 3" wide). The probability to detect an event will be enhanced through increasing both the measurement time and the size of the detector. The locations that would be used are mostly places in high-altitude, to be closer to the active region of the thunderstorm, and therefore to be able to detect the events from the ground despite the atmosphere layer between the source and the detector. Particular locations as Japan are also considered, as thunderstorms can be very low in altitude and allow to detect glows from ground level.

1.8 Motivation and Objectives

Events such as TGFs became a concern for flight crews since the first radiation dose estimations made by Dwyer et al. [2010] estimated doses approaching regulatory annual limits. Therefore, Air France company have undertaken to fund a study in the form of this thesis to estimate precisely the risks associated with high-energy events linked to thunderstorms. This PhD research has also been advised by radio-protection experts of IRSN that are responsible for the current system of exposure assessment for aircrews (SIEVERT). Finally, the main part of the thesis has been performed at LPC2E, where the high-energy physics associated with thunderstorms is one of the research fields.

To estimate the risk associated with TGFs and glows for aircraft passengers, different approaches have been used. First, we have developed and used simulations mostly based on Monte Carlo methods to estimate the radiation doses generated by the different particles involved in the production of a TGF (Chapter 3). Then, the need was to assess the probability that a commercial flight would find itself in a TGF. To do so, we crossed data from TGF satellite detections and commercial flight routes from a French airline (Air France) (Chapter 4).

In parallel with theoretical studies, we have developed a new gamma ray spectrometer, designed to perform *in situ* measurements of TGFs and gamma ray glows (Chapter 5). The future measurements made with the detector will allow to confirm estimations of radiation doses for TGFs, during balloon measurements, but also will serve to estimate the occurrence of TGFs and glows. Balloon flights have been made during the thesis to test the instrument by clear weather, and two balloon campaigns are planned and described later in the thesis, for which promising measurements are estimated and expected (Chapter 6).

Methods

Key Points

- Conversion fluence to ambient dose equivalent
- Two different models are used to estimate TGF radiation doses
- Use of simulated flight routes and real flight data with a TGF density map to estimate the probability for an aircraft to be hit by a TGF

In this chapter, we present the methodology of the different studies carried out in this thesis. The two first sections establish both the radiation dose calculation method and the models used to estimate the radiation doses generated by a TGF. The results of this study are presented and discussed in Chapter 3. The third section is dedicated to the methods used to calculate the probability for a commercial flight to be hit by a TGF. The results of this study are presented and discussed in Chapter 4.

2.1 Dose Calculations of Chapter 3

In order to estimate the possible impact that TGFs and gamma ray glows could have on the radiation exposure of individuals in commercial flights, in Chapter 3 we will utilize radioprotection terms and units. Radioprotection (or radiation protection) is a field to ensure the protection of humans and their environment against the harmful effects of ionizing radiation. An introduction on the radioprotection field is given in Section 2.1.1, and the calculation method used for radiation doses estimation is explained in Section 2.1.2.

2.1.1 Introduction on Radiation Doses

In radioprotection, the variable quantifying the energy deposited by ionizing radiation in matter per unit mass is called absorbed dose and is expressed in grays (Gy). To take into account the health hazard caused by the radiation, two other quantities are used. The effective dose is a *protection* quantity in which the exposure limits are expressed. It is calculated by summing the absorbed dose deposited in all organs penetrated by the radiation, weighted by coefficients that take into account the variability of organ sensitivity to ionizing radiation and the variability of the biological effects due to the different radiation types. The ambient dose equivalent, written $H^*(10)$, is an *operational* quantity. It is defined by the absorbed dose that would be deposited by the corresponding expanded and aligned radiation field into a 30-cm diameter sphere made of tissue-equivalent material (ICRU sphere) at a 10-mm depth on the radius opposing the direction of the aligned radiation field, taking into account the radiation type. It is used to estimate the effective dose through measurements. Both quantities are expressed in sieverts (Sv) [ICRP, 2007]. Figure 2.1 summarizes these definitions. In the results presented in Chapter 3, we use $H^*(10)$ for the sake of reproducibility and comparison to measurements. Note that $H^*(10)$ is usually greater than the effective dose for the particles and energy range considered.

2.1.2 Doses Calculations

Mainly two radiation types are involved in TGFs, electrons and gamma rays. From both models that will be presented in Section 2.2, the output are the radiation fluences, expressed in cm^{-2} . It corresponds to the number of particles going through a surface per unit area, and therefore to a flux integrated over time. Fluence-to-dose conversion coefficients have been precisely calculated by Pelliccioni [2000] and reported in the Fluka database. These coefficients are represented in Figure 2.2 in magenta for gamma rays and in blue for electrons. They are expressed in Sv cm^2 .

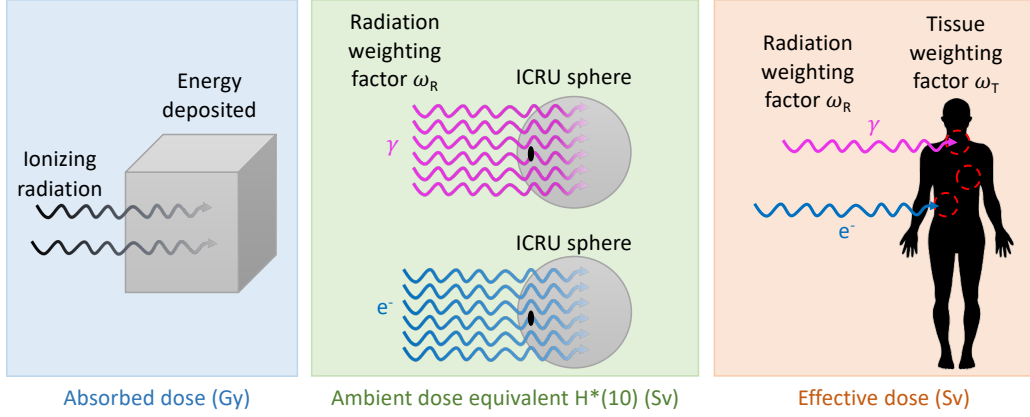


Figure 2.1: Illustration of three different radioprotection quantities used in this thesis.

The solid lines correspond to the coefficients for $H^*(10)$, whereas the three types of dashed lines correspond to effective doses under different exposure geometries. AP corresponds to an anteroposterior exposure, Iso corresponds to an isotropic exposition, and Top corresponds to an exposition from the top.

$H^*(10)$ can then be calculated as:

$$H^*(10) = \int_{\varepsilon_{min}}^{+\infty} f_{H^*}(\varepsilon) \phi(\varepsilon) d\varepsilon \quad (2.1)$$

where ε_{min} is the minimum energy considered, $\phi(\varepsilon)$ is the fluence of electrons or photons as a function of the energy ε , calculated in this study by the models explained in Section 2.2, and f_{H^*} is the fluence-to-ambient dose equivalent conversion coefficient for electrons or photons.

We can define a coefficient h to convert the electron fluence to the ambient dose equivalent, assuming that electrons are distributed following the [RREA](#) spectrum:

$$h = \int_{\varepsilon_{min}}^{+\infty} f(\varepsilon) f_{H^*}(\varepsilon) d\varepsilon \quad (2.2)$$

where $f(\varepsilon)$ is the normalized [RREA](#) spectrum (integration of $f(\varepsilon)$ over the energy range equals one) such that $\phi(\varepsilon) = \varphi \cdot f(\varepsilon)$, where φ is the total fluence, and f_{H^*}

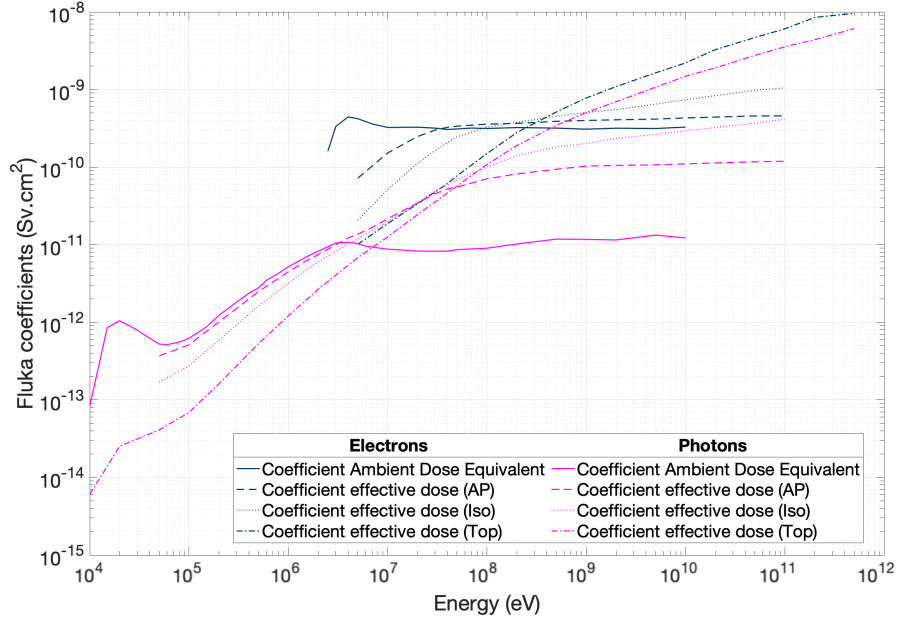


Figure 2.2: Fluence-to-dose conversion coefficients as a function of the energy, taken from the Fluka database [Pelliccioni, 2000]. The solid lines correspond to the conversion coefficients for $H^*(10)$. The three other lines correspond to different exposure geometries: anteroposterior (AP), isotropic (Iso) and from the top (Top).

is the fluence-to-ambient dose equivalent conversion coefficients for electrons. As a consequence, h is a constant. $H^*(10)$ can then be simply calculated by:

$$H^*(10) = h \cdot \varphi \quad (2.3)$$

where h , for the ambient dose equivalent, was found to be $3 \cdot 10^{-14} \text{ Sv m}^2$, using an analytical RREA spectrum. Dwyer et al. [2010] have calculated h_E for an effective dose in anteroposterior direction and found it to be $h_E = 9 \cdot 10^{-15} \text{ Sv m}^2$. Both values are consistent given the differences between the type of dose calculated.

2.2 Models used in Chapter 3

In Chapter 3, we will present results of TGF simulations that estimated the radiation doses generated by the particles involved. First, high-energy electrons at the source

of TGFs are assumed to be produced in two ways. The first model used, referred to as “pure leader model”, involves runaway electron acceleration in the potential drop formed by the leader (see Section 1.5.1). The second model used assumes that RREAs are initiated by a leader further develop in the ambient homogeneous electric field of the thunderstorm. Gamma rays are emitted by bremsstrahlung from high-energy electrons. We present the Monte Carlo code used to simulate gamma rays in Section 2.2.3. For the three models, two main assumptions are used:

- the source altitude is chosen to be 12 km
- 10^{18} photons with $\varepsilon > 1$ MeV are produced by the TGF

Indeed, the source altitude of TGFs is estimated to be between 10 and 15 km (e.g., [Cummer et al., 2011, 2014, 2015]), and satellite measurements support the production of 10^{18} photons in a TGF (e.g., [Gjesteland et al., 2015; Mailyan et al., 2016, 2019]).

2.2.1 Pure Leader Model

In the pure leader model, seed runaway electrons are assumed to be accelerated in the high and inhomogeneous electric field created by the potential difference between a leader tip and the ambient electric field of the thunderstorm. RREAs are also assumed to develop in the electric field of the leader tip. For the simulation, we use a 3-D relativistic Monte Carlo model to simulate the propagation of electrons in air. The air is modeled as 80% of N₂ and 20% of O₂. The model is capable of simulating electrons from sub-eV to GeVs [Celestin and Pasko, 2011]. The length l of the leader immersed in an ambient electric field $E_0 < E_{th}$ determine the electric field. The quantity E_{th} is the threshold electric field for producing RREAs at ground level (already discussed in equation 1.2). The electric field in the vicinity of the leader tip is calculated through the method of moments (e.g., [Balanis, 1989]) assuming that the leader channel is equipotential. This method implies that the electric field is not yet shielded by the developing streamers in our simulations (see discussion

Chapter 2. Methods

in [Celestin et al., 2015]). The energies of secondary electrons are obtained from the ionization differential cross-section, calculated through the relativistic binary-encounter-Bethe model [Celestin and Pasko, 2010; Kim et al., 2000]. Considering that the formed ion is static, the relativistic equations of conservation of momentum and energy give the scattering angles of primary and secondary electrons. A continuous radiative friction of electrons due to bremsstrahlung [Berger et al., 2005] is also implemented. It becomes significant for electrons with energy on the order of a few 10s of MeV or more.

We use a potential drop of 300 MV between the lightning leader and the ambient electric field. This potential drop allows for RREAs to develop fully and reach a typical spectrum with an exponential cutoff (see Celestin et al. [2015]).

Criticisms and constraints about such models have been expressed in Skeltved et al. [2017]. Celestin and Pasko [2011] and Skeltved et al. [2017] argue that the static vacuum solution overestimates the maximum electric field and that it should be limited to a magnitude of 50 kV cm^{-1} . This maximum field is also constrained by the time scale of the increase of the electric field in front of a new leader branch during leader-stepping (see Celestin and Pasko [2011], Figure 7). Based on the dynamic streamer production process at the tip of the lightning leader [Bazelyan and Raizer, 2000, pp. 67-68], Celestin and Pasko [2011] also argued that 50 kV cm^{-1} was a reasonable assumption on the maximum of the electric field amplitude. It must be noted that the latter argument is based on the hypothesis of a steady streamer production. A fast potential increase in the newly created leader branch might lead to a stronger electric field at the tip of the leader, as also noted by Celestin and Pasko [2011] and Skeltved et al. [2017]. In the present simulations, the static vacuum solution is obtained through the method of moments (e.g., [Celestin et al., 2015]) and runaway electrons are only injected at the location where the electric field magnitude gets below 50 kV cm^{-1} .

The initial number of electrons at the source has to be estimated in order to correctly scale the simulation so as to ensure that 10^{18} photons with energy > 1

MeV are eventually produced (see Section 2.2). Indeed, the simulation is composed of 40,000 electrons at the beginning and is scaled to the real number of electron at the source in a second step. The average bremsstrahlung photon production frequency per electron $\langle \nu_\gamma \rangle$, for electrons with energies greater than ε_{min} at each moment of time is (e.g., [Celestin et al., 2015]):

$$\langle \nu_\gamma \rangle (t) = N \int_{\varepsilon_{min}}^{+\infty} f(\varepsilon, t) \sigma_\gamma(\varepsilon) v_e(\varepsilon) d\varepsilon \quad (2.4)$$

where $\sigma_\gamma(\varepsilon) = \int_{\varepsilon_{min}}^\varepsilon \frac{d\sigma_\gamma}{d\varepsilon_\gamma}(\varepsilon, \varepsilon_\gamma) d\varepsilon_\gamma$ is the total cross section for production of bremsstrahlung photons with energies greater than ε_{min} by deflections of an electron with energy $\varepsilon > \varepsilon_{min}$, N is the local air density, $f(\varepsilon, t)$ is the instantaneous normalized energy distribution of electrons at any moment of time, $v_e(\varepsilon) = c\sqrt{1 - \left(1 + \frac{\varepsilon}{mc^2}\right)^{-2}}$ is the relativistic speed of an electron with energy ε and rest mass m , and c is the speed of light in vacuum. The total number of produced photons with energy greater than ε_{min} is [Celestin et al., 2015]:

$$N_\gamma = \int_0^{+\infty} N_e(t) \langle \nu_\gamma \rangle (t) dt \quad (2.5)$$

where $N_e(t)$ is the number of high-energy electrons as a function of the time.

2.2.2 Homogeneous Electric Field with Leader Injection Model

The second model used in Chapter 3 assumes that RREAs are initiated close to a leader tip and further develop in an ambient electric field of magnitude $E > E_{th}$, spanning over a distance of 1 km. Thus, the electron source is thermal runaway electrons produced by streamers and accelerated in a leader tip. This leader injection does not constrain the model to have a very localized electron source as the thermal runaway electrons propagate in a divergent field, possibly produced by different leader branches, and thus according to simulations the electron source diameter can take values up to hundreds of meters. This is the reason why we estimate electron

Chapter 2. Methods

doses for this model with an initial source diameter varying between 0 and 2 km.

The initial number of electrons composing the electron source discussed above is defined so as to produce 10^{18} photons with energies > 1 MeV in the end. It depends on the electric field, the length of the avalanche region, and the altitude. Using the average RREA speed $0.89c$ [Coleman and Dwyer, 2006], the number of electrons during a RREA is expressed as:

$$N_e(t) = N_0 \exp\left(\frac{z}{\lambda(E)}\right) = N_0 \exp\left(\frac{t \times 0.89c}{\lambda(E)}\right) \quad (2.6)$$

The avalanche length, also called e-folding length, is expressed as shown in equation 1.4, for an electric field magnitude $E > 3$ kV cm $^{-1}$ [Coleman and Dwyer, 2006]. Taking a RREA spectrum as $f(\varepsilon) \propto \exp(-\varepsilon/7.3 \text{ MeV})$, in equations 2.4 and 2.5, we can calculate the number of electrons at the beginning and at each moment of time during the avalanche, depending on the electric field value. In order to study the changes implied by different electric field strengths, we use two magnitudes: $4 N/N_0$ kV cm $^{-1}$ and $5 N/N_0$ kV cm $^{-1}$. These two amplitudes respectively correspond to a ratio $\xi = E/E_{th}$ of ~ 1.4 and ~ 1.8 .

The maximum electric field magnitude used is $5 N/N_0$ kV cm $^{-1}$ over a maximum length of the acceleration region of 1 km. The injection of runaway electrons in this work is assumed to be localized at an altitude of 12 km. The local electric field magnitude is therefore 1.18 kV cm $^{-1}$. Figure 2.3 (Reproduced from [Dwyer, 2003]) shows the relativistic feedback threshold electric field magnitude as a function of the acceleration length at ground level. Using GEANT4, Skeltved et al. [2014] (in their Figure 6) found somewhat lower thresholds, while in good general agreement with Dwyer [2003]. Both results presented by Dwyer [2003] and Skeltved et al. [2014] are shown considering ground-level atmospheric density in their papers. At a 12 km altitude, an acceleration under a field of 1.18 kV cm $^{-1}$ over 1 km is scalable to acceleration under 5 kV cm $^{-1}$ over a length of 236 m. Both figures presented by Dwyer [2003] and Skeltved et al. [2014] clearly show that the configuration studied

here is subcritical (“semi-stable”, in the words of Dwyer [2003]), although close to triggering relativistic feedback. In conclusion, relativistic feedback is not expected to occur in the configurations studied in the present paper and is then not introduced in the simulations. In that regard, the configuration considered here is seemingly analogous to that observed by Kelley et al. [2015].

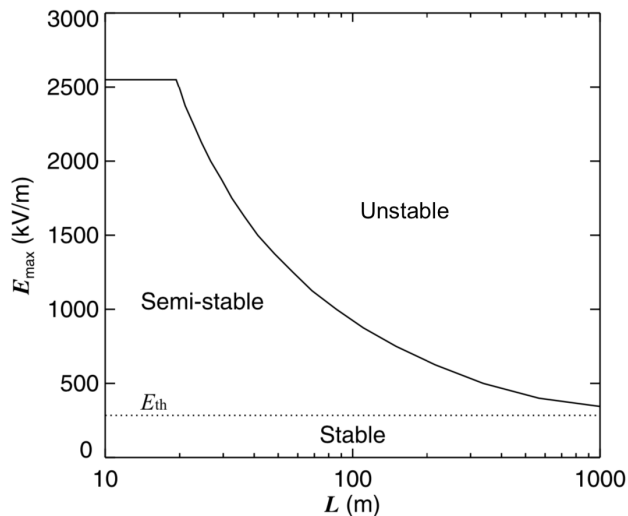


Figure 2.3: Reproduced from Figure 3 of [Dwyer, 2003]. Maximum static electric field magnitude in air as a function of the length of the electric field region at ground level. The value of the threshold electric field E_{th} is represented with the dotted line. Above the solid line, electric fields are unstable, and cannot be maintained. Between the solid line and the dotted line, the electric field may eventually discharge. Below the dotted line, the electric field is stable.

To calculate the ambient dose equivalent, we need to estimate the electron fluence. The electron beam diameter remaining a free parameter, we choose to estimate the dose depending on the electron beam diameter at the end of the avalanche, for diameters between 0 and 2 km.

To estimate the electron beam diameter during the avalanche, we make the assumption that the beam radius follows a diffusion radius $r_D = \sqrt{\frac{\alpha D_{\perp}}{v_e} z(t) + R_0^2}$, where R_0 is the initial radius and taking $\alpha = 1/4$ according to Monte Carlo simulations [Berge et al., 2019]. For the diffusion coefficient D_{\perp} , we make use of the

following estimate [Dwyer et al., 2010]:

$$D_{\perp}/v = (5.86 \cdot 10^4)E^{-1.79} \quad (2.7)$$

in meters, where E is the electric field expressed in units of kV m^{-1} .

2.2.3 Photons and Secondary Electrons

Additionally to doses from runaway electrons in the TGF source region, doses due to photons and to electrons produced as a result of photon TGF collisions with air molecules are also estimated. We use a Monte Carlo code based on [Østgaard et al., 2008] to propagate photons in the atmosphere. The code takes into account three types of interactions for the photons. Photoelectric absorption is a collision made by a photon with a molecule producing an electron. Compton scattering is a collision made by a photon with an electron emitting a new photon with a lower energy. Electron-positron pair production is the collision made by a photon with an atomic nucleus producing an electron and a positron. As shown in Figure 2.4, photoelectric absorption is the main process in air for energies up to ~ 30 keV, Compton scattering is the main process in air for energies from ~ 30 keV up to ~ 30 MeV, and electron-positron pair production is the main process in air for energies higher than ~ 30 MeV. Some secondary electrons are produced by the electron-positron pair production. Energy and position of secondary electrons created are recorded for the most dangerous location, that is for the closest point along the axis of the source, within a 500-m radius, 1 km above the source. In Earth atmosphere, positrons created through electron-positron pair production are slowed down in ionizing the material along their path and electrons contribute to enhance the gamma ray population through bremsstrahlung such as electrons. In the simulation, positrons created through electron-positron pair production are assumed to annihilate locally where the collision occurs, producing two photons with energy of 511 keV in opposite directions.

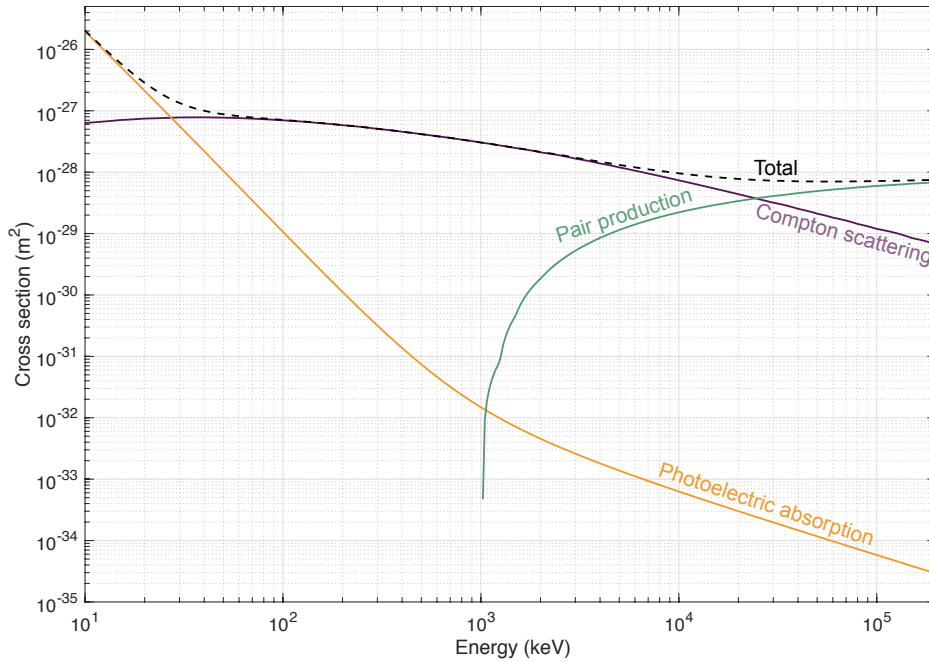


Figure 2.4: Cross sections in air of the three types of collisions taken into account in the Monte Carlo code used for the gamma ray simulations [Berger et al., 2010].

The initial velocities of the photons are uniformly distributed within a cone of 45° opening half-angle. The scale height is assumed to be 8.2 km, in good agreement with a fit of the atmosphere [U.S. Standard Atmosphere, 1976] between 0 and 15 km (the scale height characterizes a planetary atmosphere; it is the increase in altitude corresponding to a decrease in atmospheric pressure by a factor e). The energy distribution of initial gamma rays is in agreement with the RREA phenomenon, which produces a 7.3 MeV cut-off in the primary electron spectrum. Bremsstrahlung from secondary electrons produced by photon collisions is not taken into account.

In the simulation, as the configuration involves a cylindrical symmetry, photons are collected in different rings, 50-m large and concentric about the axis of symmetry of the configuration, in order to estimate the fluence as a function of the radial distance, until they reach either an upper virtual screen at 500 km or the ground (see Figure 2.5).

Photons with momenta away from the vertical axis contributing to the dose

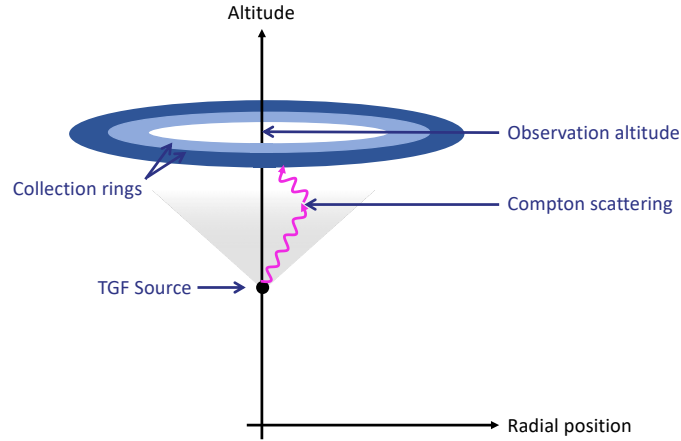


Figure 2.5: Illustration of the horizontal rings used to collect photons in the Monte Carlo simulation used.

received by a 3-dimensional object come from a surface on the collection ring larger than the vertical projection of the 3-D object onto the flat ring (see Figure 2.6). Therefore, the contributions of such photons (for which the flux is calculated through the horizontal collection ring) should be weighted higher by a factor of $\frac{1}{\cos(\theta)}$, as shown in Figure 2.6 [Bowers, 2017]. This correction is not implemented in the results shown in the present work. Because of this geometrical effect, we estimate that photon doses can be underestimated up to a factor 2. In fact, this effect is less important for electrons which mostly propagate vertically in our simulations.

In order to focus on the worst-case scenario, we simulated a point photon source at an altitude of 12 km, for the sake of consistency with calculations of runaway electron doses. 10^{18} initial photons are also considered to be produced.

2.3 Statistical Method used in Chapter 4

Chapter 4 presents the results of the statistical study for which an estimation of the probability for a commercial aircraft to find itself in the beam of a TGF has been undertaken. TGF data from the Fermi satellite (NASA) have been used to determine a TGF density map (Section 2.3.1) that has been then used with flight

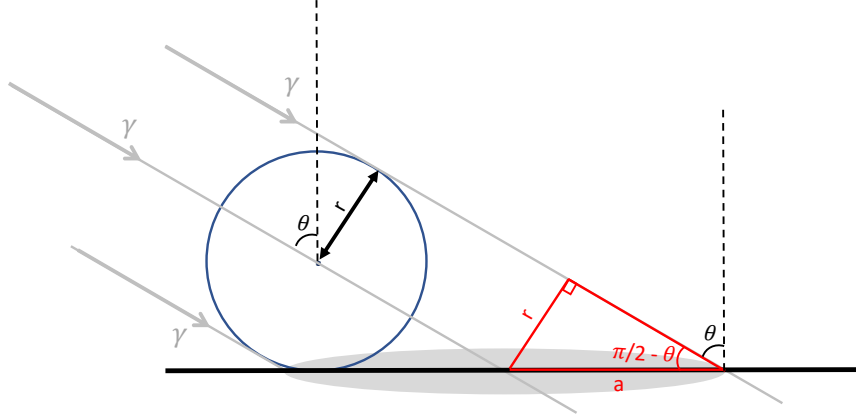


Figure 2.6: Scheme of the difference between flat and 3D-configuration. When a particle goes through the ICRU sphere (Figure 2.1), the corresponding flat surface is an ellipse (shown in gray) with parameters a and $b = r$, where r is the ICRU sphere radius. Using the scheme, we find: $a = \frac{r}{\cos(\theta)}$. The effective area of the sphere is then: πr^2 and the effective area of the ellipse (projection on the flat surface) is: $\pi ab = \pi \frac{r^2}{\cos(\theta)}$, hence the $\frac{1}{\cos(\theta)}$ correction factor corresponding to a weight on every incoming particle.

route data (Section 2.3.2) to calculate the probabilities to be hit for each aircraft (Section 2.3.3).

2.3.1 TGF Data

TGF data that have been used in this study are the TGF detected by Fermi satellite (NASA) and reported in the first Fermi-Gamma ray Burst Monitor (GBM) TGF catalog [Roberts et al., 2018]. Fermi is an astrophysics satellite that has been launched on the 11 June 2008. GBM is an instrument whose aim is to detect sudden flares of gamma-rays produced by Gamma ray Bursts (GRBs) and solar flares. GBM is composed of 12 NaI and 2 BGO scintillators and detects photons between 5 keV and 25 MeV. Its absolute timing resolution is of $\sim 2 \mu\text{s}$, hence its ability to detect TGFs. 4135 TGFs have been detected between 11 July 2008 and 31 July 2016 by the GBM. Fermi's instrument are turned off over the South Atlantic Anomaly (SAA) to reduce the risk associated with a higher exposure to trapped radiation belt protons. Con-

Chapter 2. Methods

sequently no TGF has been detected above this surface. The SAA is represented in Figure 2.7.

The triggering system to detect TGFs has been modified several times during the mission [Briggs et al., 2013], as GBM was not initially developed to detect TGFs. In fact, since July 9, 2010, the triggering system can be done on the ground thanks to the possibility to recover the whole data in predetermined areas that are assumed to produce TGFs. First, this was applied to the area above the Americas, then the spatial areas have been extended progressively on 27 January 2011, on 26 May 2011, and on 31 August 2011. On November, 26, 2012, this process has been extended to the entire orbit outside the SAA. In order to use a consistent set of data, only TGFs that have been detected between 26 November 2012 and 31 July 2016 have been used in our study. It represents 2807 TGFs, represented in Figure 2.7.

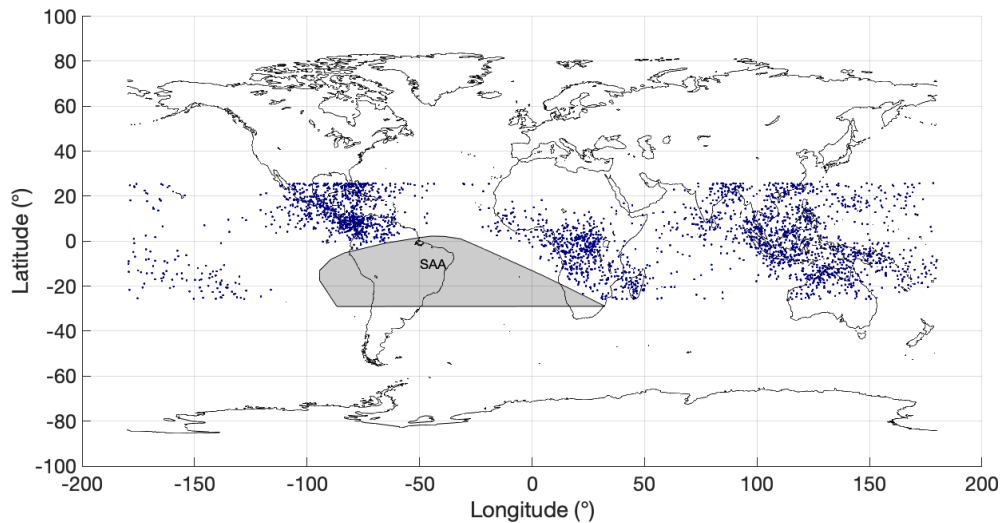


Figure 2.7: Position of Fermi for each of the 2807 TGFs detected by GBM between the 26 November 2012 and 31 July 2016.

The first step of this study is to calculate a TGF density map from this list of detected TGFs. For that, we define a grid based on latitude and longitude coordinates, with a resolution of 2° , for longitudes in $[-180^\circ ; +180^\circ]$ range and for latitudes in $[-26^\circ ; +26^\circ]$ range (Fermi trajectory goes up to 26° in latitude). Each

2.3. Statistical Method used in Chapter 4

surface element area in degree square can be approximated as:

$$dS_{jk} = R^2 \times \left(\frac{\pi}{180}\right)^2 \times \cos\left(y_j \times \frac{\pi}{180}\right) \times (x_k - x_{k+1}) \times (y_j - y_{j+1}) \quad (2.8)$$

with x and y the longitude and latitude in degrees, j and k are longitude and latitude indices for the surface elements and $R = 6371$ km is the Earth radius.

Fermi Trajectory

In addition to a factor that compensate the number of detected TGFs above each surface element as a function of the surface element area, a correction has to be applied on Fermi TGF data in order to take into account the time spent by Fermi above each surface element.

We use Fermi's orbit parameters [[heavens above.com](http://heavens.above.com), 2021] to simulate its trajectory over 10 days (see Figure 2.8a). We then calculated the time spent above each surface element. This time is only dependent on the latitudes and is shown in Figure 2.8b.

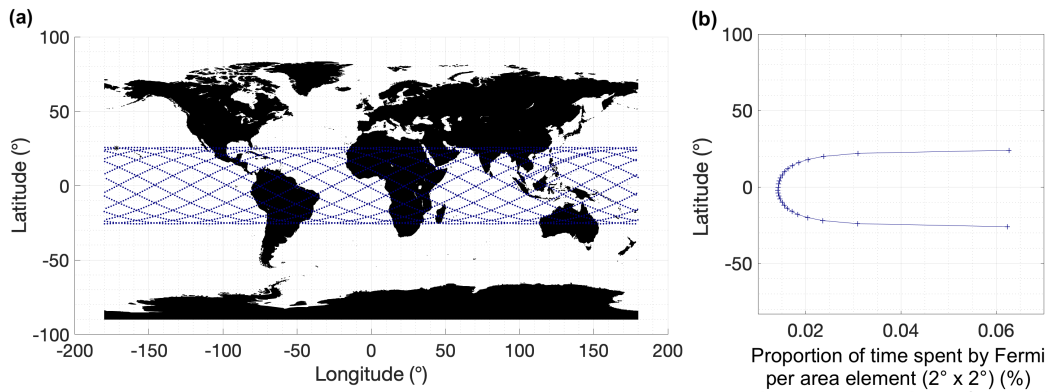


Figure 2.8: (a) Simulated Fermi trajectory for 1 day. (b) Proportion of time spent by Fermi over each surface element as a function of latitude (averaged over the longitudes).

TGF Density Map

We introduce the following variables to express the TGF density as a function of the number of TGFs in each surface element:

- $S = \sum_{j,k} dS_{jk}$ is the total surface observed by Fermi (km²) that is ~ 224 millions of km²
- $dt_{jk} = \frac{\text{time spent by Fermi above dS over 10 days}}{10 \text{ days}}$ are the proportion of time spent by Fermi above each surface element (no units) – can be seen in Figure 2.8b
- T is the duration between the 26th of November, 2012 and the 31st of July, 2016 (in years) over which the TGFs were detected (~ 3.6 years)
- FoV is the field of view of Fermi-GBM, corresponding to a disk with a radius r around Fermi's nadir (km²) [Briggs et al., 2013]
- n_{jk} are the number of TGFs detected in each surface element during the observation period of ~ 3.6 years

N_{jk} is the number that would have been detected in each surface element if Fermi was able to detect TGFs everywhere over S at anytime during the 3.6 years observation period. It is calculated by:

$$N_{jk} = n_{jk} \times \frac{S}{\text{FoV}} \times \frac{1}{dt_{jk}} \quad (2.9)$$

The TGF density d_{jk} for each surface element can then be calculated by:

$$d_{jk} = \frac{N_{jk}}{dS_{jk} \times T} \quad (2.10)$$

To calculate the radius r of Fermi-GBM field of view, we used an updated version of Briggs et al. [2013]'s Figure 8.b), describing Fermi-GBM TGF detection rate R as a function of the radial distance r . Assuming a full efficacy between 0 and 300

2.3. Statistical Method used in Chapter 4

km, one gets the value of $R(0)$. Then, we integrated the curve between 0 and 800 km, corresponding to $\int_0^{800 \text{ km}} R(r) 2\pi r dr$, and calculated FoV corresponding to the maximum radius for which the efficacy can be constant for $r < FoV$ and equal to $R(0)$, conserving the same integral value. Finally, FoV is calculated to be 416 km, and this value is used in this work.

The density map is expressed in $\text{TGF km}^{-2} \text{ year}^{-1}$, and is presented in Figure 2.9. It represents the TGF density for Fermi-GBM-detectable TGFs, that is to say fluent enough to be detectable at 500 km altitude. We can expect less fluent TGFs to be produced but not detectable by Fermi. The highest TGF density from this map is located above Panama and is equal to $\sim 5 \text{ TGFs}/100 \text{ km}^2/\text{year}$. Using this density map, we can estimate the number of TGFs (i.e., Fermi detectable TGFs) produced per year on the whole surface S . We find this value to be 380,000 TGFs/year. This value is consistent with the estimation made by Briggs et al. [2013], which used TGF data from the same instrument but not over the same period, neither the same TGF triggering process.

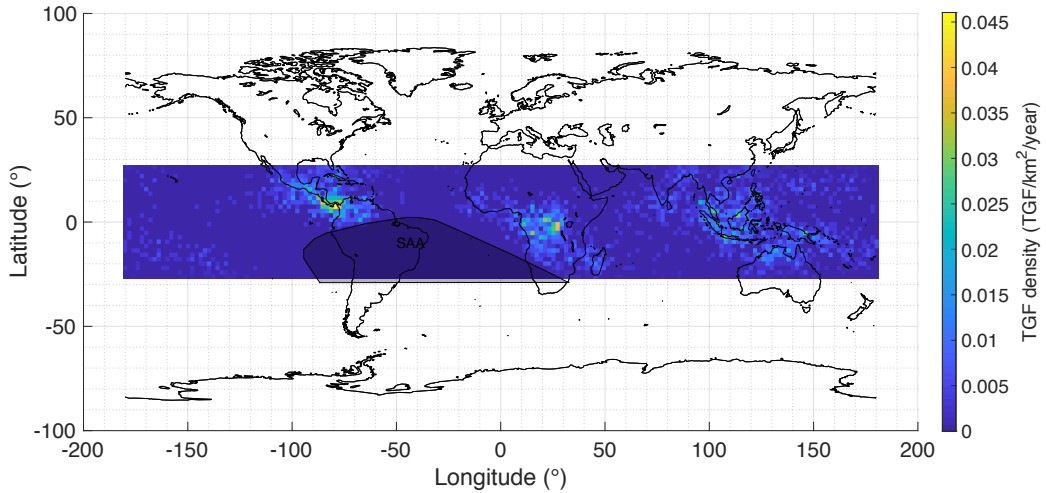


Figure 2.9: TGF density map calculated from Fermi detectable TGFs.

Comparison with TGF Frequency of Measurements

Researchers of the [ADELE](#) project mentioned in the introduction, have performed a measurement campaign with an array of six gamma ray detectors aboard an aircraft. They detected one [TGF](#) within 37 hours of flight near a thunderstorm, as well as 1213 lightning flashes [[Smith et al., 2011a](#)]. We can compare this measurement period with the calculated [TGF](#) density map. According to [Christian et al. \[2003\]](#), the lightning density in Florida (where the measurements took place) is 35 lightning $\text{km}^{-2} \text{ year}^{-1}$. [Smith et al. \[2011b\]](#) observed a factor of 26 above this value, which is not unreasonable since [ADELE](#) was flying in the vicinity of thunderstorms. The field of view of their detectors was ~ 10 km radius around the aircraft. Reshaping our [TGF](#) density map of [Figure 2.9](#) for a 10 km disk around the detector, we get the [TGF](#) density in Florida of 8.4×10^{-8} TGF/s/10 km-radius. Multiplying this density by the 37 hours of measurement and the factor of 26 to scale the lightning density, we get that: 1 over 3 campaigns like [ADELE](#) could detect a Fermi detectable [TGF](#). Therefore, the density map seems to be consistent with the results of [ADELE](#) campaign.

2.3.2 Flight Route Data

This section presents the flight data that have been used with the [TGF](#) density map, in order to calculate the probability to be hit by a [TGF](#) in a commercial flight. The totality of the flight route data of all the airlines in the world represents a huge amount of data, that is not possible to obtain easily. For that reason, we decided to use two approaches in this study. The first approach is to simulated flight route data in the world from a list of the biggest airports in the world. The second approach is to use real flight data from one airline, namely Air France.

Simulation of Flight Routes

A list of the 606 biggest airports in the world is used to account for the global air traffic [ourairports.com, 2021]. 5000 routes are drawn randomly by choosing randomly the departure airport and the arrival airport. The route between two airports is calculated as a geodesic, and the aircraft velocity is assumed to be constant and equal to 250 m s^{-1} . Wilkerson et al. [2010] estimate that 86% of the flights in the world were short-haul flights, 10% of the flights were medium-haul flights and only 4% of the flights were long-haul flights. This proportion is taken into account in assigning a weight to the probability of the three type of flights. The total number of flights per year is assumed to be 38.9 millions in 2019, as shown in Figure 2.10 [statista.com, 2021]. We emphasize that this approach contains significant biases. However, it provides an interesting order of magnitude estimate.

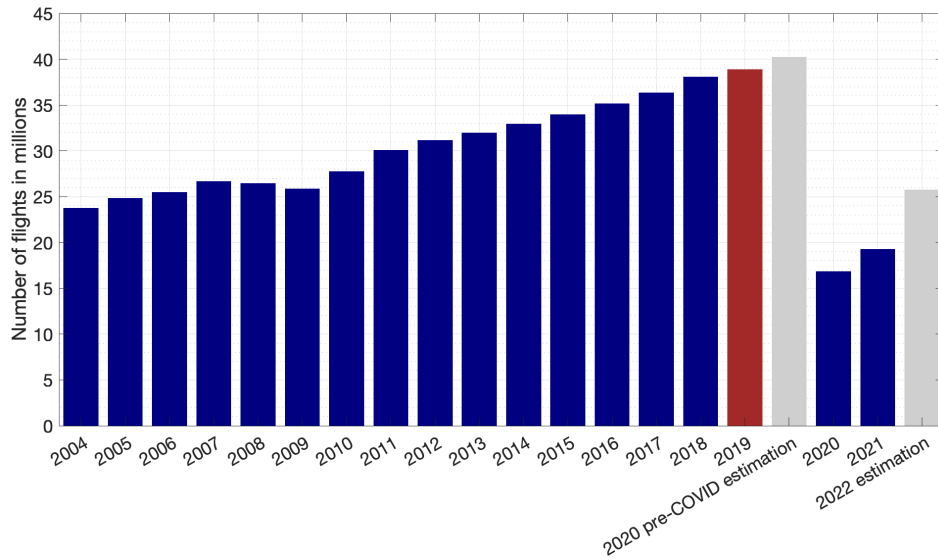


Figure 2.10: Number of flights per year in the world from 2004 to 2022 [statista.com, 2021]. We choose as a reference number of flights per year the number of flights performed in 2019 (red), before the COVID-19 crisis that caused a brutal decrease in the global air traffic in 2020.

Real Flight Route Data from Air France Company

Real flight route data from Air France airline from the 1st January, 2014 and the 31st July 2016 have been collected and used in this study. The advantage is that these flight data describe the actual routes flown by the pilots. The disadvantage of this approach is that it is limited to one airline, that is not likely to be representative of the global air traffic.

Every flight has been reported as follows: departure airport and the corresponding date, arrival airport and the corresponding date, as well as waypoints on the trajectories. The number of waypoints can reach up to 20 for the longer flights. In addition to a probability calculation on each route performed by Air France, a linear interpolation between the waypoints makes possible the real time and space comparison between Fermi detected TGF locations and in-flight aircraft. These results are presented in Chapter 4. It is worth mentioning that we assume TGF positions to be Fermi's footpoint at the moment of the detection. However, this approximation being done on all TGF positions should not imply big changes in the TGF distribution, given the randomness of the process.

2.3.3 Probability Calculations

From the results presented later in Chapter 3, a harmful radius around the TGF source is deduced to be 200 meters. In that sense, the term "hit by a TGF" in this manuscript means that the aircraft is closer than 200 m from a TGF source. For each flight, the probability for an aircraft to find itself closer than 200 m from a TGF source will be calculated as follows:

- Linearly interpolate the trajectory with the frequency of 1 Hz (1 position/s)
- Calculate the time Δt_{jk} spent above each surface element (in seconds, with a resolution of 1 s)

- Get the probability for the aircraft to be hit above each surface element by:

$$p_{jk} = \Delta t_{jk} \times d_{jk} \quad (2.11)$$

The TGF density d_{jk} here is now expressed in TGF/0.1257 km²/s, corresponding to the number of TGFs per second in a 200 m-radius area.

- Get the probability for the aircraft to be hit on the whole route, corresponding also to the number of TGFs that can hit the aircraft on the whole route, by:

$$P_{\text{flight}} = \sum_{j,k \in \Omega} p_{jk} \quad (2.12)$$

where Ω is the set of indices indexing surface elements crossed by the considered route

The obtained probability corresponds to the number of TGFs that can hit the aircraft during a given flight. Since it is a small number ($\sim 10^{-8}$), to get a more meaningful number we will calculate the number of flights between two TGF hits on this route. When the frequency of flights on this route is known, the time between two TGF hits on this route will be calculated.

2.4 Conclusions

In this chapter, we presented the methods used for the two theoretical studies of Chapter 3 and Chapter 4 of this thesis. These methods are originals in their application. Indeed, the calculation of the radiation doses delivered along the avalanche for photons and within two different models of TGF production for electrons have not been done until this work. Likewise, the Chapter 4 study, using at the same time TGF data and flight route data (simulated and real) to quantify the risk for an aircraft to be hit by a TGF, is new.

Estimation of Radiation Doses Associated with TGFs

Key Points

- Radiation doses associated with runaway electrons producing Terrestrial Gamma ray Flashes may exceed usual safety annual limits
- The highest doses from electrons are delivered in very compact regions
- For most TGFs, photon doses do not exceed safety limits and secondary electrons produce negligible radiation doses

In order to evaluate whether TGFs represent a significant exposure to aircraft passengers, we propose to simulate the propagation in air of particles involved in TGF production to estimate the radiation doses delivered. The methodology used in this chapter has been presented in Chapter 2. The results and a discussion are presented in Sections 3.2 and 3.3.

The results of this Chapter about radiation doses delivered by TGFs have been published in [Pallu et al., 2021].

3.1 Previous Considerations

Before presenting the results of radiation doses from photons and electrons in TGFs, we mention doses that could be delivered by the same particles in gamma ray glows and by neutrons in TGFs. We present also the configuration of the present study in Section 3.1.3.

3.1.1 Radiation Doses Delivered by Gamma ray Glows

Gamma ray glows have particle fluxes much lower than TGFs. Only few flux measurements have been made *in situ* for gamma ray glows. For instance, Kelley et al. [2015] have measured a gamma ray glow on board an aircraft. They discuss in their paper that the aircraft was in the electron TGF source when the detection have been made, therefore the assumed most harmful part of the event. The measured electron flux was $\sim 1100 \text{ cm}^{-2} \text{ s}^{-1}$. Using equation 2.3, we get a dose rate of $\sim 1 \text{ mSv/h}$ generated. It corresponds to $0.3 \text{ } \mu\text{Sv}$ delivered to someone who would be exposed over one second to the electron TGF source of this glow. From the different measurements made of gamma ray glows on board aircraft [Kelley et al., 2015; Østgaard et al., 2019a], we can estimate that the exposure can last up to several minutes. The dose received in a 10 min exposure, that is a very upper limit corresponding to a 150 km-radius gamma ray glow seen on board an aircraft, would reach 0.2 mSv , which corresponds to about only the dose received for a chest X-ray. Therefore in this study we decided to focus on doses delivered by TGFs.

3.1.2 Radiation Doses Delivered by Neutrons

It is known that neutrons can be produced by TGFs with gamma rays through photo-nuclear reactions, as explained in Chapter 1. However, until now only few neutron measurements have been made coincidently with TGFs [Bowers et al., 2017; Enoto et al., 2017]. Moreover, only a small fraction of gamma rays (those with energies greater than $\sim 10 \text{ MeV}$) will create a neutron, corresponding to a much smaller dose than electrons and photons. Therefore we decided to focus primarily on doses delivered by TGF electrons and photons.

3.1.3 Configuration

The configuration of the situation studied in this section is depicted in Figure 3.1:

- Source altitude at 12 km

3.2. Radiation Doses Results

- 10^{18} photons with energies greater than 1 MeV are produced in total
- RREAs propagate over a distance of ~ 1 km above the source
- Gamma rays are allowed to propagate up to 500 km of altitude – doses delivered by gamma rays are estimated from 1 km above the source, as the total radiation dose between the source and 1 km above will be mainly delivered by the electrons

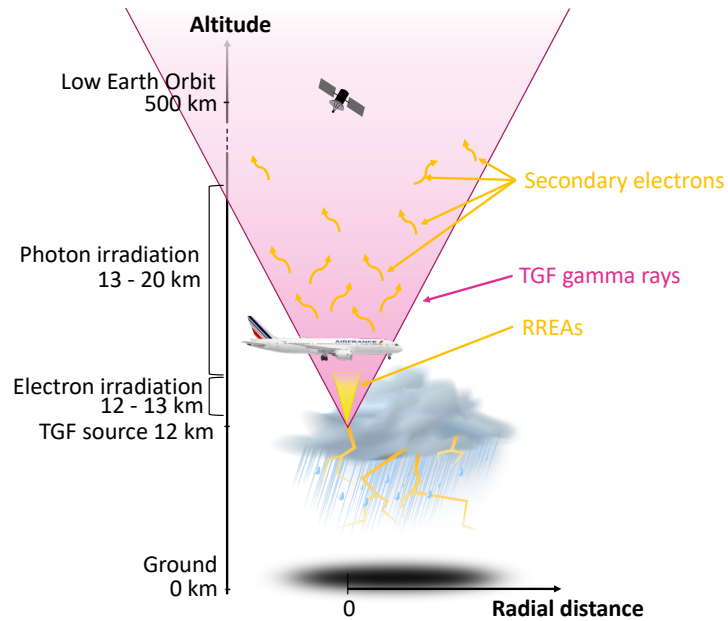


Figure 3.1: Representation of the configuration studied. The pink area represents the TGF. The yellow area is the location of causative RREAs. Secondary electrons are electrons produced by collisions between TGF photons and air molecules. Reproduced from [Pallu et al., 2021].

3.2 Radiation Doses Results

In this section, the results obtained from both models used for electron simulations and from the photon simulations are presented.

3.2.1 Electron Doses: Pure Leader Model

Using the electron energy distribution function $f(\varepsilon, t)$ and the number of electrons $N_e(t)$ from our Monte Carlo simulations, the bremsstrahlung diffusion cross section $\frac{d\sigma_\gamma}{d\varepsilon_\gamma}$ from [Lehtinen \[2000\]](#), the assumption that a typical TGF observed from space produces 10^{18} photons, and the assumptions made about the potential drop (see [Section 2.2.1](#)), we found that 10^{14} runaway electrons need to be produced at the source (i.e., thermal runaway seeds with energy > 3.5 keV injected in the vicinity of the leader tip (see [\[Celestin and Pasko, 2011\]](#)). This number is used hereafter as the number of initial runaway electrons.

Electrons propagate until they slow down in low-field regions. In this case, the [RREA](#) takes place over almost 750 meters in altitude up from the source and about 600 meters in diameter for most of the electrons.

[Figure 3.2](#) presented the electron dose generated for one TGF in less than 1 ms, obtained within the pure leader model in a 2-D cross-sectional view: depending on the altitude and on the radial distance. The position of the leader tip (at an altitude of 12 km) is represented as a red diamond.

The maximum dose delivered by the [RREA](#) is 0.29 Sv, 50 meters above the source. At this distance, 90% of the electrons are contained in a 15-m diameter disk. The energy spectrum of the electrons contained in the 15-m diameter disk, 50 meters above the source is shown in [Figure 3.3](#). This figure presents an instantaneous spectrum obtained when the mean position of electrons reaches $z = 50$ m. A sharp cutoff around 30 MeV observed in the spectrum is explained by the fact that electrons could only gain that much energy from the injection point to the moment they reached 50 m.

The altitude for which the $H^*(10)$ dose produced by the [RREA](#) during less than 1 ms goes below the limit effective dose defining the workers' category A (6 mSv) is 430 meters above the source, and at this altitude, 90% of the electrons are included in a 280-m diameter disk. The altitude for which the dose goes below the regulatory

3.2. Radiation Doses Results

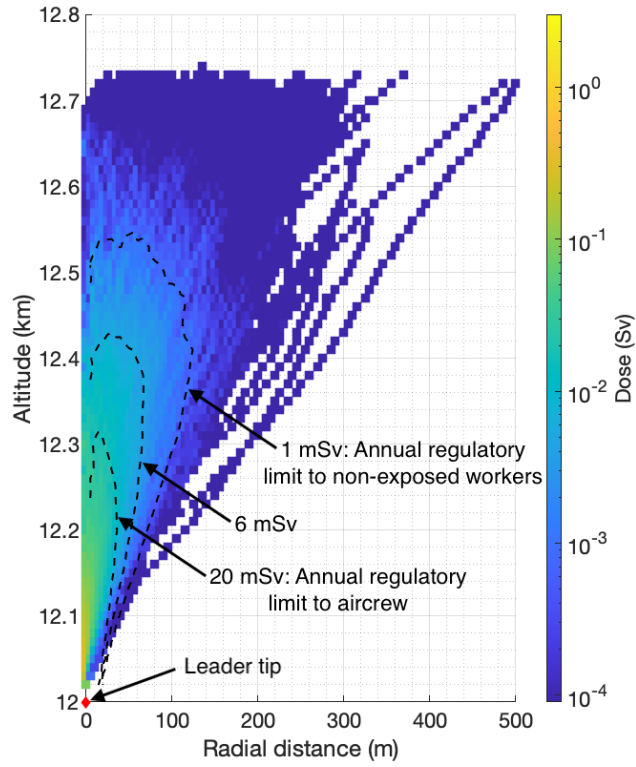


Figure 3.2: 2-D cross-sectional view of the calculated ambient dose equivalent associated with runaway electrons producing a TGF, obtained within pure leader model. The leader tip is represented as a red diamond. The dashed lines are isocontours at 1, 6, and 20 mSv. Reproduced from [Pallu et al., 2021].

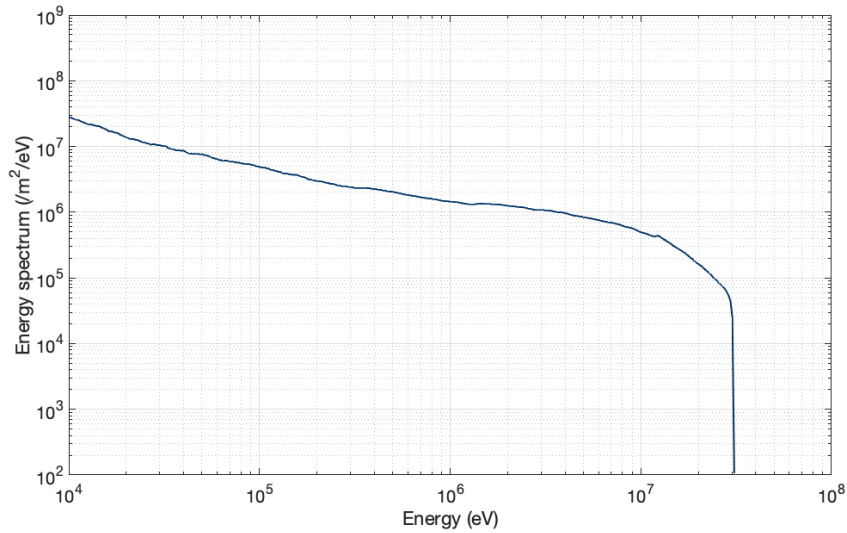


Figure 3.3: Energy spectrum of the RREA electrons contained in the 15-m diameter disk, 50 meters above the source. Reproduced from [Pallu et al., 2021].

annual limit to the non-exposed workers (1 mSv) is 550 m above the source, and at this altitude, 90% of the electrons are included in a 337-m diameter disk.

3.2.2 Electron Doses: Homogeneous Field Model

Two electric field values have been used for the second model consisting in the development of RREAs in a homogeneous field model after an injection of the thermal runaway electrons by a leader: 4 kV cm^{-1} and 5 kV cm^{-1} , normalized to ground level.

For an electric field of 4 kV cm^{-1} normalized to ground level, a source altitude of 12 km and the length of the avalanche region to be 1 km, we found that $6 \cdot 10^{16}$ thermal runaway electrons are needed at the source so as to have 10^{18} photons with energy $> 1 \text{ MeV}$ produced through bremsstrahlung. For an electric field of 5 kV cm^{-1} normalized to ground level, and the same assumptions as for 4 kV cm^{-1} , $4 \cdot 10^{15}$ thermal runaway electrons are needed at the source.

Figure 3.4 represents the dose delivered by the electrons for one TGF during less than 1 ms within a homogeneous electric field model, for at a 12 km altitude, for 4 kV cm^{-1} (Figure 3.4 A) and for 5 kV cm^{-1} (Figure 3.4 B) (scaled to ground level) both extending over a length of 1 km. Panels A.1 and B.1 show the dose produced at the end of a 1-km-long avalanche, at an altitude of 13 km, as a function of the electron beam diameter. Panels A.2 and B.2 show the dose produced as a function of the electron beam diameter and as a function of the altitude inside the avalanche. Panels A.3 and B.3 show the dose as a function of the altitude inside the avalanche for a point source. A striped area indicates the non-physical cases, where the initial radius of the source would be imaginary for such small electron beam diameters at the end of the avalanche region, because of the diffusion process. A spatial 2-D representation of the point source case for electric field magnitudes of 4 kV cm^{-1} and 5 kV cm^{-1} is presented in Figure 3.5 to illustrate the beam diffusion and therefore the dose is shown as constant depending on the radial distant.

The diffusion process is the reason for the non-linear horizontal axis for the

3.2. Radiation Doses Results

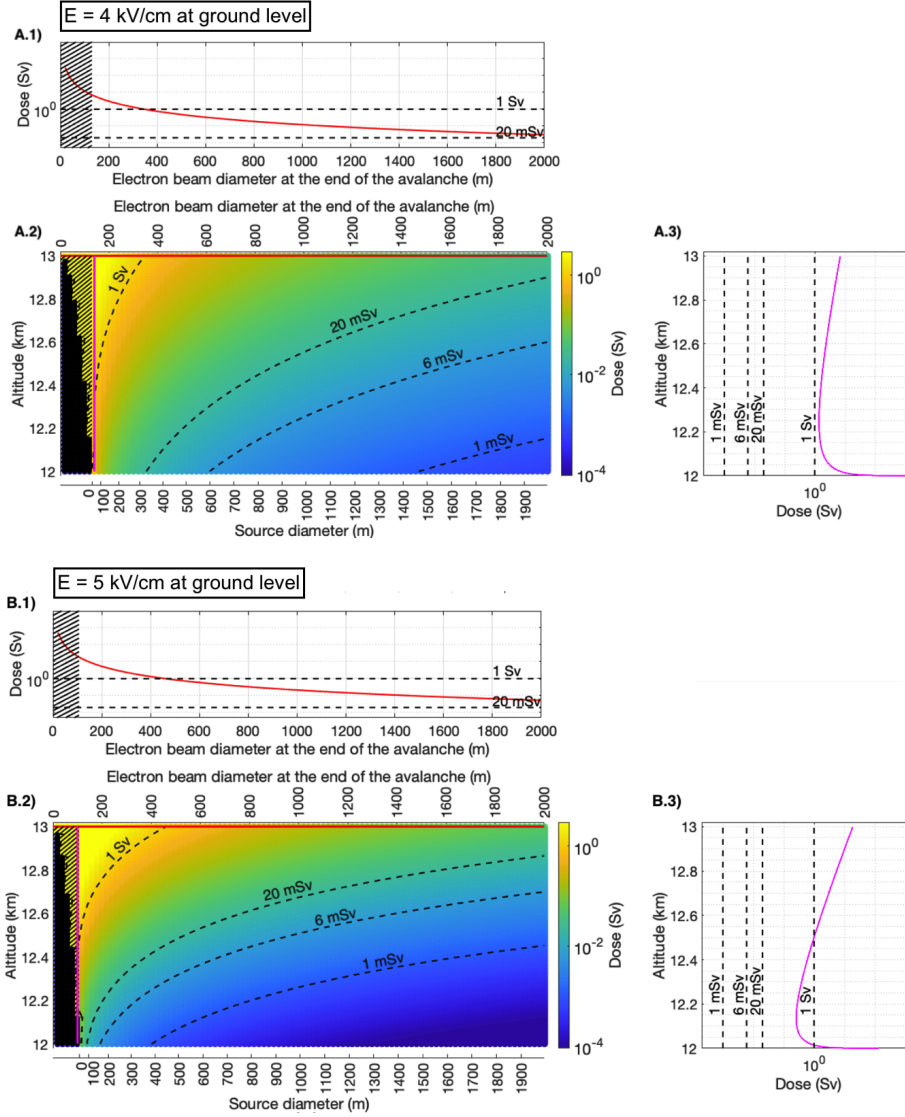


Figure 3.4: Representation of the calculated ambient dose equivalent for electrons, within a homogeneous electric field model. The electric field value corresponds to: (A) 4 kV cm^{-1} and (B) 5 kV cm^{-1} at ground level. The dashed lines represent $H^*(10)$ isocontours. (Panels A.1 and B.1) Dose produced at the end of a 1-km avalanche, at an altitude of 13 km, as a function of the electron beam diameter at the end of the avalanche. (Panels A.2 and B.2) Dose produced inside the avalanche as a function of the electron beam diameter at the end of the avalanche. The black and striped area represents a non-physical situation considering the minimum diffusion diameter of a point source. (Panels A.3 and B.3) Dose as a function of the altitude inside the avalanche for a point source that ends with (A) a 130-m diameter and (B) a 107-m diameter, represented with a magenta line in panels A.2 and B.2. The avalanche length λ and the initial number of runaway electrons N_0 are, respectively, (A) 249 meters and $6 \cdot 10^{16}$ electrons, and (B) 138 meters and $4.1 \cdot 10^{15}$ electrons. Reproduced from [Pallu et al., 2021].

Chapter 3. Estimation of Radiation Doses Associated with TGFs

source diameter, below panels A.2 and B.2. We also consider that we need at least 2 avalanche lengths in order to have electrons following the RREA spectrum at the end of the avalanche. Under this assumption, we found that at this altitude of 12 km, with an avalanche over 1 km, electric fields below 3.4 kV cm^{-1} at ground level are not sufficient to get electrons following a RREA spectrum.

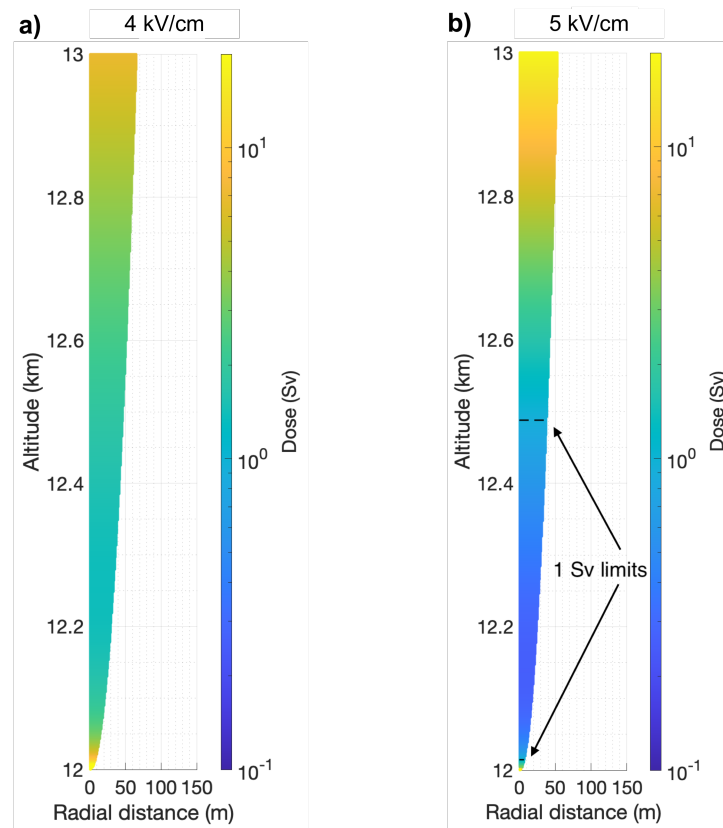


Figure 3.5: 2-D representation of the calculated ambient dose equivalent for runaway electrons accelerated in a homogeneous electric field region, assuming a point source, to illustrate the electron beam diffusion. The dose is thus shown as constant with the radial distant. (a) The electric field value is 4 kV cm^{-1} at ground level. The minimum dose delivered is 1.4 Sv. The dose at the end of the avalanche region is 7 Sv. (b) The electric field value is 5 kV cm^{-1} at ground level. The minimum dose delivered is 0.3 Sv. The dose at the end of the avalanche region is 18 Sv. The colorbar is the same for both plots and goes from 0.1 to 20 Sv. Reproduced from [Pallu et al., 2021].

One major result of this study is that the ambient dose equivalent can reach

3.2. Radiation Doses Results

high values, above regulatory annual limits for aircrew (20 mSv) even for large electron beam diameter. Even for low electric fields as 3.4 kV cm^{-1} simulated but not presented, we found that all along the electron beam the dose is higher than 20 mSv for source diameter up to 650 m, and the dose at the end of the avalanche is higher than 1 Sv for source diameters up to 200 m. In Figure 3.4 A., $H^*(10)$ at the end of the avalanche has a minimum of 30 mSv for the largest beam diameter of 2 km, and it exceeds an extremely high dose of 1 Sv, reaching 7 Sv, for the smaller final beam diameter of 130 m. Along the avalanche, the dose does not fall below 1 Sv for a point source, and 0.5 mSv for a final beam diameter of 2 km.

In Figure 3.4 B, $H^*(10)$ at the end of the avalanche has a minimum of 54 mSv for the largest beam diameter of 2 km, and it reaches even higher values than for the previous electric field value of 4 kV cm^{-1} , with 18 Sv for the smallest final beam diameter of 107 m. Along the avalanche, the dose does not fall below 0.3 Sv for a point source, and $40 \mu\text{Sv}$ for a final beam diameter of 2 km.

For a point source, the dose is extremely high at the very beginning, reaching values of hundreds of sieverts. This is artificial, due to the fact that the number of electrons per unit area is very large, and happens only over 20 m above the point source.

Concerning the electric field value, comparing Figures 3.4 and 3.5, we can say that the greater the electric field, the greater is the dose at the end of the avalanche. The bremsstrahlung photon production frequency per electron ν_γ does not depend on the electric field, but there is a different number of electrons at each moment of time depending on the electric field (through $\lambda(E)$). For a given number of initial electrons, the number of electrons at the end of the avalanche is greater for greater electric fields. Thus, during the avalanche, on average, the number of electrons needs to be lower for a greater electric field to maintain the number of TGF photons to 10^{18} . It is possible to see this effect on the number of initial electrons needed that is $6 \cdot 10^{16}$ electrons for $E = 4 \text{ kV cm}^{-1}$, and only $4.1 \cdot 10^{15}$ electrons for $E = 5 \text{ kV cm}^{-1}$.

3.2.3 Photon Doses

The ambient dose equivalent from photons is plotted in Figure 3.6. In the simulation, because of a cylindrical symmetry, photons are collected in different rings, 50-m large and concentric with the axis of symmetry of the configuration, in order to estimate the fluence as a function of the radial distance, until they reach either an upper virtual screen at 500 km or the ground (see Figure 3.1). This ring-based method associated with a Monte Carlo code creates a lack of resolution along the axis of symmetry, some kilometers above the source (also noticeable in Figure 3.2 for the runaway electron Monte Carlo code); this is a purely numerical effect, due to a weak probability to have particles in the smallest rings. It should not be concluded that the dose is weaker close to the axis, the simulation performed only did not allow to estimate the dose in some of the darkest bins.

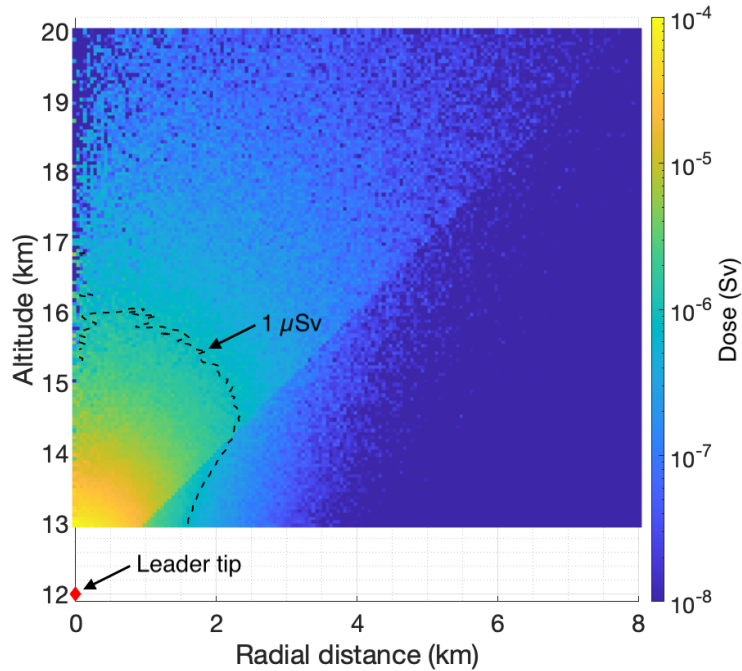


Figure 3.6: Ambient doses equivalent generated by photons as a function of the observation altitude and the radial distance. The red diamond is the position of the photon source, localized at 12 km of altitude. The maximum dose is reached at the closest point to the source region and reaches $90 \mu\text{Sv}$. Reproduced from [Pallu et al., 2021].

The step in the dose along the 45° line from the source is due to the initial momentum distribution of the photons. The three safety limits used in the present work are not plotted here because photon doses are all under these limits, but we plotted the $1 \mu\text{Sv}$ contour as a reference. The maximum of the dose is found closest to the source, that is, 1 km above the source, and reaches $90 \mu\text{Sv}$. It is clear from this simulation, that the dose between the source and 1 km above is higher and could be very high but this is only due to the fact that we chose a point source for the photons. The extent of the highest doses obtained (above $1 \mu\text{Sv}$) is contained in an area of 4 km in altitude and a maximum of 4 km in diameter.

[Bottollier-Depois et al. \[2000\]](#) measured an average flight dose rate for a Paris-Tokyo flight of $6 \mu\text{Sv h}^{-1}$. Assuming a mean dose rate of $6 \mu\text{Sv h}^{-1}$, a 10 h flight leads to $60 \mu\text{Sv}$ received for the passengers. A passenger that would receive the maximum dose generated by the photons would increase its exposure by a factor of 2.5.

3.2.4 Secondary Electron Doses

The radiation dose delivered by the secondary electrons (produced by photon collisions) have been estimated only for the worst position of the photon simulation, that is 1 km above the source. We found that a maximum of $0.6 \mu\text{Sv}$ would be delivered one kilometer above the source, that is less than the dose received during a dental X-ray. For a 10 h flight, this additional dose received by secondary electrons would corresponds to an increase of only 1% of the total flight dose received during the whole flight.

3.3 Discussion

3.3.1 Calculated Doses

The results presented in this chapter give a prediction of ambient dose equivalents produced by electron avalanches that are much larger than photon and secondary

Chapter 3. Estimation of Radiation Doses Associated with TGFs

electron doses. Indeed, runaway electron doses approach or exceed the very high dose of 1 Sv in both models used in this work. Comparing the extent of the areas where doses are delivered, as photons propagate further in the atmosphere, photons deliver doses on a region of about 5-km wide over almost 10-km long. On the other hand, the region of interest for electrons is on the order of 1-km long and 400-m wide (pure leader model) to some kilometers wide (homogeneous field model). Even though the extent could be even larger than for photons, secondary electrons produce doses so small that, to see an impact on the calculation of the total dose received from flights, aircrews would have to find themselves in the vicinity of a TGF several tens of times a year.

Concerning electron doses, the two models used in this work do not give the same results. In particular, the maximum of the delivered doses do not occur in the same part of the avalanche region. For the leader model, the maximum occurs in the first third of the avalanche, mostly due to the very small region close to the leader tip, even though the maximum number of electrons occurs at ~ 320 m from the source point. On the contrary, the homogeneous field model implies the maximum dose to occur at the end of the avalanche, chosen here as 1-km long. This is not true for the particular case of a point source for which the dose reaches very high values at the very beginning of the avalanche.

Our results can be compared to those presented by [Dwyer et al. \[2010\]](#). Their work is comparable to the homogeneous field situation modeled in our study, but uses effective doses in antero-posterior direction, unlike the ambient dose equivalent that we use (see [Figure 2.2](#) for the comparison of the conversion coefficients). They only estimated the dose delivered by electrons at the end of the avalanche as a function of the electron beam diameter. Our results are similar to the TGF doses that they calculated, taking into account that ambient dose equivalent conversion coefficients are greater than effective dose conversion coefficients for energies around 1 MeV. In fact, we found the same results as [Dwyer et al. \[2010\]](#) with effective doses, and presented here an estimation of the dose all along the avalanche region.

These results, especially for the homogeneous field model, were obtained for a very specific case designed to fit our current knowledge of TGFs: source altitude of 12 km, an ambient electric field of 4 or 5 kV cm⁻¹, and the length of the avalanche region of ~1 km. Regarding the homogeneous field model, we note that the variation of the dose along the avalanche depends on the parameters of the problem: electric field value, length of the avalanche and source altitude. These variations can be summarized as follow:

- The higher the electric field, the higher the dose at the end of the avalanche. However, the dose along the avalanche is lower, due to the lower number of initial electrons, as can be seen in Figures 3.4 and 3.5
- The higher the altitude, the lower the dose at the end of the avalanche (e.g., doses at the end of the avalanche for a point source: 12 Sv for 10 km; 7 Sv for 12 km), but with a greater dose along the avalanche
- Longer avalanches imply lower doses along the whole avalanche. This can be easily understood by the fact that since we fix the number of photons produced during the TGF, for longer avalanches, electrons are less compactly packed than for shorter avalanches. For avalanches shorter than 1 km (e.g., 500 m), the dose reaches around 1 Sv all along the avalanche

Despite the variation of these parameters, in particular for lower electric field values (3.4 kV cm⁻¹), lower altitudes (10 km) and longer avalanche regions, electron doses were still approaching the 1-Sv-value at the end of the avalanche. Concerning the pure leader model, the results depend on the initial number of electrons and vary proportionally with it.

3.3.2 Intensity of TGFs

For both models, we used a fixed value of 10¹⁸ photons (>1 MeV) produced at the source of the TGF (called “TGF brightness” in the following), which is in agreement

Chapter 3. Estimation of Radiation Doses Associated with TGFs

with satellite measurements (e.g., [Mailyan et al., 2019]). However, the maximum and the minimum possible brightness of TGFs are still under debate.

Indeed, it is not yet clear if all lightning can produce TGFs but too weak to be detectable by current measurements. Several studies have been published about the population of dim TGFs but the results do not conclude unambiguously on the proportion of weak TGFs. One of the main issues is that the measured near-threshold fluence distribution depends on the satellite and the ground-based lightning detection network used. Given the dependency of the radiation doses generated on the brightness of the TGF, dimmer TGFs imply weaker radiation doses, and therefore should not represent a high radiation risk, as a factor of 100 or even 10 decreasing the radiation dose would lead to doses below the annual regulatory limits.

Regarding the maximum possible brightness of TGFs, for instance Gjesteland et al. [2015] have shown diversity in the intrinsic brightness of TGFs going up to 10^{20} of photons with energies > 1 MeV. Thus, one cannot exclude TGF brightness up to 10^{20} , knowing that all the detectors in space suffered saturation for some TGF events and that Gjesteland et al. [2015], Mailyan et al. [2016], Mailyan et al. [2019], Sarria et al. [2019] and Smith et al. [2020] reported such high values. Of course, TGFs with brightness up to 10^{20} are probably much rarer events, but assuming that the dose depends linearly on the TGF brightness, in principle the associated dose might be 100 times greater for brightness up to 10^{20} . Thus, especially for doses associated with photons discussed in this work, one would obtain significant values, reaching up to 9 mSv, and resulting in 1-km wide areas with levels of radiation exceeding the 1-mSv safety limit.

3.3.3 Attenuation Due to the Aircraft Cabin

On actual airplanes, the aluminum skin is about 1.6 mm. For the A320 airplane, for instance, it goes from 0.8 mm where it is not pressurized, up to 7 mm at the door frames [Rappeneau, K., Air France, personal communication, June 29, 2020]. In this work we choose to model aircraft cabins assuming a 5-mm aluminum skin, to

account for a margin that may include the fact that TGFs are mostly upward, and the floor and the luggage hold below the passengers and crews that could attenuate the radiation.

Electron stopping power value for aluminum in the minimum ionizing range corresponds to 4 MeV cm^{-1} [Berger et al., 2005]. Therefore, the electron spectrum (Figure 3.3) shifts by about 2 MeV to lower energies. The impact on the doses is shown for electrons in Figure 3.7. The dose is slightly attenuated by the cabin, but the difference represents around 30% of its value. One can add that secondary particles will be produced by electrons penetrating the cabin, scattering from many directions. Aircraft passengers will be therefore exposed from a larger solid angle. Secondary particles produced by electron penetrating the cabin would include bremsstrahlung photons, which would have negligible effects compared to the extremely high doses delivered by electrons here, but will also include neutrons, that have the highest weighting factors concerning equivalent dose calculations. Besides the present analysis, no Monte Carlo simulation to determine doses delivered by these neutrons has been run in this work. Even though the exposure would be more diffuse after the aircraft skin, the dose delivered by electrons is not sufficiently reduced to reach values under the safety limits, as we can see in Figure 3.7. Hence, we conclude that the cabin represents poor protection to the high-energy electrons causing TGFs in agreement with Dwyer et al. [2010].

Concerning photons, 5 mm of aluminum let more than 90% of the photons with energies greater than 1 MeV to go through [Berger et al., 2005]. Therefore, there is no significant impact of gamma-rays, and the doses calculated without attenuation in Figure 3.6 are close to those that would be expected to be received by passengers. For secondary electrons, that have weaker energies, the cabin attenuates their dose by 80%, reaching only $0.1 \mu\text{Sv}$.

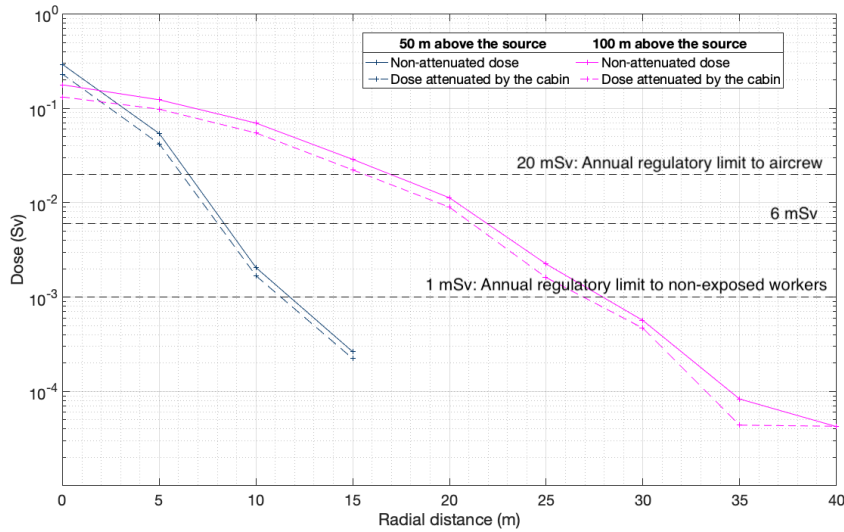


Figure 3.7: Attenuation of the electron dose by the cabin within the pure leader model, with the observation 50 m above the source (blue) and 100 m above the source (magenta). The calculation is made by subtracting 2 MeV from each electron. Electrons with energies lower than 2 MeV are simply removed as they stop in the aircraft’s skin. Reproduced from [Pallu et al., 2021].

3.4 Conclusions

In the work presented in this chapter, radiation dose calculations associated with TGF events are carried out within two production models regarding electrons. A Monte Carlo simulation has been used to model the development of RREAs within a “pure” leader model, and we calculated the fluxes of runaway electrons as a function of altitude considering further avalanches of runaway electrons within the homogeneous field model. We also used a Monte Carlo method to simulate the propagation of photons and secondary electrons in the Earth’s atmosphere. The results of these simulations show that:

- Secondary electrons produce negligible doses (a fraction of microsievert)
- Photons produce doses of a fraction of millisievert (<1 mSv) over an area spanning over several kilometers
- Runaway electrons may produce very significant doses (approaching 1 Sv) in

compact volumes

TGFs are therefore likely to generate high doses through the high-energy electrons involved, although in compact regions: high doses on the one hand, and a low probability for an aircraft to lie in the electron beam on the other hand.

A risk analysis of an event should take into account the likelihood of the event happening and its severity. Even though it seems rather rare for an aircraft to find itself in a TGF source region, that is to say at the wrong place, at the wrong time, the consequences could be serious. Flying away from thunderstorms is probably still the best mitigation strategy, as it is currently impossible to predict where and when a TGF will occur, and it is still difficult to predict the exact spatial and temporal distribution of TGFs around the world. In fact, more and more TGFs are detected as specifically designed instruments are being used. Currently, the ASIM on the ISS, launched in April 2018, is composed of the MXGS instrument designed to detect TGFs [Neubert et al., 2019]. ASIM should extend the known spatial, temporal and fluence distributions of TGFs. Future TGF-focused missions could contribute to answer these questions regarding radiation dose issues and measurements done in thunderstorms will be necessary to confirm doses estimated in this work. Instrumental developments to measure particle fluxes in thunderstorms are presented in Chapter 5.

Moreover, it is worth mentioning that ongoing statistical studies based on data collected using passive dosimeters on board Air France flights have not yet found significant dose increases associated with routes crossing thunderstorms (lower than a few mSv over 3-months integration periods) [Trompier et al., 2014], likely because pilots avoid thunderstorms in most cases. However, the need for a thorough radiation risk assessment for aircraft passengers and aircrews is clearly called by the present work, including an estimation of the probability for an aircraft to find itself in a TGF source region, which is the subject of the next chapter.

Risk for Commercial Flights to be Hit by a TGF

Key Points

- The probability for a commercial flight to be hit by a TGF is estimated by two methods
- Estimation of one hit per flight every 390 years over the whole Air France fleet
- The most exposed route in the world is estimated to be Atlanta-Santiago, with about one hit per flight every 250 years

In order to estimate the probability for an aircraft to find itself in the harmful area of a TGF, in this chapter we present the results of a statistical study using satellite TGF detection data and commercial flight route data. The context is presented in Section 4.1, then the different results and the discussion are presented in Sections 4.2 and 4.3.

4.1 Context

In Chapter 3, we presented the doses delivered by TGF particles through numerical modeling. We predicted that doses delivered by TGF photons should not exceed safety limits used for exposed workers, but doses delivered by electrons may exceed these limits, yet in very compact regions corresponding to the TGF source region. This region is estimated to be approximately 200 m radius large (see Chapter 3).

Chapter 4. Risk for Commercial Flights to be Hit by a TGF

In the following, we will use the term “hit by a TGF” for an aircraft that was closer than 200 m of a TGF source.

The fact that a commercial aircraft is struck by lightning one to two times a year on average [Fisher et al., 1999] indicates that aircraft are not excluded from being hit by high-energy events produced in thunderstorms, even though pilots usually try to avoid thunderstorms. Moreover, it is worth mentioning that aircraft trigger themselves most of the lightning that struck them, leading to the fact that aircraft passing and lightning occurrence are not independent events. Despite this point, aircraft passing and TGF occurrence are considered as independent events in the following study. In the present chapter, we present the results of our estimations of the probability for a commercial flight to be hit by a TGF, depending on the data used concerning the flight route data, taking into account the harmful area of 200 m radius large around a TGF source. Fermi-GBM-detected TGFs are utilized to make a TGF density map, already presented in Section 2.3.1, and two different methods are used for flight routes estimation (as explained in Section 2.3.2): first a simulation of the world traffic from a list of airports; then, the use of real flight data for a single major airline, namely Air France, for which we had access to true flight routes.

4.2 Probability for an aircraft to be hit by a TGF

In this section, probabilities are calculated from flight routes, as explained in Section 2.3.3. Obtaining flight route data for the global air traffic is difficult as it represents a huge quantity of data that is usually not free. Therefore, we decided to use two different ways of getting flight route data in the present study. First, we simulate random flight routes from a list of the 606 biggest airports in the world. On the other hand, we also use real flight data of the whole Air France fleet on the same period as the TGF detection by Fermi (2014–2016).

4.2. Probability for an aircraft to be hit by a TGF

4.2.1 Randomized Routes

The methodology concerning the use of random flight routes is explained in Section 2.3.2. First, we estimate the probability for a commercial aircraft to be hit on a route that has been found to be particularly exposed to TGFs. From this value, we then estimate an upper limit to the probability to be hit by a TGF on the whole air traffic. Finally, we estimate the total probability using random flight route data.

A particularly exposed route

In order to estimate an upper limit on the probability for an aircraft to be hit by a TGF, we look for a particularly used route that is especially exposed. For that, the probability on all the routes from Atlanta (Georgia, USA) airport (airport code: ATL), that is the airport with the busiest traffic in the world, to the 605 other airports has been calculated (see Figure 4.1) using the method presented in Sections 2.3.2 and 2.3.3. The most exposed route is found to be between Atlanta (Georgia, USA) and Santiago (Chile, airport code: SCL). The probability for an aircraft to be hit by a TGF on this route is 6.7×10^{-7} TGF/flight. This corresponds to one flight over 1.5 million of flights that is hit by a TGF on this route. Assuming that the number of flights per week on this route is 16 [flights.com, 2021], it means that on this route, one flight would be hit every ~ 1800 years by a TGF.

Global air traffic: an upper limit

We use the results the probability found for the ATL-SCL route to estimate an upper limit for the probability to be hit by a TGF in a random commercial flight in the world. Assuming the duration of the ATL-SCL flight to be 504 min (with constant aircraft velocity), the probability for an aircraft to be hit per second on this route is then 2.2×10^{-11} TGF/s. With 38.9 million of flights per year [statista.com, 2021], the proportion of short, medium, and long-haul flights stated before in Section 2.3.2 and a mean duration for short-haul flights of 1.5 h, for medium-haul flights of 4.5 h

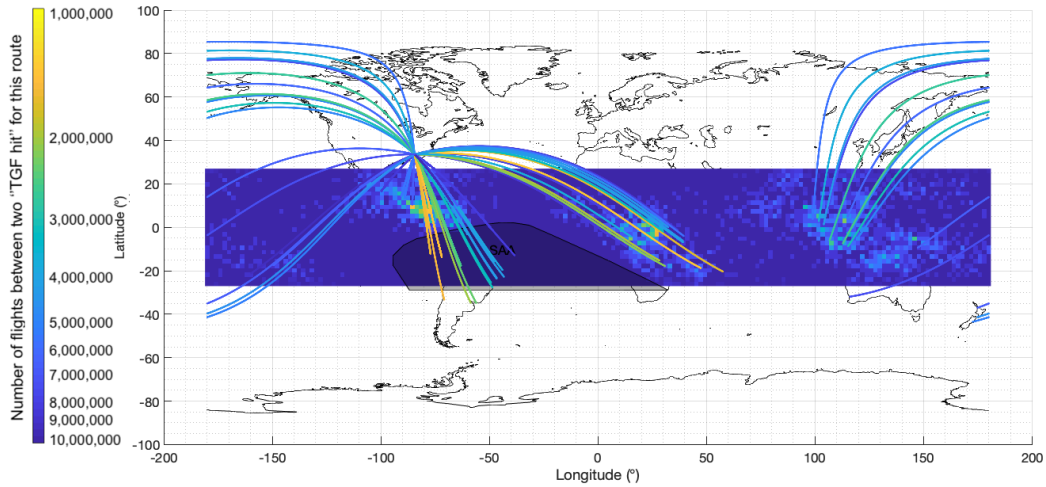


Figure 4.1: Representation of the calculated time (in years) separating two hits of aircraft by a TGF on each Air France routes; these results are plotted above the TGF density map presented in Figure 2.9.

and for long-haul flights of 11 h, we obtain a mean of 6.7 flights hit by a TGF per year in the world for the upper limit.

We emphasize that this is an estimation of an upper limit, therefore an overestimation, of the probability that an aircraft would be hit by a TGF in the world.

Global air traffic: the total probability

In this part, probabilities are calculated from theoretical routes between airports chosen randomly, as explained in Section 2.3.2 to obtain a more precise estimate of the total probability. Five thousand random flights (respectively 893, 679 and 3428 short, medium and long-haul flights) is sufficient to obtain an accurate estimate of the mean probability. The results can be seen in Table 4.1.

Taking into account the proportion of each flight type, the probability for an aircraft to be hit by a TGF on a flight is 1.6×10^{-8} TGF/flight. With 38.9 millions of flights per year, it means one flight every ~ 1.6 years would be hit (within 200 m) by a TGF.

We emphasize that for routes crossing latitudes above or below 26° , the proba-

4.2. Probability for an aircraft to be hit by a TGF

Table 4.1: Table of probability for an aircraft to be hit by a TGF according to its flight type

Flight type	Flight duration	Proportion of the flight type in the world [Wilkerson et al., 2010]	Probability to be hit by a TGF (TGF/flight)
Short-haul	< 3 h	86%	8.2×10^{-9}
Medium-haul	3 h – 6 h	10%	5.6×10^{-8}
Long-haul	> 6 h	4%	7.8×10^{-8}

bility corresponding to the part of the route above or below 26° is set to zero because we do not have TGF data to estimate it. There is a similar issue above the South Atlantic Anomaly (SAA) where no data is available. For these particular routes, the result is slightly underestimated by this procedure. As we do not take into account the altitude of the TGFs nor the altitude of the flights (see later discussion in Section 4.3.2) and since the fact that pilots usually try to avoid thunderstorms is not considered, on the contrary, probabilities are overestimated by these assumptions. The latter point can nevertheless be somewhat unveiled using real route data and evaluating the overestimation caused by ignoring the altitude variability of TGF sources. This is done in the next sections, with real flight data for the whole fleet of Air France between January 2014 and July 2016.

4.2.2 Air France Fleet

We use the list of all actual Air France flight routes that have been performed between January 2014 and July 2016. For each flight, we use the departure airport, the arrival airport, and waypoints recorded during the flight. An interpolation using geodesics is made between the waypoints to complete the routes. Up to 20 waypoints are available for longest trajectories. 700,587 flights have been performed by Air France over this period, representing less than 1% of the totality of the flights

Chapter 4. Risk for Commercial Flights to be Hit by a TGF

in the world. We will use only the 97,868 flights that have routes that go below 26° latitude, which represents 14% of the Air France flights over this period. Over this period, 1,942 TGFs have been detected by Fermi and 55,795 of the 97,868 flights that go below 26° latitude were in flight when a TGF has been detected by Fermi.

Real time distances

For each TGF detected between January 2014 and July 2016, we calculate the location of each in-flight aircraft at the time of the TGF and calculate its distance to the TGF. As mentioned in part 2.3.2, it is worth mentioning that we assume TGF positions to be Fermi's footprint at the moment of the detection. This approximation being done on all TGF positions should not imply big changes in the TGF distribution, given the randomness of the process.

Figure 4.2 shows the location of in-flight aircraft at the time of the TGF on the 22nd July, 2015. The minimum distance with an in-flight aircraft for this TGF is 36 km, which is the shortest distance found between a TGF in the Fermi-GBM catalog [Roberts et al., 2018] and an Air France aircraft over the 2.6-year of route data.

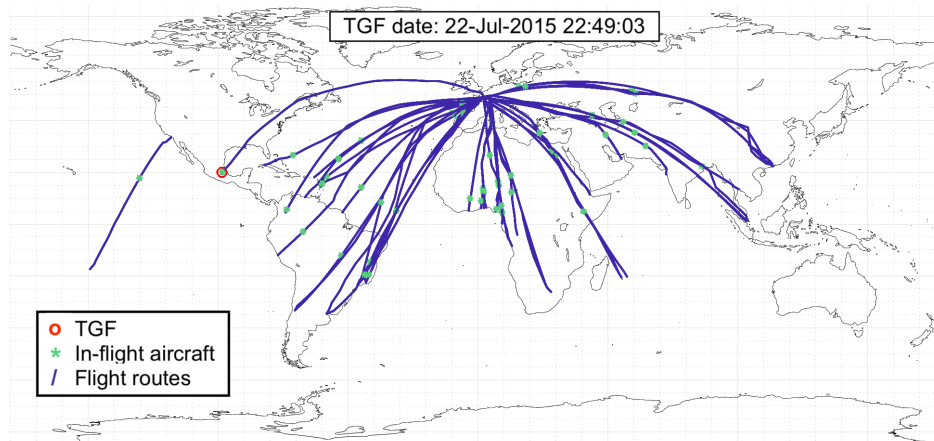


Figure 4.2: Representation of the location of all in-flight Air France aircraft at the time of the detection of a TGF. The TGF plotted has been detected on the 22nd of July, 2015. The green stars represent the location of aircraft. The blue lines are the routes of the aircraft concerned. The red star (hidden by a green star) is the location of the TGF. The shortest distance between an aircraft and the TGF is 36 km.

4.2. Probability for an aircraft to be hit by a TGF

A histogram of the distances between in-flight aircraft and TGFs is showed in Figure 4.3. The mean distance is 9900 km, which is close to the mean distance between two random points on the Earth surface. Only 0.5 % of the 55,795 Air France flights have been at distances below 1000 km from a TGF. We would have hoped to be able to extrapolate this histogram for shorter distances, but seeing the shape of the histogram, we were not able to do it and estimate the probability for an aircraft to be hit using another method. Again, altitudes have not been taken into account for TGFs and aircraft.

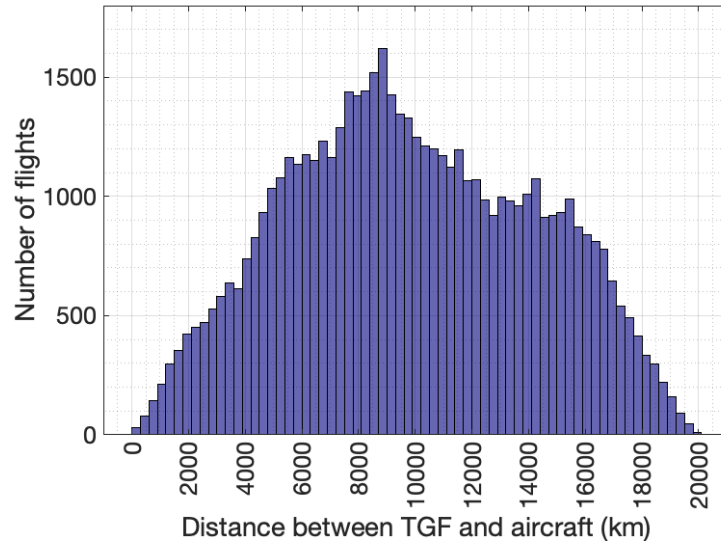


Figure 4.3: Histogram of distances between a TGF and aircraft in flight at the time of the TGF. A total of 55,795 flights are used to calculate this histogram.

Probabilities

We also estimated the probability for each real flight to be hit by a TGF, as done in Section 4.2.1 for randomized flights. The probabilities go from 6.7×10^{-12} to 1.1×10^{-6} , with a mean probability of 8.1×10^{-8} TGF/flight. The route having the higher probability is MEX (Mexico city, Mexico) – BOG (Bogota, Colombia), for which only 2 flights have flown in 2.6 years in the Air France fleet, corresponding to one Air France aircraft hit on this route every 1,200,000 years. However, an estimated

Chapter 4. Risk for Commercial Flights to be Hit by a TGF

number of 6 flights/day on this route [flightconnections.com, 2021] involves that there is one hit per flight every 415 years on this route for all the airlines. Figure 4.4 represents the time between two hits on each route, taking into account the probability and the frequency of flight during the 2.5 years studied. Then, CDG (Paris, France) – JNB (Johannesburg, South Africa) is the most exposed route, representing one flight hit by a TGF every 3,600 years (one hit every 2,600,000 flights and ~ 720 flights/year). The total probability on the whole Air France fleet is 0.0026 TGF/year, corresponding to one hit every 390 years on the whole fleet.

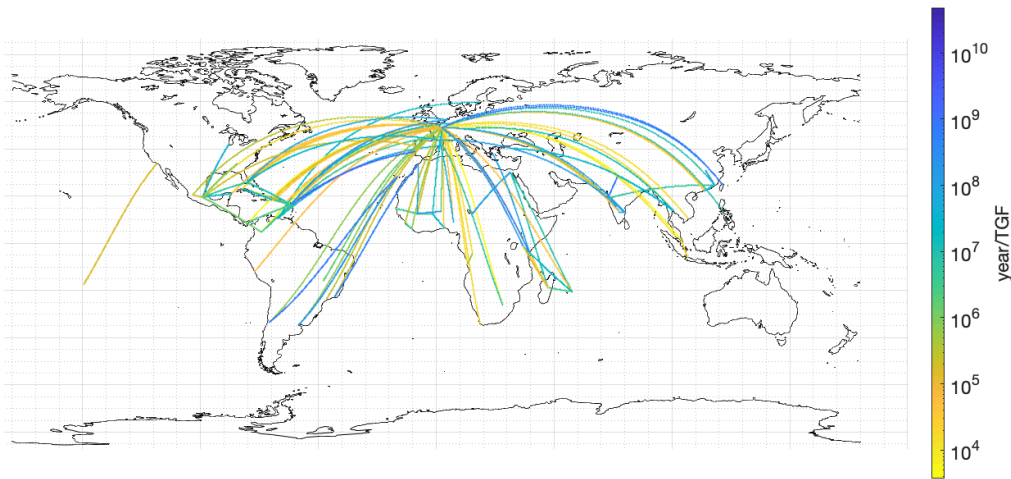


Figure 4.4: Time (in years) separating two hits of aircraft by a TGF on Air France routes.

4.3 Discussion

A few strong assumptions have been made to be able to assess the TGF risk to commercial flights. First, we address only Fermi-detectable TGFs in this work, whereas a population of dim TGFs could increase the TGF density map used. This point is discussed in Section 4.3.1. Then, parameters as the 26° latitude limit and the SAA imply an underestimation of the probability for concerned routes. This point may be improved in using the lightning density map of Figure 1.1 to estimate the TGF density where we do not have Fermi data. The surface covered by Fermi

representing almost 50% of the Earth surface, we do not expect the probabilities to be impacted more than by a factor of 2 taking into account TGFs produced above 26° in latitude. Finally, the fact that altitudes of TGFs and aircraft are not taken into account involves an overestimation that can be quantified and that is explained in Section 4.3.2.

4.3.1 Lower Fluence TGFs

The TGFs addressed in this work are Fermi-detectable TGFs, that are TGF intense enough to be detectable with the limited sensitivity of spaceborne instruments from low-orbit altitudes. Several studies mentioned in Chapter 1 have been performed but do not conclude definitively on the proportion of weak TGFs as it depends on the satellite and the ground-based lightning detection network used.

In case of a large proportion of weak TGFs, the results of our present study would not be strongly impacted as we address only satellite detectable TGFs that are estimated to produce a high number of photons (10^{18}) and thus a sufficiently high number of runaway electrons to deliver the harmful radiation doses estimated by Pallu et al. [2021]. Moreover, Celestin et al. [2015] have shown that weak TGFs would be too dim to reach the RREA spectrum, and would lead to lower energy spectra, and thus to much weaker doses delivered.

4.3.2 Overestimation Made by Ignoring the TGF Altitude Dependence

It is possible to evaluate the overestimation introduced by ignoring the TGF source altitude dependency into account in the probability calculations. We assume that TGFs are produced between 10 and 15 km (e.g., [Cummer et al., 2011, 2014, 2015]), and commercial aircraft to fly between 9 and 12 km. We consider a uniform distribution of upward TGFs and flights over their respective altitude ranges, and a vertical hazardous region equal to the size of the runaway electron acceleration region (~ 1 km) (see [Pallu et al., 2021]).

Chapter 4. Risk for Commercial Flights to be Hit by a TGF

We make the following definitions: TGF_{10-12} is the event “TGF altitude is between 10 and 12 km”, A_{10-12} is the event “the aircraft altitude is between 10 and 12 km”, h_A is the aircraft altitude, and h_{TGF} is the TGF altitude. The difficulty arises from the fact that these events are not all independent. The probability for an aircraft to find itself within 1 km above a TGF is the following:

$$\mathcal{P} = P(TGF_{10-12} \cap A_{10-12} \cap h_A > h_{TGF} \cap |h_{TGF} - h_A| < 1 \text{ km}) \quad (4.1)$$

Conditional probability definition gives:

$$\begin{aligned} \mathcal{P} &= P(h_A > h_{TGF} \cap |h_{TGF} - h_A| < 1 \text{ km} \mid TGF_{10-12} \cap A_{10-12}) \\ &\quad \times P(TGF_{10-12} \cap A_{10-12}) \end{aligned} \quad (4.2)$$

Since these can be considered as independent events, the probability that the aircraft and the TGF happen both between 10 and 12 km is:

$$P(TGF_{10-12} \cap A_{10-12}) = \frac{2}{5} \times \frac{2}{3} = \frac{4}{15} \quad (4.3)$$

As illustrated in Figure 4.5, given that the aircraft and the TGF are in the range 10-12 km, the probability that the aircraft is above the TGF and less than 1 km above it, can be calculated as:

$$\begin{aligned} &P(h_A > h_{TGF} \cap |h_{TGF} - h_A| < 1 \text{ km} \mid TGF_{10-12} \cap A_{10-12}) \\ &= P(h_A > h_{TGF} \mid TGF_{10-12} \cap A_{10-12}) - \\ &P(|h_{TGF} - h_A| > 1 \text{ km} \mid h_A > h_{TGF} \cap TGF_{10-12} \cap A_{10-12}) \\ &= \frac{1}{2} - \frac{1}{8} = \frac{3}{8} \end{aligned} \quad (4.4)$$

Finally, the probability for an aircraft to find itself within 1 km above a TGF,

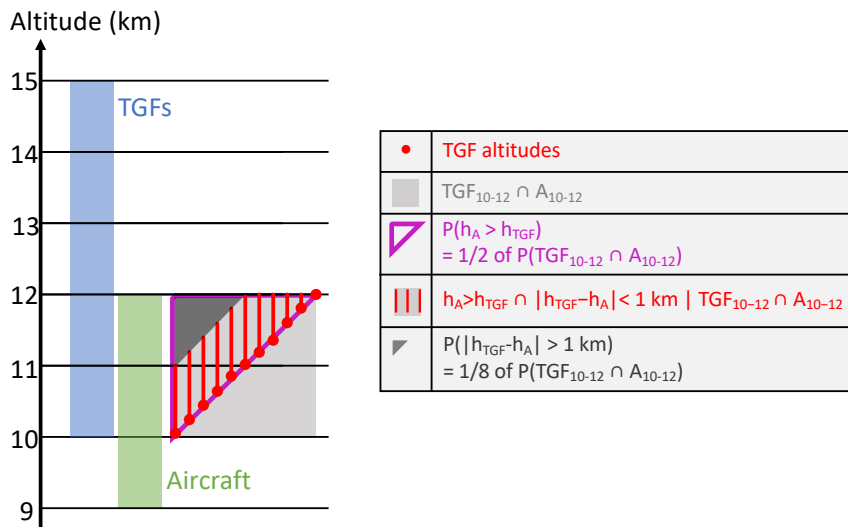


Figure 4.5: Illustration of the events configuration. The proportion of the red hatched area of the light grey square corresponds to the probability that an aircraft is hit by a TGF, given that both are in the range 10-12 km. The magenta area corresponds to the area where the aircraft is constrained to be above the TGF. The dark grey area corresponds to the area where the aircraft is above but too far (>1 km) above the aircraft.

according to equation 4.2, is:

$$\mathcal{P} = \frac{3}{8} \times \frac{4}{15} = 0.1 \quad (4.5)$$

We have verified numerically this method using various altitudes and dangerous range extents for aircraft and TGF locations drawn randomly. One finds that the probability for an aircraft to be hit by a TGF as reported in the present study is overestimated by a factor 10.

4.4 Conclusions

In this work, we have carried out a statistical study to estimate the probability of a commercial aircraft to be hit by a TGF. We used the data of more than 2800 TGFs reported in the first Fermi-GBM TGF catalog [Roberts et al., 2018]. Concerning

Chapter 4. Risk for Commercial Flights to be Hit by a TGF

aircraft flight data, we used two different methods. First, randomized routes between airports have been simulated whereas on the second hand we used real flight data from the airline Air France over 2.6 years.

In the first part of the study, we show that the probability for a commercial aircraft to be hit by a TGF is estimated to be once every ~ 2 years in the world. Some assumptions and lack of data bring an uncertainty on the evaluation of this probability, for instance, the unavailability of data above the SAA and above 26° latitude, the altitude distribution of TGFs, and the routes effectively followed by the pilots who try to avoid thunderstorms when possible. Concerning the TGF altitude distribution, we estimated in Section 4.3.2 that the overestimation could be of a factor of ~ 10 , changing the high rates estimated in Section 4.2.1 to be lowered from ~ 7 hits/year to 1 every 1.4 year for the upper limit and from 1 every 1.6 years to one every 16 years for the total probability with random routes.

Concerning the method utilizing true routes, the second part of the present work uses real data to represent better the routes actually flown by the pilots, in addition to remove the bias associated with randomly picking airports. With these data from the Air France airline over 2.6 years, we found that one aircraft would be hit every 390 years on the whole fleet. Using the fact that Air France flights represent $\sim 1\%$ of the global air traffic, one can extrapolate to the global air traffic and gets one hit every ~ 4 years, that is in the same order of magnitude as found using randomized routes. This probability is considered as low, especially as we still do not take the TGF and aircraft altitude into account, the latter decreasing this probability by a factor of ~ 10 and most significantly that pilots avoid thunderstorms whenever possible.

Gamma ray Spectrometer: Development & First Results

Key Points

- Development of a new gamma ray spectrometer to detect gamma ray glows and TGFs in close proximity
- Neutron detection is performed through a pulse shape discrimination (PSD) method using a plastic scintillator
- Definition of an observation strategy for long-duration balloon campaigns (real-time analysis to limit the quantity of data)
- First results of balloon flights performed in fair weather

In parallel with the theoretical studies presented in Chapters 3 and 4, we have developed a new lightweight gamma ray spectrometer, XStorm, designed to detect TGFs and gamma ray glows aboard aircraft (typically balloons and planes). Indeed, we plan to fly the detector under balloons in the vicinity of thunderstorms to get closer to the sources of these events over long durations, in the framework of two projects funded by the French Space Agency (CNES): OREO and STRATELEC (see Chapter 1). From the first specifications to the readiness for a measurement campaign, we present the science objectives (Section 5.1), the different characteristics (Section 5.2), and the first results obtained in fair weather conditions with the detector (Section 5.3).

5.1 Science Objectives

The main objectives of the gamma ray spectrometer are to detect atmospheric electric events like gamma ray glows usually produced at thunderstorm altitudes, their high altitude (20 km) counterpart, that was recently reported by Østgaard et al. [2019a] and TGFs. In fact, the spectrometer will fly under super-pressurized balloons in the intertropical region (see Chapter 1) to get closer to the sources in thunderstorms than would be possible using satellite. First, this type of measurements would help to understand physical processes that are still uncertain about the context leading to the acceleration and multiplication processes. Super-pressurized balloons moving with a low velocity in the atmosphere will be ideal to explore the source geometries and the time dynamics of gamma ray glows, that is difficult to study by plane or smaller balloons. It will also bring informations to quantify the occurrence frequency of these events, and to confirm the results presented in Chapter 3 about radiation dose estimated associated with TGFs and in Chapter 4 about the TGF density. Considering the spectrometer high frequency measurement abilities, it should be possible to detect a time construction in the counts for a TGF or a gamma ray glow. Finally, the link between TGFs and gamma ray glows can be study with such measurements [Smith et al., 2018; Wada et al., 2019].

Additional secondary objectives that can be addressed are phenomena leading to an increase of high-energy radiation in the lower stratosphere, such as Solar Energetic Proton (SEP) events, creating gamma rays in the atmosphere that could be detectable, and GRBs that might also be detectable at these altitudes.

5.1.1 Gamma ray Glows

Gamma ray glows are enhancements of the background radiation in thunderstorms, which can last from seconds to tens of minutes and are not fluent enough to be detected far away (such as by satellite like TGFs) from the thunderstorm. As they are presumably more frequent than TGFs and that they last longer, they are the

first science objective constraining the design of this spectrometer. Moreover, as they are run by the same physical processes as TGFs, namely RREAs, and that they can occur at the same time [Smith et al., 2018; Wada et al., 2019], studying gamma ray glows also helps understand TGF production mechanisms. Therefore, the scientific aims are to investigate runaway electron acceleration processes, study their link with cosmic rays, and to explore what is the impact of gamma ray glows on the thunderstorm electrical system [Kelley et al., 2015] and the impact of the thunderstorm electrical system on gamma ray glows, for instance their link with lightning.

Recently, two gamma ray glows have been detected at 20 km, a high altitude compared to thunderstorms [Østgaard et al., 2019a]. They were detected on-board an ER-2 aircraft over the continental United States. They also measured the electric field value and tried to explain the measurements using numerical simulations. However, the charge structure of the thunderstorm was not in agreement with the configuration that could explain photon fluxes detected at 20 km. These measurements introduce new questioning concerning where and how gamma ray glows can be produced.

Finally, both types of glows are difficult to characterize in space and time because of the fact that aircraft and balloons do not usually stay for a long time in the glow to see the ending of the event (time dynamics) whereas ground measurements do not allow to probe the space extent (source geometries), except for ground measurements made with networks of ground stations [Torii et al., 2011].

5.1.2 Terrestrial Gamma ray Flashes

As previously said in the introduction, TGFs last less than 100 μ s, are very fluent and produce photons up to \sim 40 MeV energies. The aims in detecting TGFs are to observe these events in close proximity and to quantify the associated radiation doses in thunderstorms. In fact, up until now only estimations by calculation have been made (see Chapter 3 and Pallu et al. [2021]). One of the objectives is also to detect

Chapter 5. Gamma ray Spectrometer: Development & First Results

radionuclide and neutron signatures that have been predicted and demonstrated to be produced by TGFs (e.g., Rutjes et al. [2017]; Enoto et al. [2017]; Bowers et al. [2017]) but have only been detected few times on the ground. For instance, Bowers et al. [2017] have detected neutrons probably produced by a TGF and Enoto et al. [2017] have detected a 511 keV line corresponding to the electron-positron annihilation over long durations, likely associated with the production of neutrons.

Even though TGFs are now frequently detected by different means of measurement, they have been discovered and are still mostly detected by satellites. Ground-based measurements are now quite frequent as well, especially thanks to the Telescope Array that is continuously able to detect downward TGFs [Abbasi et al., 2017, 2018; Belz et al., 2020]. However, airborne measurements of TGFs have been performed only twice [Smith et al., 2011a; Bowers et al., 2018], and TGF detections with our gamma ray spectrometer during a balloon campaign is likely to add new information on the characteristics of the sources.

5.2 Instrument Overview

XStorm (Figure 5.1) is a gamma ray spectrometer designed to detect gamma ray glows and TGFs near the sources, therefore with a high particle flux. The detection principle is based on scintillators associated with silicon photomultipliers (SiPMs). Scintillators are materials whose main property is to scintillate, that is to say they emit a quantity of optical photons, proportional to the energy deposited in the scintillator by incoming ionizing particles. Several types of scintillators exist. For our purpose, we chose to use two of them: a Bismuth Germanium Oxide (BGO) crystal and a plastic scintillator of type EJ-276, contained in the red box in Figure 5.1 that allow us to discriminate neutrons, electrons, and photons. In this section, we present the detailed principle of the detector and its characteristics.

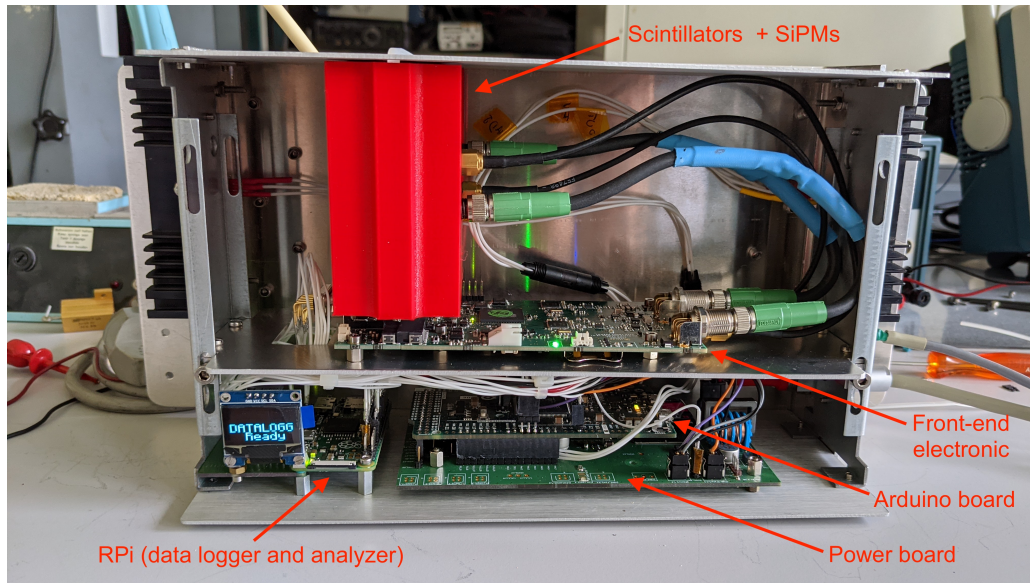


Figure 5.1: XStorm adapted for Strateole-2 campaign (mechanical, communication and power interfaces)

5.2.1 Design Philosophy and Overview

XStorm has been developed to obey usual constraints concerning balloon on-board instruments. In particular, XStorm has a low cost of $<4,000$ \$, to mitigate the risk of no recovery, and a low power consumption, estimated to be ~ 8 W. It is contained in a steel and aluminium box with the following dimensions: $50 \text{ mm} \times 160 \text{ mm} \times 100 \text{ mm}$. It weighs less than 2 kg. It is composed of:

- one BGO scintillator: cubic shape with 1" side, packed in a light-tight box
- one plastic scintillator EJ-276 from Eljen Technology: cubic shape with 1" side, packed in a light-tight box
- two silicon photo-multipliers (SiPMs) C series, 30035 from Onsemi. They are $3 \text{ mm} \times 3 \text{ mm}$ and are composed of 4774 microcells of $35 \mu\text{m}$
- front-end electronics, with one channel for each scintillator. Two different ADCs are used, 40 MHz for the BGO channel and 200 MHz for the plastic channel that has a shorter decay time (tens of ns for the fast component)

Chapter 5. Gamma ray Spectrometer: Development & First Results

- a Raspberry Pi Zero used as a data logger and data analyzer
- a microcontroller board for the communication interface with the on-board computer (OBC)
- a power adaptation board

The decay time of the BGO scintillator is ~ 300 ns, and the decay times of the plastic scintillator are shorter, but depends on the particle type. The latter point is explained in Part 5.2.3.

The front-end electronics associated with the two channels using two scintillators and SiPMs and the signal analyzer using a FPGA have been developed in collaboration with a French company, Icohub, who develops detectors to monitor different types of radiation and dosimetry.

The detection principle is the following. When a particle goes through a scintillator, the quantity of energy deposited by the particle in the scintillator is proportional to the quantity of light collected by the SiPMs. In the case where there are more photons than microcells in the SiPM, the signal can saturate the SiPM. The front-end electronics filter the light pulse signal, and the light pulses are then digitized by the ADC. The FPGA can then analyze the signal to detect pulses and calculate their integral. A threshold is chosen to detect pulses, and the integral is calculated in two parts over $1 \mu\text{s}$ for each pulse as showed in Figure 5.3. These two parts allow, on the plastic channel, to discriminate neutrons from gamma-rays thanks to the Pulse Shape Discrimination (PSD) method, explained in Section 5.2.3. On the BGO channel, we use this feature with a separation at $0.6 \mu\text{s}$ to reject fake pulses observed during flight caused by highly energetic particles present at high altitude. We refer to these events in Section 5.3.4. An electron/gamma ray discrimination can be performed statistically by comparing the proportion of counts in each detector, knowing that electrons will be detected almost in the same proportion in both BGO and plastic scintillator, but gamma rays are detected more efficiently in the BGO.

The arrival time of the particle is measured within 100 ns UTC. This is reached

5.2. Instrument Overview

synchronizing the GPS Pulse Per Second (PPS) signal with the FPGA oscillator that runs at 100 MHz. The 100 MHz frequency could give a 10 ns precision but we only keep the precision at 100 ns. The 100 ns precision UTC is very important for TGF studies as it allows the comparison of our data with that obtained by lightning detection networks. In Table 5.1, one can find a summary of the performances of the spectrometer.

Time accuracy	100 ns UTC
Energy range	~400 keV – 20 MeV
Precision in energy	~20%
Maximum count frequency	1 MHz
Particle discrimination	Photon/neutron (plastic) Photon/electron (statistically)

Table 5.1: Performances of the gamma ray spectrometer.

5.2.2 Energy Range and Time Performances

The spectrometer is able to measure energies between ~400 keV and 20 MeV, with a 20% resolution at 511 keV, taken at FWHM. This low resolution is not a problem for the detector as TGF and gamma ray glow spectra do not show any radiation lines that we would like to detect with a high resolution. A background spectrum acquired in 4 hours at ground level has been plotted in Figure 5.2. Three lines from the background have been identified and used for the energy calibration: potassium (^{40}K) at 1.462 MeV, bismuth (^{214}Bi) at 2.204 MeV and thallium (^{208}Tl) at 2.615 MeV. To limit the temperature effect on the energy measure, namely the spectrum expansion when the temperature gets colder, a system of temperature compensation has been implemented to vary linearly the SiPM voltages as a function of the temperature.

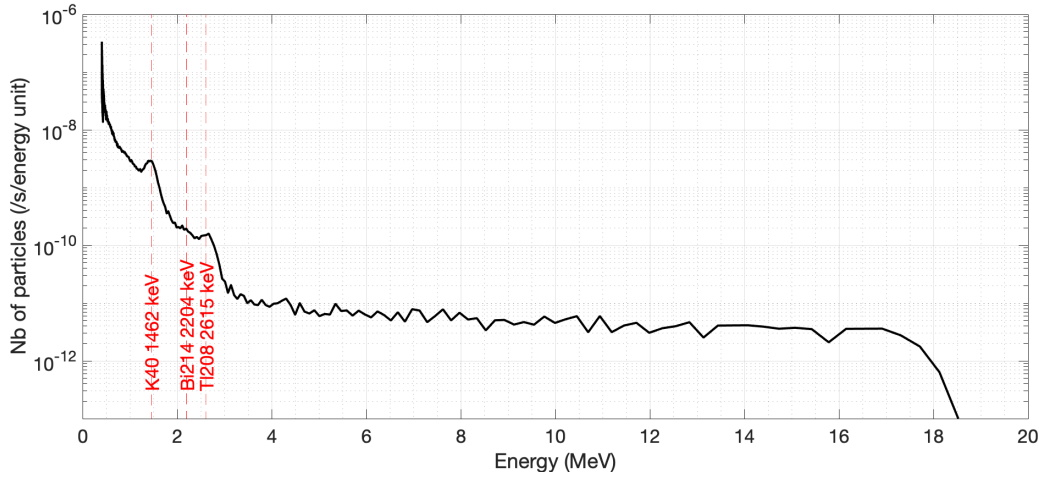


Figure 5.2: Spectrum acquired in 4 hours, at ground level, in Orléans, France. Three gamma ray lines from the background have been identified and used for the energy calibration: potassium 40 at 1.462 MeV, bismuth 214 at 2.204 MeV and thallium 208 at 2.615 MeV.

Data of every single particle detected is collected. In other words, for every particle that goes through the scintillator (and that deposits enough energy to be above the threshold), both integral 1 and integral 2 described in Figure 5.3, and the arrival time within 100 ns precision UTC are saved. The quantity of data produced can therefore be important, according to the existing particle fluxes. For information, the data encapsulation used by XStorm is presented in Appendix A. For balloon flights with payload recovery, it is usually not a problem thanks to SD cards that can hold a sufficient amount of data for several months of data. However, sometimes (for instance, with Stratéole-2 super-pressurized balloons) no recovery is possible, thus data have to be transmitted through satellite communication (for instance with an Iridium link) that is limited because of the expensive costs. For this reason we developed a second working mode, explained in Section 5.2.4, in which we collect light data as survey data, and save the whole data only when an event has been detected. Also for this reason, we developed an event-based detection system that is also explained in Section 5.2.4.

As mentioned in Part 5.2.1, the measurement window is fixed to 1 μ s. The spec-

trometer is a nonparalyzable detector and can record correctly count rates up to ~ 970 kHz. We deduce an effective dead time of $\sim 1.030 \mu\text{s}$ for each particle detection. Only very energetic particles, probably protons, can blind the electronics for a few tens of microseconds. This phenomenon is also followed by other instrumental effects, that are discussed in Section 5.3.4. Pulse pile up is possible for pulses separated by $< 1 \mu\text{s}$. For these pulses, the number of counts detected and the energy of the pulse recorded will both be wrong. There is no possibility to find out that two particles have hit the detector in less than $1 \mu\text{s}$ using the data that are recorded (arrival time and the two integrals). This particularity has therefore to be kept in mind in analyzing data with a high count rate.

5.2.3 Pulse Shape Discrimination Method for Neutron Detection

The scintillation process can be divided into 3 parts. First, the *fluorescence* process that corresponds to the prompt emission of optical photons from an excited material. Then, two other processes are present: the *phosphorescence* and the *delayed fluorescence*. The *phosphorescence* emits photons with lower energies than the *fluorescence* whereas the *delayed fluorescence* emits in the same range of energy as the initial *fluorescence* but with a time delay, due to more transitions in the energy levels of the molecule. The *delayed fluorescence* is the reason why the light emitted by the scintillation process appears to be affected by several exponential decay times [Knoll, 1989].

The main two decay times, called *fast* and *slow* components, and especially the slow component, depend on the nature of the radiation, and can therefore be used to differentiate incident particles. This method is used to quantify the neutron flux, but we do not use it to quantify their energy. The method based on differentiating the radiation type using the shape of the pulse produced is called the Pulse Shape Discrimination (PSD) method. The possibility of obtaining PSD in plastic scintillators was first shown by Brooks et al. [1960]. We use the EJ-276 plastic scintillator from Eljen Technology, since good results have been obtained with this plastic for

Chapter 5. Gamma ray Spectrometer: Development & First Results

the PSD (e.g., [Grodzicka-Kobylka et al., 2020, 2021]). Neutrons detected by association of plastic scintillator with PSD method are mostly fast neutrons. In fact, elements with a high thermal cross-section such as ${}^6\text{Li}$, ${}^{10}\text{B}$ or ${}^{113}\text{Cd}$, need to be present to absorb thermal neutrons, and this is not the case for EJ-276. On the other hand, fast neutrons interact efficiently with the plastic scintillator EJ-276. Gamma rays and neutrons have however a different ionization mechanism, involving the difference in the decay time components [Bertrand et al., 2015]. Whereas gamma rays create delta electrons through Compton scattering, exciting molecules on their path, that are able to de-excite on the same time scale as the prompt fluorescence mechanism, neutrons undergo elastic scattering producing a recoil proton. Interactions between two excited molecules (triplet states) produced by the proton ionization involves a delayed fluorescence (see [Bertrand et al., 2015]). In fact, this interaction is more frequent with protons than with electrons due to the fact that protons produce a higher ionization density along its path.

In order to use this method to discriminate neutrons from photons, without saving the whole signal, we apply the PSD method in calculating a ratio Q between the first part of the integral of a pulse and the total integral of the pulse (e.g., [Cieřlak et al., 2019]):

$$Q = \frac{I_2}{I_1 + I_2} \quad (5.1)$$

I_1 and I_2 are the partial integrals spanning over ranges illustrated respectively in blue and in red in Figure 5.3. Plotting this ratio as a function of the total integral of each pulse $I_1 + I_2$, a characteristic plot with two branches, one corresponding to photon pulses and the other to neutron pulses can be easily noticed. The separation rate of the two branches is dependent on the choice of the separation ratio between I_1 and I_2 . After measurement tests with a neutron source (Californium ${}^{252}\text{Cf}$), a separation of the integral calculation at $0.1 \mu\text{s}$ appears to be the best choice for our detector.

An example of a measure with the neutron source is showed in Figure 5.4, where

5.2. Instrument Overview

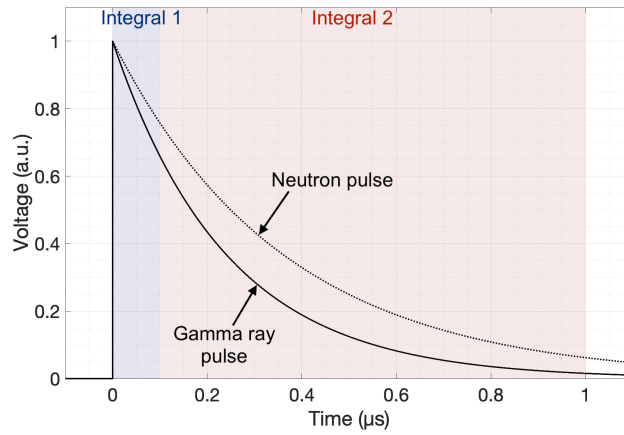


Figure 5.3: Integral calculations with the plastic channel. The first integral is calculated between 0 and $0.1 \mu\text{s}$ and the second one is calculated between 0.1 and $1 \mu\text{s}$. This is made to perform the Pulse Shape Discrimination.

the two branches are identified. At ground level and without the neutron source, the branch corresponding to neutrons cannot be identified as almost no neutrons are present. With this source and this technique, we measured 8% of neutrons, 48% of gamma rays among the particles detected. 44% of the particles could not be identified because of the fact that weak energies lead to $I_2 = 0$ and therefore $Q = 0$.

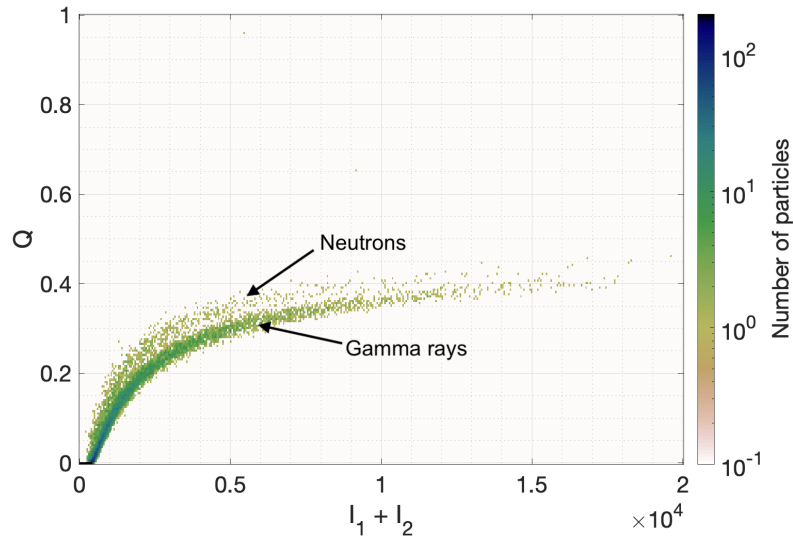


Figure 5.4: PSD representation that allows to discriminate neutrons from gamma rays. Data have been obtained with XStorm exposed to a neutron source (Californium ^{252}Cf).

Chapter 5. Gamma ray Spectrometer: Development & First Results

Decay times assumed for EJ-276 scintillators are 13, 35, 270 ns for gamma rays and 13, 59, 460 ns for neutrons [EljenTechnology, 2021].

However, SiPM filters extend the pulse duration, and thus modify their characteristic decay times [ONSEMI, 2021]. Thus, to be closer to the electrical pulses measured by our scintillators and SiPMs, we acquired some pulses (~ 40) with XS-torm plastic scintillator. They have been recorded during the experiment with the neutron source of Figure 5.4. Trying to fit them with a simple model $\propto \exp(-\frac{t}{\tau})$ using only one decay time τ has given two types of pulse: the majority of them with a fitting decay time of ~ 240 ns, and 5 of them with a fitting decay time of ~ 360 ns. We assume that 240 ns is the decay time for gamma ray pulses and that 360 ns is the decay time for neutron pulses. Pulse shapes with decay times using these values are shown in Figure 5.3.

We developed a toy model to understand the influence of the different parameters of the detector. Simulating pulses of different amplitudes with both decay times, and adding a Poisson noise, we plot the obtained theoretical PSD representation in Figure 5.5(a). Two branches are clearly distinguishable. The upper one corresponds to the neutrons and the lower one to the gamma rays. The proportion of neutrons and photons determined with Figure 5.4 is used for this simulation, namely in the identified particles there were 15% of neutrons and 85% of gamma rays.

Another example of neutron measurement is shown in Figure 5.12, acquired during a lightweight balloon flight. During the flight, neutrons represented about 1% of the particle detected on the plastic scintillator. Almost no neutrons are detected on the ground because of their very rare presence at this altitude.

Both of these measured PSD representations showed Q decreasing with the lowest total energies, on the contrary to the theoretical representation shown in Figure 5.5(a) that has Q almost constant (with respect to the poisson noise) as a function of the energy. This difference is due to the presence of two different thresholds implemented in the spectrometer. The first threshold crushes voltage values that are lower than threshold, which are thus assumed to be zero. The pulses are then

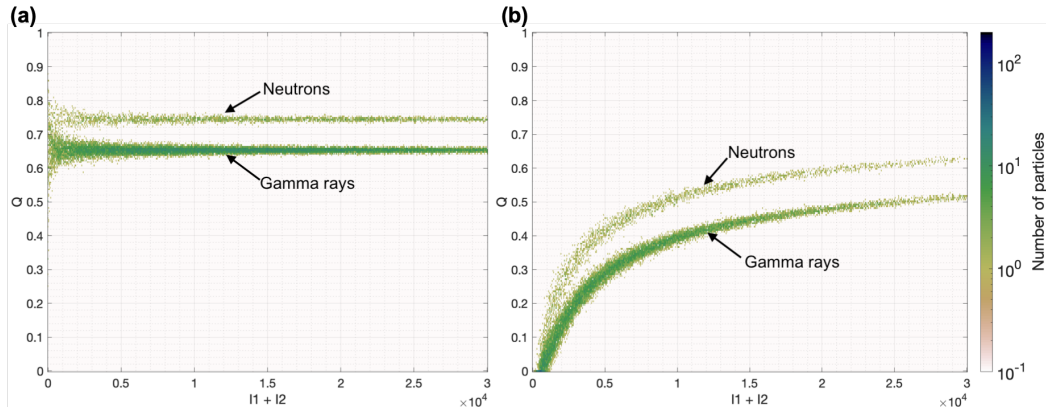


Figure 5.5: Simulation of neutron and gamma ray pulses. (a) PSD representation that allows to discriminate neutrons from gamma rays. (b) PSD representation, with addition of the two thresholds discussed in Section 5.2.3. Both representations have been obtained by simulating pulses with decay times of 240 ns and 360 ns, different amplitudes and a Poisson noise.

shifted to lower voltage values. The second threshold implemented is a detection threshold, which is used as a criterion to detect a pulse. These characteristics have been implemented on the theoretical PSD representation in Figure 5.5(b) and the decrease in the lowest energies is visible. The differences between the theoretical (Figure 5.5(a)) and the measured (Figure 5.4) plots depend on the decay times, the thresholds, and the spectrum of the particles. Particularly, the asymptotic value of the branches are determined by the decay times of the pulses, that undergo probably a modification by the front-end electronics, hence the difference with the decay times determined experimentally after the SiPM.

5.2.4 On-board Software

In order to limit the quantity of data produced by the spectrometer, especially during balloon campaign where instruments are not recovered at the end of the flight (for instance, on board Stratéole-2 gondolas our uploading rate is limited to 10 MB/day), a survey mode and an event detection system have been developed. The latter allows to transmit the whole data (arrival time and integrals of every particle, called high resolution data in the following) to the ground in case of the

Chapter 5. Gamma ray Spectrometer: Development & First Results

detection of an interesting event (namely a gamma ray glow or a TGF).

Survey data mode

The survey data mode converts the high resolution data that contain each particle data (arrival time and two integrals) into more compact data. One low resolution spectrum is calculated every second with a 10 energy bin resolution, and one high resolution spectrum is calculated every hour with a 1000 energy bin resolution in order to be able to re-calibrate the detector if needed and to secure energy-resolved data in case an event did not trigger the high-resolution recording. Thanks to that survey mode, the quantity of data goes from ~ 4 MB/hr to ~ 70 kB/hr (without events). Both survey and event modes are illustrated by a scheme in Figure 5.6.

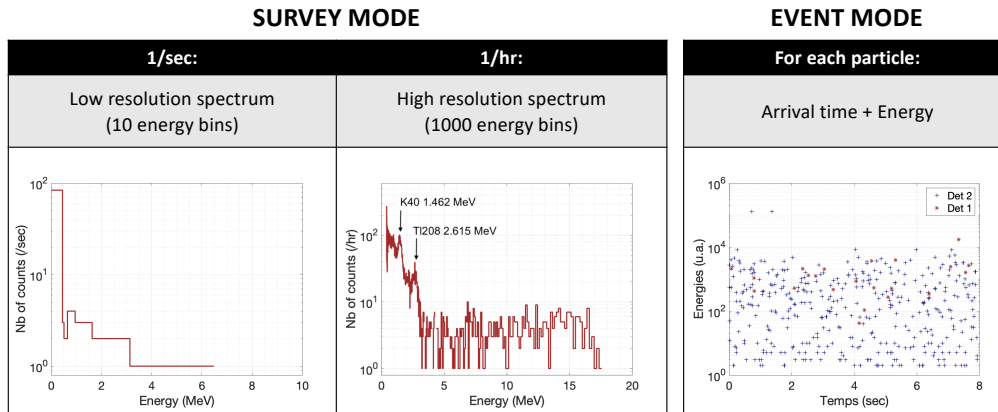


Figure 5.6: Illustration of the two working modes implemented, mainly to fly with balloons using satellite communication link. In the event mode, the detector type is indicated: plastic (detector 1) and BGO (detector 2).

Triggering processes

In order to be able to save the produced high-resolution data in case of an event detection, two different thresholds have been developed to detect independently TGFs and gamma ray glows using only the BGO scintillator channel. Both triggers are based on a monitoring of the background radiation and Poisson statistics in real time. We assume that the number of particles detected in the scintillators follows

5.2. Instrument Overview

a Poisson distribution law. In order to limit the number of false positive detected by the system, we use a criterion, which fixes the threshold for each type of event. Despite the fact that the radiation background does not effectively follow a Poisson distribution law, this method has shown good results during test flights, limiting the number of false positive, and it is worth mentioning that the threshold is also adjustable in flight. Assuming a Poisson distribution of counts, the probability to have a number of counts k over a time bin of duration τ is:

$$P(X = k) = e^{-\lambda} \frac{\lambda^k}{k!} \quad (5.2)$$

where $\lambda = R\tau$ is the mean number of particles detected over a duration τ , R is the number of particles detected per second. The probability to obtain more than k counts from the background over a time τ is then:

$$P(X \geq k) = \sum_{n \geq k} e^{-\lambda} \frac{\lambda^n}{n!} = 1 - \sum_{n < k} e^{-\lambda} \frac{\lambda^n}{n!} \quad (5.3)$$

The high-energy background can cause any numbers of counts over a given duration Δt with a likelihood quantified as above. These background-associated events are referred to as false positive events. The duration between two false positives is then:

$$\Delta t = \frac{\tau}{P} \quad (5.4)$$

As super-pressurized balloon flights last for a few months, we assume that it is acceptable to have one false positive per month, therefore we choose $\Delta t = 1$ month. The thresholds then only depend on the number of counts from the background radiation R .

Concerning TGFs, the typical time duration is $\sim 100 \mu\text{s}$ (e.g., [Fishman et al., 2011]) therefore we use $\tau = 100 \mu\text{s}$. Figure 5.7(a) shows Δt as a function of the threshold k and the background radiation R with $\tau = 100 \mu\text{s}$. One can see that Δt does not vary significantly as a function of the background radiation, and therefore,

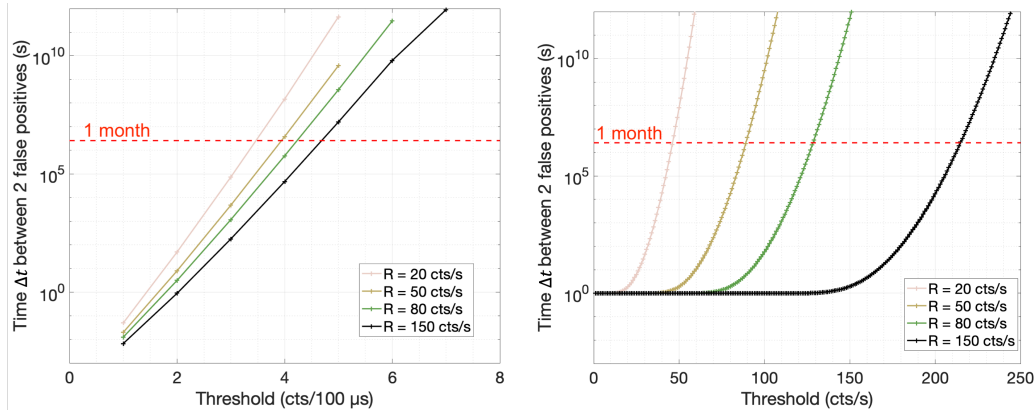


Figure 5.7: Duration between two false positives Δt as a function of the threshold k and the radiation background R for (a) TGFs ($\tau = 100 \mu\text{s}$) and (b) gamma ray glows ($\tau = 1 \text{ s}$). The red dashed line corresponds to 1 month.

given the observed background in the lower stratosphere (see Figure 5.12) we fixed the threshold at 5 counts/100 μs .

Concerning gamma ray glows, their time duration can presumably vary from seconds to tens of minutes. Thus, to be able to detect even the shortest glows we use $\tau = 1 \text{ s}$. Figure 5.7(b) shows Δt as a function of the threshold k and the background radiation R with $\tau = 1 \text{ s}$. Δt varies significantly as a function of the background radiation level, and therefore we developed a system to monitor the background radiation and fix the threshold with it, in real time, so as to always keep $\Delta t = 1 \text{ month}$. For instance, if the background radiation level measured is 80 cts/s, the gamma ray glow threshold will be fixed to 128 cts/s.

When one or the other of the thresholds has been overtaken, the on-board software will keep and send the high resolution data to the ground through satellite link, corresponding to the counts that have overtaken the threshold as well as some time before and after trigger (typically a few minutes, but this is adjustable from the ground). This is illustrated in Figure 5.8 with simulated data. Note that the system triggers high resolution recording as long as the threshold is exceeded. For typical background analysis durations considered (a few hours), glows lasting for more than this time scale will end up switching the trigger off as these glows would eventually be identified as the new background. In any case, such long-duration

5.2. Instrument Overview

glows are not expected and the corresponding amount of data would be too high for transfer. However, we also emphasize that the survey mode is always running in parallel and would continue providing data.

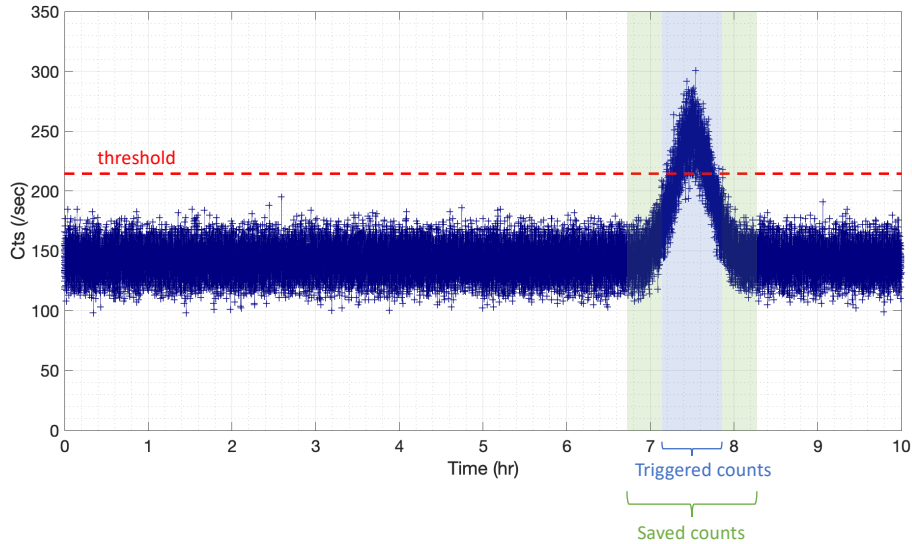


Figure 5.8: Illustration of a triggered gamma ray glow (simulated data). The blue shaded part corresponds to triggered counts. The green shaded part corresponds to the counts that are recorded and sent to the ground. The duration of the green part can be modified with a telecommand during the flight.

Strategy on telecommands

In order to follow at best the detector behavior, each telemetry packet provide house keeping data, such as temperatures, voltages and memory usage for instance, in addition to the gondola's house keeping that provides information such as temperatures of inside and outside the gondola and GPS positions. To control the behavior of the detector, a telecommand (TC) strategy have been developed. In fact, when a balloon flight uses a satellite communication link, it is usually possible to send TCs from the ground to the instrument. Trying to anticipate the possible problems that could occur during such a flight, we implemented several instructions to be run from the ground. The effect of these TCs are the following:

- Download high resolution data, even when no events have been triggered, that

Chapter 5. Gamma ray Spectrometer: Development & First Results

is available for some hours after the measure (~ 3 hours), before being deleted

- Modify some parameters used by the on-board software, such as configuration parameters of sensors (temperature function adjusting SiPM gains, scintillator pulse threshold, PSD parameters, etc.) or the criteria for the calculation of the triggering high-resolution recording thresholds
- Delete all the data acquired on the data logger, which would be useful for instance when a problem occurred and when the instrument needs a fresh start
- Send programmable bash commands to the data logger to open a large amount of possibilities, for instance changing precise parts of the on-board software

5.3 First Measurements

In this section, we present the preliminary results obtained with the developed gamma ray spectrometer. Measurements acquired during test flights on-board balloon in fair weather are presented, after the presentation of radioactive source measurements. An instrumental effect encountered during the balloon flights and later reproduced in the laboratory is presented with the solution found to avoid related issues.

5.3.1 Measurements of Radioactive Sources

The gamma ray spectrometer has been tested and calibrated using radioactive sources. Different radioactive sources were available: ^{137}Cs , ^{22}Na , ^{60}Co , ^{88}Y , ^{252}Cf , and ^{152}Eu . The calibrated spectra acquired with these sources are shown in Figure 5.9. All the expected gamma ray lines (black dashed lines) in the energy range detectable by the spectrometer are observed. Measurements of ^{22}Na , ^{60}Co , and ^{88}Y have been made very close to the source (< 1 cm). This particular configuration explains the “additional” lines observed in these spectra for higher energies. Indeed,

when the source is close to the detector, it increases the probability to detect two gamma photons in the same time range (here $1 \mu\text{s}$). In this case, the energy measured will correspond to the sum of the energy of both particles. This phenomena is called *coincidence summing*, creating *sum peaks*, and is also referred to as *pile-up*. It explains the ~ 2.4 MeV peak for ^{22}Na , the ~ 2.5 MeV large peak (containing probably 3 different sum peaks) for ^{60}Co , and the ~ 3.6 MeV peak for ^{88}Y . The ^{252}Cf spectrum does not show any visible gamma ray lines, indeed it is mainly used as a neutron source.

The resolution of the spectrometer being only $\sim 20\%$, it is not possible to distinguish the two lines of ^{60}Co at 1.1 MeV and 1.3 MeV (same for the sum peaks). ^{22}Na , with the line generated at 511 keV, confirmed that we would be able to detect this energies in case of the measure of a TGF afterglow for instance, as reported by [Enoto et al. \[2017\]](#).

5.3.2 Gamma ray Measurement Features

Following several test flights, we have noted different behavioral characteristics of the gamma ray spectrometer that we developed.

Temperature dependency

First, we found out that the spectrometer's gain depends on the temperature. This is a usual characteristic for such detectors. This characteristic has been measured as an extent of the spectrum within high energies at low temperatures, due to the better efficiency of the scintillator/SiPM couple at low temperatures for instance during balloon flights. This effect was so intense that some pulses were saturating, and were populating and polluting lowest energy bins. In fact, the integral of a saturated pulse, that is to say whose top has been cut, is equal to the integral of non saturated pulses of a lower energy. We have thus implemented a saturation bin which contains the number of saturated pulses to prevent this refolding spectrum.

To correct for the energy spectrum shift as a function of temperature, we imple-

Chapter 5. Gamma ray Spectrometer: Development & First Results

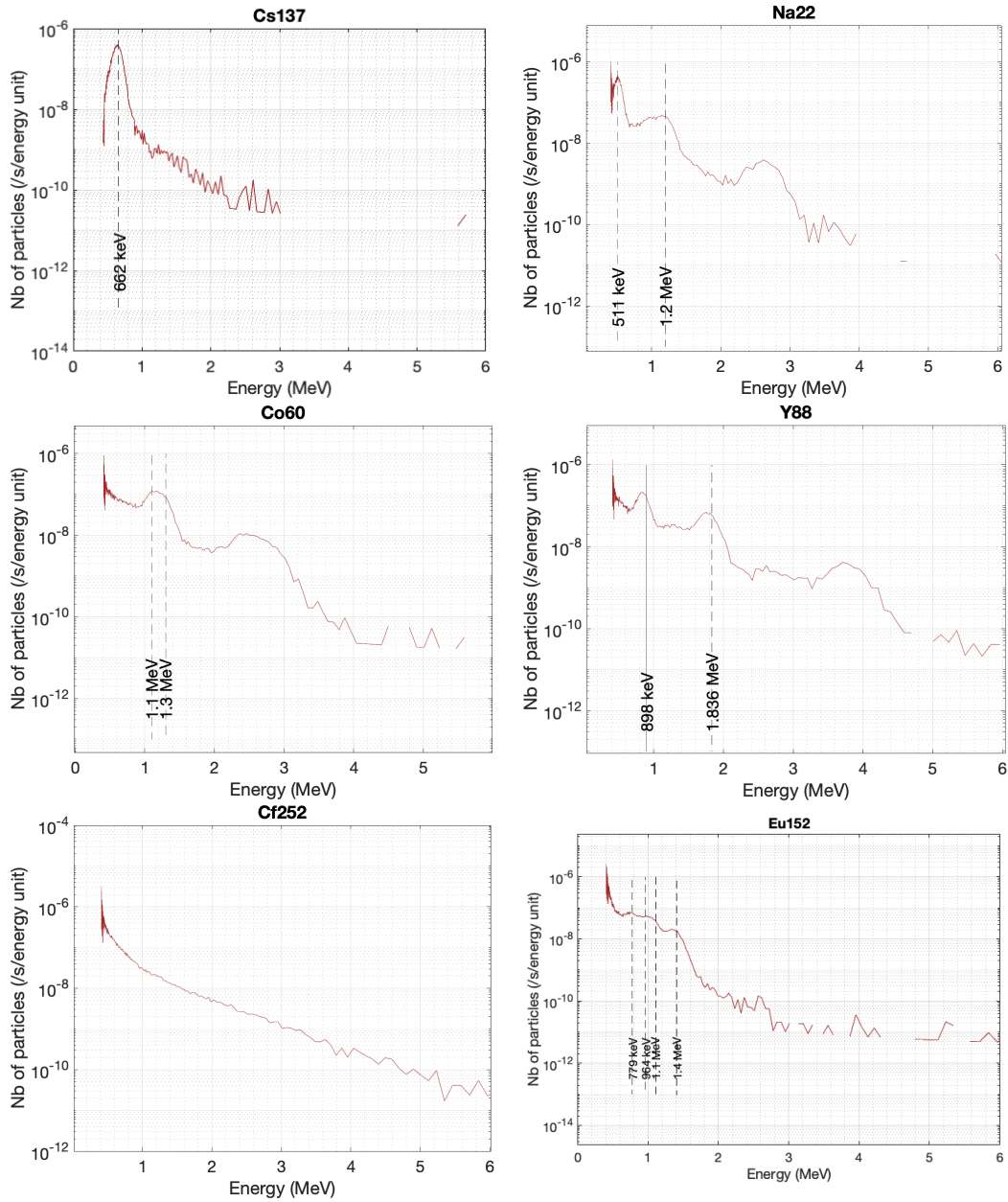


Figure 5.9: Energy spectra acquired with different radioactive sources. The expected gamma ray lines are shown by black dashed lines. An explanation concerning the “additional” lines than those specified is given in the text.

5.3. First Measurements

mented a temperature correction function for the SiPM gains. This is driven by a linear function to keep the energy spectrum constant as a function of the temperature. This linear function is sufficient to keep constant the energy spectrum for temperatures between -20°C and $+40^{\circ}\text{C}$ (see Figure 5.10), corresponding to temperatures that could be reached during balloon flights. The difference of the highest energy reported depending on the temperature is still not completely understood, but we speculate that the noise should be less important at low temperatures, allowing the possibility to detect higher energies, without saturating the ADC.

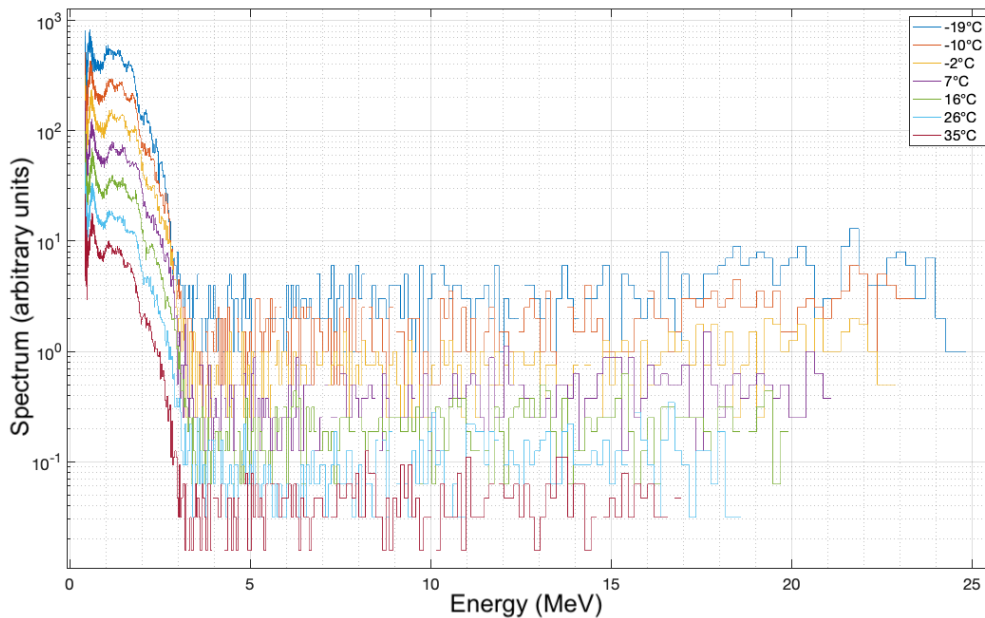


Figure 5.10: Energy spectra as a function of the temperature, with the use of the temperature correction function for the SiPM gains.

Count rate dependency

Another feature that was noticed during the testing of XStorm is the underestimation of the count energies under high count rates. In fact, for count rates greater than ~ 100 kHz, the energy is increasingly underestimated with the increase of the count rate, as shown in Figure 5.11. For instance, at 500 kHz, the energy measured corresponds to $\sim 70\%$ of the real energy. At 1 MHz, the energy measured

Chapter 5. Gamma ray Spectrometer: Development & First Results

corresponds to 50% of the real energy. This phenomenon is produced by the front-end electronics, composed of analog high-pass filters that cancel out the continuous component of the signal. At high-frequency rates, this continuous component is not efficiently filtered, and a bias is introduced in the energy calculation. Knowing the filter response, it should be possible to estimate the impact of this effect for measurements with count rates greater than 100 kHz.

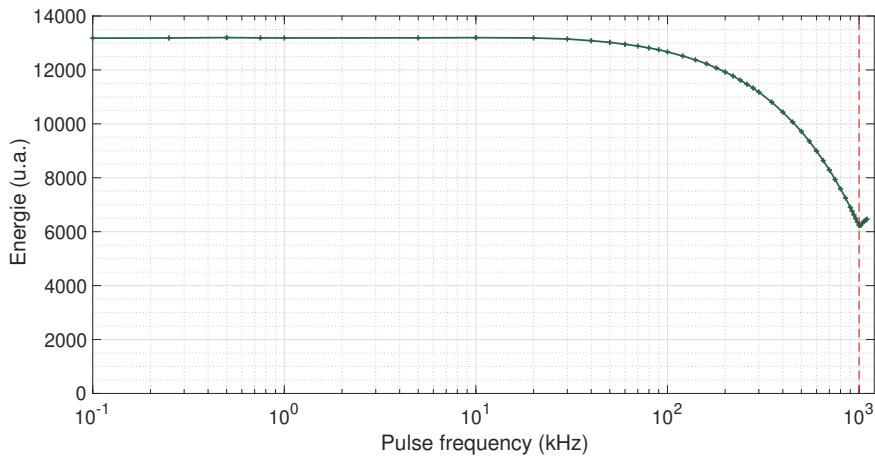


Figure 5.11: Measured energy of a pulse as a function of the count frequency. Pulses used are identical and generated by a pulse generator. The energy is attenuated from count frequency of ~ 100 kHz.

5.3.3 Lightweight Balloon Measurements in Fair Weather

Several balloon flights have been made in fair weather to validate the spectrometer's behavior. This balloon type (launch shown in Figure 5.13) can carry up to 2 kg of payload for a flight that last about 2-3 hours going up to ~ 30 km altitude, burst and going down below a parachute. The altitude monitoring of a flight is presented in Figure 5.12 upper graph. The payload is usually recovered at the end of the flight.

We present the number of particle detected by XStorm as a function of time in Figure 5.12 lower graph. Both BGO and plastic scintillator channels are represented, with a discrimination between gamma rays and neutrons on the plastic scintillator channel. The number of neutrons is multiplied by 100 to make the interpretation of

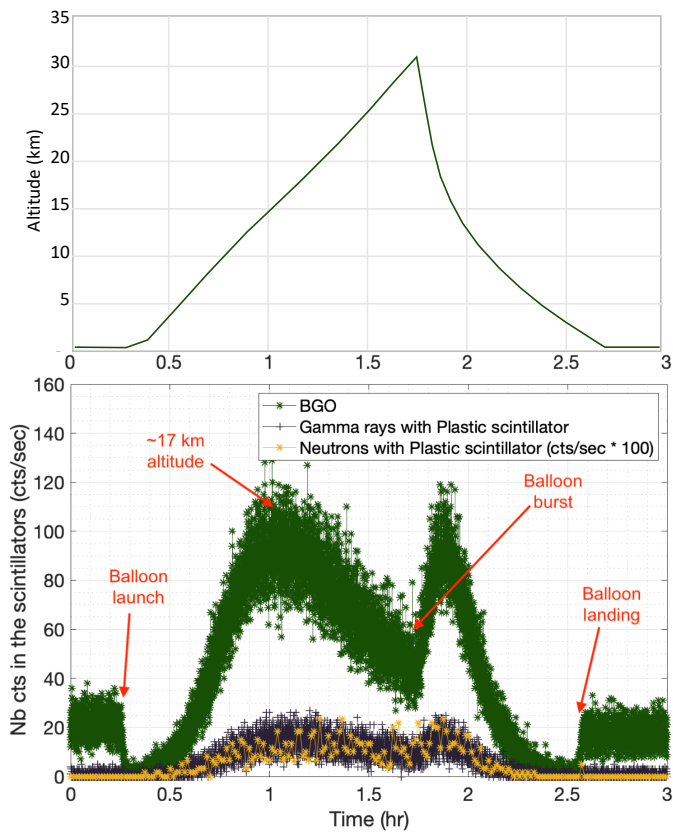


Figure 5.12: Number of particles detected by XStorm as a function of time during a lightweight balloon in fair weather. The balloon has been launched on the 7th October, 2021 at Aire-sur-l'Adour (France).



Figure 5.13: XStorm lightweight balloon launch in fair weather.

Chapter 5. Gamma ray Spectrometer: Development & First Results

the figure easier. The background at ground level before launch and after landing is due to natural radioactivity from soil. Then, the rate of detected particles is dependent on the altitude, with a maximum rate around 17 km which is called Regener-Pfotzer maximum [Regener and Pfotzer, 1934]. This maximum depends on the latitude. The balloon bursted at 33 km, and went back down to the ground quicker than during the ascent, under a parachute. The number of neutrons has been determined using the PSD method. Almost no neutrons have been detected on the ground, that is consistent with the proportion of neutrons (> 1 MeV) at ground level estimated by EXPACS [Sato, 2015] to be lower than 10^{-2} neutrons/s/cm² (in Toulouse, France, at < 300 m of altitude), and the fact that natural radioactivity is not expected to produce a significant neutron count rate. Neutrons are estimated by EXPACS to represent $\sim 20\%$ of the particles detected at 17 km of altitude, with ~ 2 neutrons/cm²/s.

The model EXPACS has also been used to compare the number of gamma rays detected with the number of particles in the atmosphere as a function of the altitude of the detector. We show the number of counts (/s/cm²) > 1 MeV detected by XStorm as a function of the altitude in Figure 5.14. We plotted the estimation made by EXPACS, taking different types of particle into account (photons, electrons, positrons, and protons) that are expected to participate to the count rate. The measurements with XStorm corresponds to $\sim 70\%$ of the count rate estimated with EXPACS, which is consistent with the expected efficiency of the instrument. In fact, the efficiency is expected to be $\sim 70\%$ for 1"-thick BGO scintillator crystals at 1 MeV for gamma rays [Saint-Gobain, 2021] (accounting for 78% of the particles at 17 km according to EXPACS).

5.3.4 Instrumental Effects Caused by Very Energetic Particles

During balloon flight tests in fair weather, numerous events (~ 500 per flight) with hundreds of counts occurring within hundreds of microseconds have been recorded at high altitude. One of these events is shown in Figure 5.15. The typical count

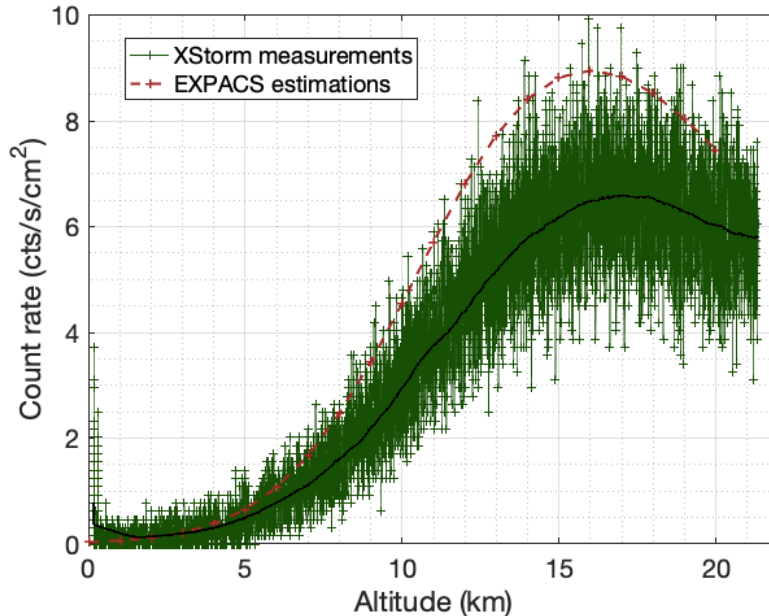


Figure 5.14: Number of counts ($/s/cm^2$) with energy >1 MeV detected by XStorm as a function of altitude (green). The black line corresponds to a moving average calculated over a 15-min range. The red dashed line represents the count rate estimations made with EXPACS, taking into account gamma rays, electrons, positrons and protons (>1 MeV).

sequence is always the same, one saturated count followed by 50-70 μs without signal during which time the detector is blind, and afterward approximately one hundred counts within 30-50 μs . The shape followed by count energies illustrated in Figure 5.15 is indicative of a strong instrumental effect as we cannot see a physical reason that would explain particles with increasing energies first and then decreasing as precisely as it is. These events have been recorded mostly at high altitude, only few have been recorded on the ground, less than 5 on several weeks of measurements. On the other hand, the number of these events detected during a balloon flight is very high: 474 events over a 2.5 hour flight, that corresponds to 1 every 20 seconds.

Exploring how these events can be produced in the spectrometer, we found that we could reproduce those events using electric pulses with a very high amplitude and duration as an input signal instead of SiPM output signal. We realized that the electric potential before the Analog-to-digital Converter (ADC) was going in

Chapter 5. Gamma ray Spectrometer: Development & First Results

the negative part during tens of microseconds, and coming back as a bounce to a positive signal lasting also tens of microseconds. This last positive part corresponds to the counts detected around 90 μs in Figure 5.15.

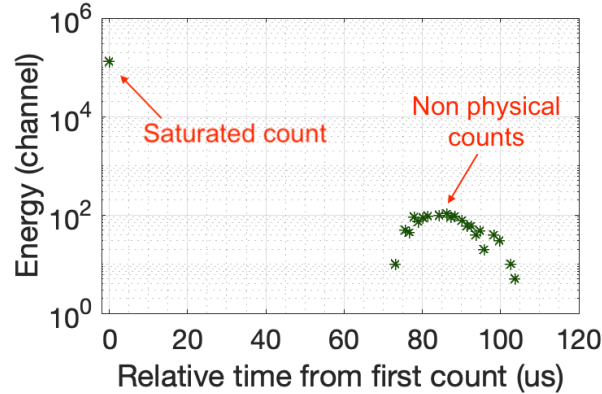


Figure 5.15: Instrumental effect detected during a balloon flight with XStorm.

This instrumental effect has the particularity to validate the criterion chosen to detect TGFs. In fact, the TGF detection criterion has been defined in Section 5.2.4 as “more than 5 counts in 100 μs ”. Therefore, our event triggering protocol leads these instrumental effects to be detected as TGFs every ~ 20 s, associated with a large amount of data saved and an overuse of the satellite communication link during a balloon flight. For this reason we had to find a way to discriminate TGFs from these instrumental effects.

Despite the fact that it seems visually easy to do this discrimination, the diversity of the parameters such as the time between the saturated count and the following count group, the number of counts in the following count group, the energies of the counts, etc., leads to the difficulty to find specific criteria to identify them. However, we found out that, using the right separation ratio between the two calculated integrals, we could use a method of PSD on the BGO scintillator channel, since the function was not used up to now. This method has been found to be optimal for a ratio of 60% for I_1 .

Figure 5.16 shows the representation of the PSD on the BGO scintillator channel

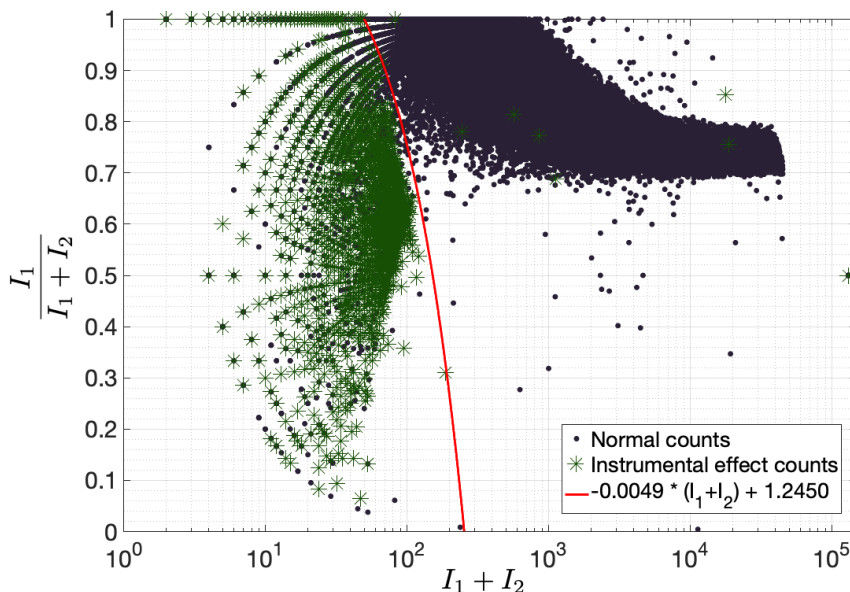


Figure 5.16: Representation of the PSD on the BGO scintillator channel during a balloon flight. Black points represent “normal” counts. Green stars represent the counts generated by instrumental effects. Inequality 5.5, represented in red, is defined as the limit between “normal” and “instrumental” counts.

during a balloon flight. We can clearly identify two groups of counts, according to their type. We thus assume that instrumental effect counts satisfy the following inequality:

$$\frac{I_1}{I_1 + I_2} < -0.0049 \times (I_1 + I_2) + 1.2450 \quad (5.5)$$

where I_1 and I_2 are the two integrals defined in Figure 5.3 with a separation at $0.6 \mu\text{s}$.

This criterion is used as follows. The event triggering protocol select all counts that satisfy “more than 5 counts in $100 \mu\text{s}$ ”. All the counts belonging to this group are classified as “normal” or “instrumental” counts with the inequality 5.5. If more than 90% of the counts are estimated to be instrumental effect counts, we consider that the counts do not come from a TGF detection. This method has been tested in flight, and has shown a rate of 100% of rejection of the spurious instrumental effects.

5.4 Conclusions

In this chapter, we have presented the newly developed lightweight gamma ray spectrometer, its objective-driven performance, its characteristics, and the first results obtained during testing. It has been developed to detect and study gamma ray glows and TGFs in the vicinity of thunderstorms and be flown on board balloon flights. Several specifications have been defined to fit the constraints imposed by balloon flights, such as a light weight, low cost to mitigate the risk of no recovery, and a low power consumption. The energy range and time performances have been defined to detect gamma ray glows and TGFs, limiting the effects related to energy saturation processes, dead-time, and pile-up. Both the measurements campaigns planned presented in the first section are very promising, and should provide new information on these events and help achieve the following objectives:

- Observe gamma ray glows and TGFs in close proximity over long time scales
- Explore source geometries and time dynamics of gamma ray glows
- Investigate runaway electron acceleration processes
- Study the link between gamma ray glows and cosmic rays
- Study the mutual impact between the thunderstorm electrical system and gamma ray glows
- Quantify radiation doses in thunderstorms (see also Chapter 3)
- Detect radionuclide and neutron signatures of TGFs
- Understand the relation between TGFs and gamma ray glows

Radiation background and radioactive sources have been used to calibrate the detector. Several balloon flight in fair weather have been performed and measured the background radiation level mainly due to cosmic rays, in agreement with estimations from the cosmic ray flux model EXPACS [Sato, 2015]. An innovative method

5.4. Conclusions

is used to detect and identify neutrons with a plastic scintillator, namely the Pulse Shape Discrimination (PSD) method. This method has been demonstrated using a neutron source and in the radiation background at high altitude, showing $\sim 1\%$ of neutrons among the particles detected.

An on-board software has been developed to enable the event detection in real time, based on Poisson statistics, and thus limit the amount of data saved when satellite communication link is used.

Spurious events presented in Section 5.3.4 have been identified, explained, and a rejection protocol has been implemented in the on-board software so as not to mistake these counts for TGFs.

Predictions on XStorm measurements

Key Points

- Estimation of the detectability of gamma ray glows and TGFs as a function of the altitude and applied to Stratéole-2 campaign
- Gamma ray glows with sources above 14 km altitude are detectable from 20 km-altitude balloons
- We estimate that there is approximately a one-in-two chance for a single instrument on board a Stratéole-2 flight to detect a TGF

Gamma ray glows are central to the scientific objectives of XStorm as they are more frequent and easier to detect at balloon altitudes than TGFs. TGF detection is a secondary objective, but such a measurement would bring critical new information. In this chapter, we present calculations and simulations to determine how and where a gamma ray glow can be detected using XStorm on balloon campaigns such as Stratéole-2 and OREO, and with ground-based measurements. We also present calculations on the probability to detect a TGF during a Stratéole-2 balloon flight.

6.1 Photon propagation for gamma ray glows

In order to have an idea of what can be detected as a function of the altitude, we simulate the propagation of photons, from source altitudes between 1 and 20 km. The photon propagation is simulated using the Monte Carlo code presented in Sec-

tion 2.2.3, based on [Østgaard et al., 2008] assuming a standard RREA spectrum with a 7.3 MeV cut off (e.g., [Dwyer et al., 2012]). Two different configurations will be used, one with initial photon velocities directed upward, and the other one with initial photon velocities directed downward, to model charge structures in thunderstorms. Convolving the impulse response of a point source to simulate expanded sources in time and space, corresponding to gamma ray glows with a given initial photon flux, we verified that the ratio of the final photon flux over the initial photon flux for a gamma ray glow, is equal to the ratio of the final number of photons over the initial number of photons for the punctual source. Therefore, to evaluate the flux attenuation as a function of altitude, we simulate punctual sources.

The proportion of photons that reach altitudes between 0 and 30 km, with an initial source set between 1 and 20 km of altitude and initial photon velocities directed upward, is shown in Figure 6.1. The same results but with initial photon velocities directed downward, are shown in Figure 6.2. Photons are more attenuated with downward velocities as the atmosphere is thicker at lower altitudes. In those simulations, we do not take into account bremsstrahlung from positrons propagating back to the start of the avalanche. Positrons and gamma rays produced by their bremsstrahlung are part of the RREA process and therefore it is worth mentioning that this phenomenon would probably enhance the detectability in the reverse direction.

6.2 Detectability of gamma ray glows

In order to know in which conditions a gamma ray glow is detectable at 20 km of altitude, for the next Stratéole-2 campaign for instance, we estimate the photon flux at 20 km of altitude for a strong gamma ray glow reported in the literature. We will use the case reported by Kelley et al. [2015], who detected a glow-like event during the ADELE project and reported the measurement of the electron flux. They indeed estimated that the detector was in the electron source at the time of the event,

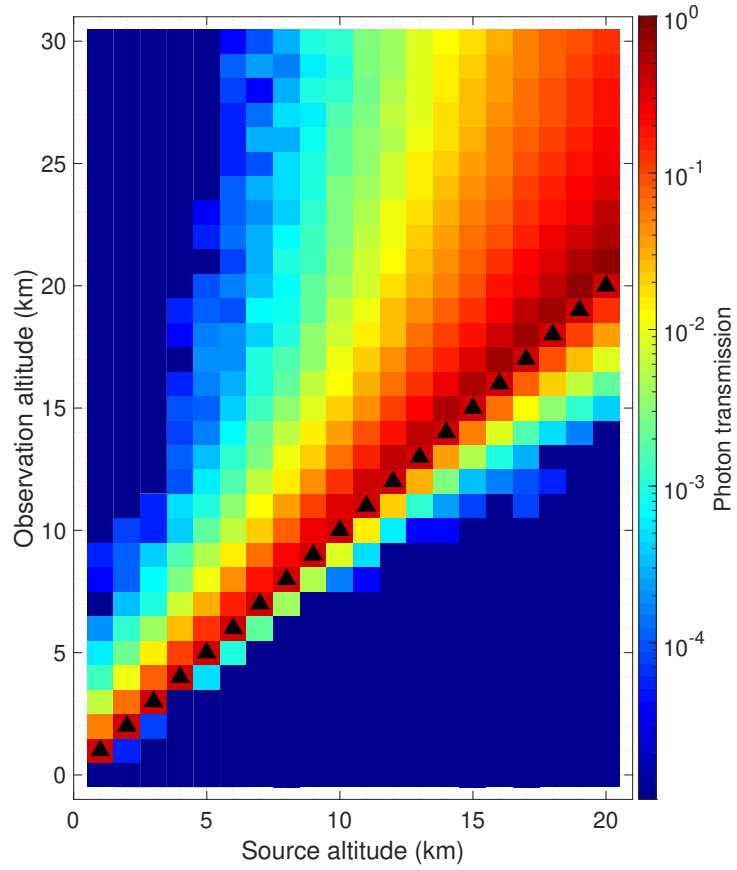


Figure 6.1: Proportion of photons that reach a given altitude (or ratios of photon fluxes observed at various altitudes to fluxes at the source in the case of an infinite source plane. The source is set at different altitudes between 1 and 20 km, with initial photon velocities directed upward (black triangles).

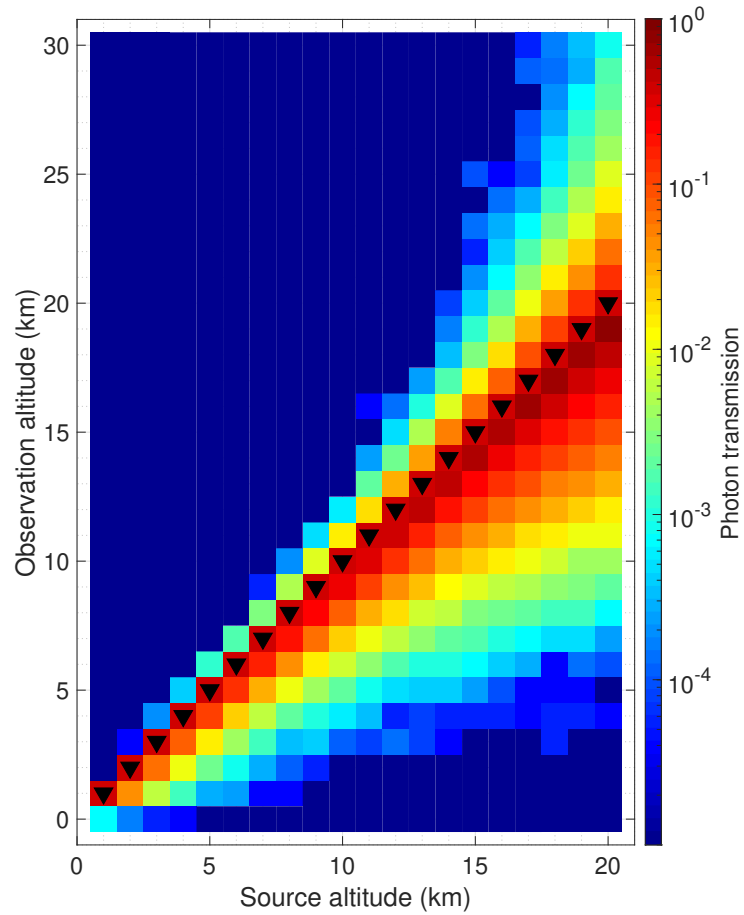


Figure 6.2: Proportion of photons that reach a given altitude (or ratios of photon fluxes observed at various altitudes to fluxes at the source in the case of an infinite source plane. The source is set at different altitudes between 1 and 20 km, with initial photon velocities directed downward (black triangles).

6.2. Detectability of gamma ray glows

with a measured flux of 1,100 electrons/cm²/s at 14.1 km of altitude [Kelley et al., 2015]. This detection is believed to be done at the end of a downward RREA. We developed a toy model simulating the production of RREA in a 5 km side region with an exponential distribution that ends with a flux of $f_e = 1,100$ electrons/cm²/s at 14.1 km. The electron density at the end of the avalanche at 14.1 km is:

$$n_e(14.1 \text{ km}) = \frac{f_e(14.1 \text{ km})}{v_e} = \frac{1,100/\text{cm}^2/\text{s}}{0.89c} = 0.0412 \text{ electron/m}^3 \quad (6.1)$$

where v_e is the mean electron velocity in a RREA [Coleman and Dwyer, 2006]. We assume that the runaway electron density as a function of the altitude z is:

$$n_e(z) = n_0 \exp\left(\frac{z}{\lambda}\right) \quad (6.2)$$

where n_0 is the initial runaway electron density and λ can be calculated from equation 1.4 and is dependent on the electric field amplitude. We use an electric field amplitude $E = 4 \text{ kV cm}^{-1}$, also used in simulations by Kelley et al. [2015], which gives $\lambda = 340 \text{ m}$ at 14.1 km. The density profile $n_e(z)$ is then fixed by the condition described in equation 6.1. According to our simulation, the majority of the avalanche takes place within 3 km of altitude. This is also assessable using the avalanche multiplication factor estimated in Kelley et al. [2015] to be $\sim 4,500$. The number of avalanche lengths is then $\ln(4,500) \approx 8.4$, and thus the avalanche is $8.4 \times \lambda \approx 2.8 \text{ km}$ long.

In the simulation, the position of each starting electron and each new electron is randomly chosen following the exponential distribution of equation 6.2. We propagate electrons and photons assuming their velocities to be respectively $v_e = 0.89c$ and c and directed upward, and we use a time step of $0.1 \mu\text{s}$ which we calculate the new position of each particle. We fix the number of electrons in the simulation, and for each electron that reaches the limit altitude of 14.1 km, a new electron is injected following the exponential distribution of the positions. Then, we simulate

Chapter 6. Predictions on XStorm measurements

the production of photons by each electron using the mean bremsstrahlung photon production (with energy >1 MeV) frequency ν_γ over the standard RREA spectrum, given in equation 2.4, that is equal to $\sim 2.4 \cdot 10^5$ photon/electron/s. Photons are propagated without absorption (in the RREA and above). Figure 6.3 helps visualize the configuration of the simulated system. The position of electrons and photons, the distribution of the photon and electron fluxes in the simulation as a function of the altitude, and the flux at 14.1 km as a function of the time are represented. The photon flux at 14.1 km is then found to be ~ 340 photons/cm²/s.

We compare this result with Kelley et al. [2015] measurements, using the gamma ray and electron spectra provided in their Figure 2. Integrating the spectra for energies >1 MeV, we obtain the ratio between the electron flux and the photon flux to be ~ 4.7 . Thus, we obtain a photon flux of 235 photons/cm²/s. This result is consistent with our estimation, given that we used different physical parameters, in particular the cross-sections values to calculate ν_γ .

Such result can be easily obtained analytically. Indeed, the differential equation driving the density of photons at 14.1 km (end of the RREA) as a function of the electron density can be written as:

$$\frac{\partial n_\gamma}{\partial t} + \vec{\nabla} \cdot (n_\gamma \vec{c}) = n_e \nu_\gamma \quad (6.3)$$

where n_γ and n_e are the photon and electron densities, \vec{c} is the speed of light and ν_γ is given by equation 2.4, $n_e \nu_\gamma$ represents the quantity of bremsstrahlung photons produced by the electrons per unit time. In the stationary state, $\vec{\nabla} \cdot (n_\gamma \vec{c}) = n_e \nu_\gamma$. Therefore, in one dimension it gives:

$$c \partial_z n_\gamma = n_e \nu_\gamma \quad (6.4)$$

6.2. Detectability of gamma ray glows

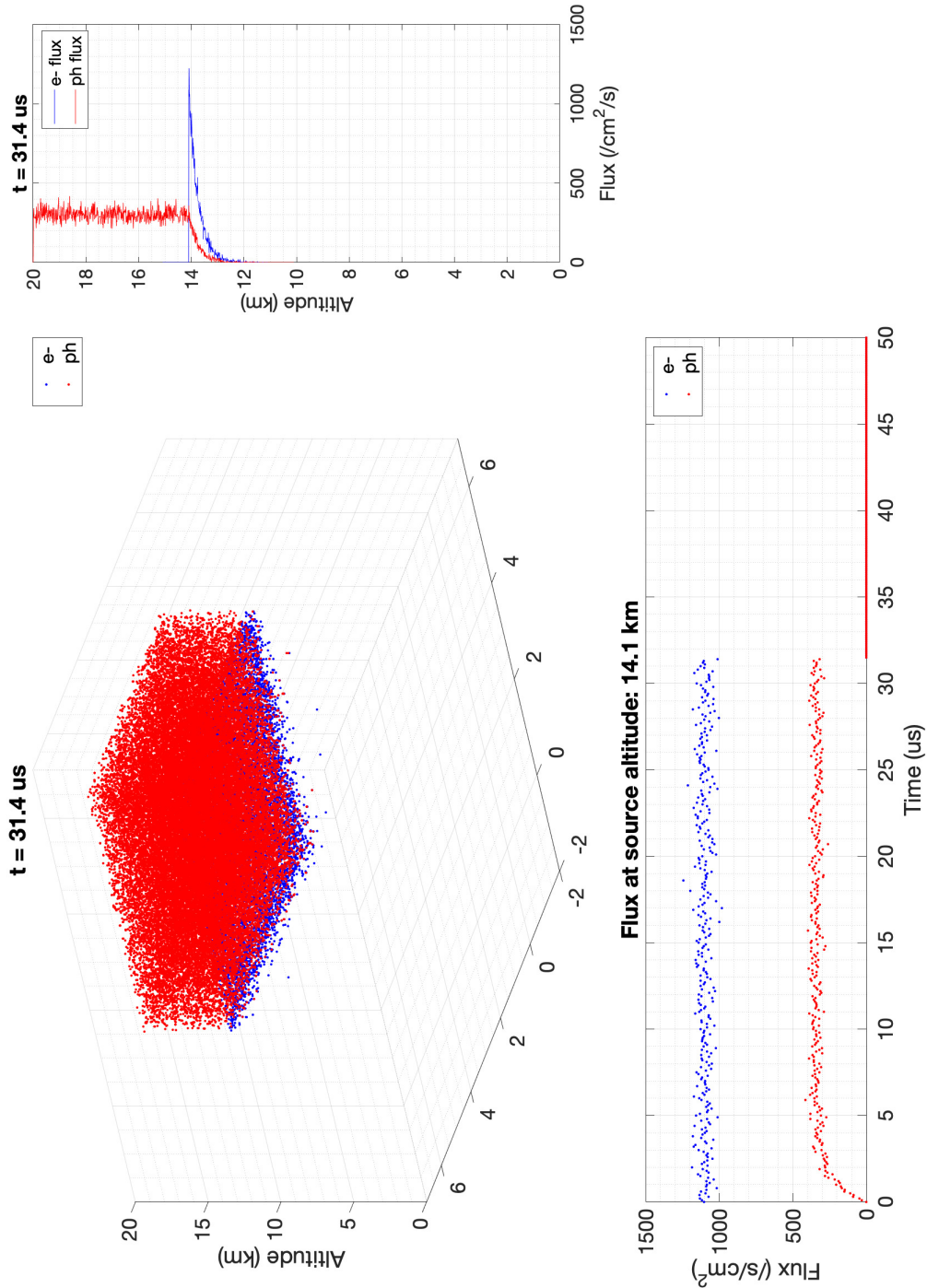


Figure 6.3: Simulation of a RREA with photon production in real time. The position of electrons and photons are plotted respectively in blue and red. The stationary photon flux at 14.1 km is reached within less than $5 \mu\text{s}$. In this simulation, the photons do not undergo collisions, hence photon flux observed above 14.1 km is constant.

Chapter 6. Predictions on XStorm measurements

Hence, using equation 6.2:

$$n_\gamma(z) - n_\gamma(z_0) = \frac{\nu_\gamma}{c} \int_{z_0}^z n_e(z) dz = \frac{\nu_\gamma [n_e(z) - n_e(z_0)] \lambda}{c} \quad (6.5)$$

$n_e(z_0)$ is negligible and $n_\gamma(z_0) = 0$. We then obtain:

$$n_\gamma(z) = \frac{\nu_\gamma n_e(z) \lambda}{c} \quad (6.6)$$

With ν_γ obtained from equation 2.4, $n_e(14.1 \text{ km})$ from equation 6.1, and $\lambda \approx 340 \text{ m}$ calculated above, we get $n_\gamma = 0.0153 \text{ photons/m}^3$, and therefore the photon flux at 14.1 km is:

$$f_\gamma(14.1 \text{ km}) = n_\gamma \times c = 334 \text{ photons/cm}^2/\text{s} \quad (6.7)$$

The model agrees well with the theoretical prediction.

The attenuation due to collisions can be taken into account in reducing the flux using the ratio determined in Section 6.1 for a source altitude of 14.1 km, as a function of the observation altitude. Using the flux deduced by [Kelley et al. \[2015\]](#) measurements, we estimate for which altitudes such a glow would have been detectable, depending on the source altitude, using upward and downward initial velocities for photons. In this purpose, we use the background radiation level as a function of the altitude between 0 and 30 km of altitude, determined by the combination of EXPACS estimations and balloon measurements with XStorm launched from Aire-sur-l'Adour (France). Our detector will fly at 20 km of altitude for the next scientific campaign of Stratéole-2. The detectability of gamma ray glows with the method presented in Section 5.2.4 depends on the detection surface area of the detector. In fact, the threshold calculated is not proportional to the background radiation level but depends on the occurrence frequency of false positive events. For instance, for a background of 4 cts/cm²/s, the threshold is fixed at 7 cts/cm²/s, and for a background of 8 cts/cm²/s, the threshold will be fixed at 12 cts/cm²/s. This is due to the fact that Poisson likelihood does not increase linearly with the number

6.3. Probability to detect a TGF

of counts for higher number of counts. Therefore, we determine the detectability of a glow using the geometric surface of XStorm that is a cube of 1" side, thus $S_{XStorm} = 6.45 \text{ cm}^2$.

The detectability for a glow with a source flux of 340 photons/cm²/s depending on the source altitude and the initial photon velocity direction is plotted in Figure 6.4. According to Figure 6.1, the flux at 20 km is equal to 7% of the flux at 14 km, and therefore would be equal to 24 photons/cm²/s. Such a glow would then be detectable, as the background radiation level at 20 km of altitude is ~ 8 photons/cm²/s (see Figure 5.14). For photons propagating downward, using Figure 6.2, we found that the flux at 20 km will be attenuated by 99.2% and will thus not be detectable by XStorm. More generally, XStorm on a Stratéole-2 balloon at 20 km will be able to detect upward gamma ray glows for sources between 14 and 20 km and downward gamma ray glows for sources between 18 and 20 km of altitude.

The fact that for a source altitude of 1 km, a gamma ray glow is not detectable from the ground is due to the natural radiation background of the ground estimated with XStorm measurements (note that EXPACS estimate only radiation level from cosmic rays).

It is worth mentioning that the reference glow chosen in those studies is a bright one reported by Kelley et al. [2015]. Much fainter glows such as the one reported by Østgaard et al. [2019a], with a signal to noise ratio of about 1.4, requires a longer triggering timescale than 1 s to be detected. The triggering timescale is a variable parameter on XStorm, and will be adjusted to optimize the detection of fainter glows for the next Stratéole-2 campaign.

6.3 Probability to detect a TGF

The detection of TGFs by balloon is believed to be less probable than gamma ray glows, because TGFs are less frequent and because balloon flights are very close to the altitude of TGF sources as compared to satellites. This proximity limits

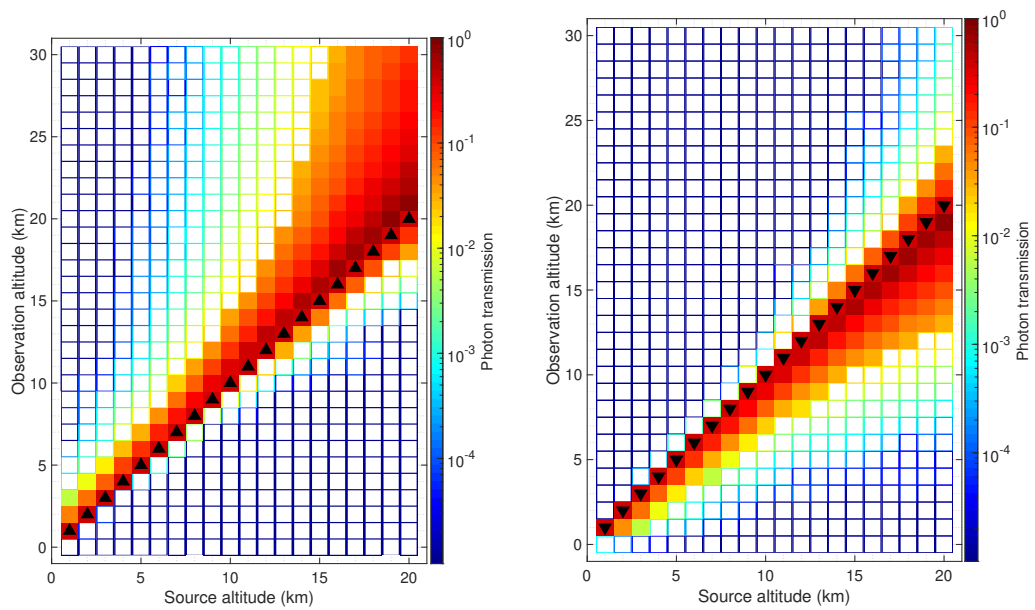


Figure 6.4: Same as Figures 6.1 and 6.2 with upward (left) and downward (right) initial velocities for photons. Only the XStorm detectable glow configurations are filled, using the threshold calculation method presented in Section 5.2.4 and the background radiation level determined by EXPACS and fair weather balloon flights at Aire-sur-l'Adour (France). The glow used as a reference is the glow detected and described in [Kelley et al. \[2015\]](#).

6.4. Ground-based measurements

the field of view of the detector. Stratéole-2 campaign consists in balloons flying between 18 and 20 km of altitude for long duration. We hence expect a small but non-zero probability to detect such an event. Therefore, we want to estimate the probability of this to happen. We assume an upward TGF with an opening angle of 45° , photon directions isotropically distributed in the beam, a typical TGF source altitude of 12 km, and an observation performed at 20 km. Monte Carlo simulations of photon fluxes show that at least 5 photons of the assumed TGF would be detected for distances smaller than ~ 20 km from the source, for XStorm detection area of ~ 6 cm². We therefore assume that a TGFs would be detectable within a 20 km-radius around the source. We calculate a map of TGF densities in units of /s/20 km-radius to take into account the field of view of XStorm, similarly to what was done in Section 2.3.1. Using the trajectories of the 8 balloon flights performed in the Stratéole-2 preliminary campaign in 2019 (with a mean of 85 days per flight), we calculate the probabilities to find one balloon in a TGF beam, applying the same method as described in Section 2.3.3. We thus estimate that $\sim 1/2.3$ Stratéole-2 balloon flights will be able to detect a TGF. The next scientific campaign is planned in 2024, for which we have to deliver 4 detectors to be flown on super-pressurized balloons, thus we estimate the expected number of TGFs detected during the next campaign to be ~ 2 .

6.4 Ground-based measurements

Ground-based measurements have the advantage to be continuously running during long periods of time and to allow the use of bigger detectors. This improves the count statistics, the spectroscopic resolution and the detectability of weak glows. However, ground-based measurements have the disadvantage to have the thicker part of the atmosphere between the detector and the event, and a non-negligible higher background radiation level due to the natural terrestrial radioactivity. This natural radiation level is difficult to estimate as it depends on the ground type.

Chapter 6. Predictions on XStorm measurements

Thus, we use the background radiation measured at Aire-sur-l'Adour (France) as a reference, in addition to the radiation background due to cosmic rays. The size of the scintillators are assumed to be 3" side. We determine with the same method used in Section 6.2 the detectability of gamma ray glows similar to the one reported in Kelley et al. [2015].

Results are shown in Figure 6.5. Ground-based detections are found to be very similar to in-flight cases presented in Figure 6.4. Only some configurations do not allow ground-based detections as compared to in-flight detections. This is the case for a 3 km altitude source with an observation at 1 km of altitude, and for a 7 km altitude source with an observation at 4 km of altitude.

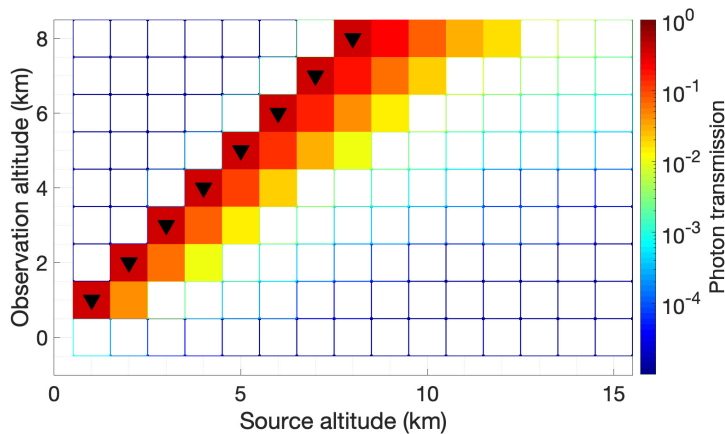


Figure 6.5: Detectability of [Kelley et al., 2015]-like gamma ray glows for ground-based detections, depending on the source altitude and the observation site altitude.

6.5 Conclusions

In this chapter, we have used the Monte-Carlo model presented in Section 2.2.3 to determine the configurations for which XStorm would be able to detect a gamma ray glow. Simulating the photon propagation in the atmosphere, we used initial photon velocities directed upward and downward to model different charge structures of thunderstorms. We used altitude sources between 1 and 20 km, and observation

altitudes between 0 and 30 km to cover the altitude range that can be reached by balloons. We determine for each configuration which proportion of the photon flux reaches the observation altitude.

The electron flux measurement presented in [Kelley et al. \[2015\]](#) is then used to simulate the photon flux generated by RREAs with such an electron flux. We conclude that the maximum photon flux at the source should have been ~ 340 photons/cm²/s.

Taking into account the event detection method considering the background radiation level as presented in Section 5.2.4, we determine the parameters [source altitude ; observation altitude] for upward or downward photon fluxes that correspond to detection using XStorm. The same exercise is done for the adaptation of XStorm as a ground-based detector (using large scintillators), taking into account the natural radiation from the ground in addition to the radiation due to cosmic rays.

In addition to usual gamma ray glows studied in this chapter, the detection of high-altitude gamma ray glows such as those reported by [Østgaard et al. \[2019a\]](#) would bring new information on this new type of observations and help understand the link between gamma ray glows, TGFs, and charging processes that take place in thunderstorms.

General Conclusion

Key Points

- Although TGFs likely produce high doses in highly compact regions, the low probability for an aircraft to be in the TGF electron beam makes the additional risk of exposure due to TGFs is not significant
- The promising future observational results with the newly developed gamma ray spectrometer will help answer open questions in the high-energy atmospheric research field

Because high-energy events produced in thunderstorms such as TGFs and gamma ray glows overlap with commercial flight altitudes, the need for an assessment of the corresponding additional exposure has been raised. In fact, the first studies performed to estimate the radiation doses that could be generated by such events [Dwyer et al., 2010] led to a real concern among flight crew unions. In this manuscript, we presented studies quantifying potential damages and exposure probabilities, along with new instrumental developments and planned campaigns to improve theoretical estimates and further the understanding of thunderstorm-associated high-energy phenomena.

7.1 Summary

First, using numerical simulations, a precise estimation of the radiation doses delivered by TGFs has been presented in Chapter 3. Doses associated with runaway electrons have been estimated using two models used in the literature to explain

Chapter 7. General Conclusion

TGF production. Using both models, electron doses are estimated to be large, reaching almost ~ 1 Sv (dose value that implies acute radiation sickness), nevertheless in small areas of tens of meters large. Using a Monte Carlo method, we performed simulations of photon propagation in the atmosphere to simulate TGFs and estimated that the maximum photon dose delivered reaches only $90 \mu\text{Sv}$. The radiation doses associated with secondary electrons produced by photon collisions have also been estimated, being limited to $< 1 \mu\text{Sv}$. The worrying doses associated with TGFs are therefore associated with runaway electrons, which high doses spread only over 200-m radius regions in the considered models. To supplement these results, we then proposed to quantify the probability for an aircraft to find itself in the 200-m radius high dose region of a TGF.

We estimated this probability with a statistical study, using satellite and flight route data, in Chapter 4. We first used the Fermi-GBM satellite TGF data, acquired between 2012 and 2016, to calculate a TGF density map. We found this TGF density map to be consistent with previous estimation of the global number of TGFs per year (400,000) and reported measurement campaigns. Using both this density map and commercial flight routes, we were able to calculate the probability for an aircraft to be hit on each trajectory. Two different approaches were used concerning commercial flight routes. First, the 600 biggest airports in the world were used to simulate geodesic routes between airports. With this approach, the more exposed route were found to be between Atlanta (Georgia, USA) and Santiago (Chile) with one aircraft hit by a TGF once every ~ 250 years. Then, real flight route data for Air France airline between 2012 and 2016 were used. The calculated probabilities have shown that on the whole Air France fleet, ~ 390 years separate two Air France aircraft hit by a TGF. Note however that this evaluation is maximized as the evasive actions taken by pilots to avoid thunderstorms are not considered. Finally, in a more concrete approach, we looked for the smaller distance between an in-flight Air France aircraft and a Fermi-GBM detected TGF in 2.5 years. We found it to be 36 km. This distance is much larger than the high radiation dose radius determined

in the previous study (~ 200 m). The proximity distribution using real flight routes is however not sufficiently precise to perform an extrapolation down to 200 m.

To complete the study of the TGF associated risk, we developed a new gamma ray spectrometer, named XStorm, which aim is to detect TGFs and gamma ray glows in close proximity. The detector development has been performed entirely during this PhD program and is now ready to fly on the campaigns planned. First, the ability to date the arrival time of the particles within 100 ns precision UTC will allow to compare our data with other lightning-related data such as lightning sferics detection with ground networks (for instance GLD360). Then, photon energies between 400 keV and ~ 30 MeV are measurable and the detector allows to perform the discrimination between three types of particles using two different method. The electron/photon discrimination is doable statistically, knowing that, in contrast with electrons, photons are more efficiently detected in the BGO scintillator than in the plastic scintillator. The Pulse Shape Discrimination (PSD) method is used for the discrimination between photons and neutrons with the plastic scintillator channel. It has been tested successfully using a neutron source and in the radiation background at high altitude. We also developed and implemented a real time analyzer to detect TGFs and gamma ray glows on board the balloon gondolas and limit the quantity of data transferred.

Finally, we presented predictions on future measurements that can be expected with XStorm on board balloon campaigns. Using the reported electron flux measured by Kelley et al. [2015], we determined the different configurations (source altitude and detector altitude) for which XStorm would be able to detect a gamma ray glow. The next Stratéole-2 campaign that will fly at ~ 20 km altitude in 2024 is a unique vantage point to measure gamma ray glows and TGFs. We expect to be able to detect upward gamma ray glows produced between 14 and 20 km altitude. Concerning TGFs, we calculated the probability that a TGF occurs in the ~ 20 km radius field of view of XStorm during a Stratéole-2 balloon flight, and found that there is approximately a one-in-two chance for each single instrument to detect a

TGF.

7.2 Impact of the thesis

The results presented in this thesis bring needed information to flight crews about their actual in-flight exposure and the impact of these recently discovered events. We already discussed with pilot trade unions and Air France airline about the results presented in this thesis and their feedbacks were positives. Moreover, we performed new and original studies about physical aspects such as the comparison of runaway electron propagation using the two main TGF production models, and the development of a gamma ray spectrometer to detect these events in close proximity.

7.3 Perspectives

Finally, this thesis calls for following studies to be carried on. In particular, measurements in electrically active regions with the gamma ray spectrometer developed during the thesis is planned for the campaign presented. The future measurements will bring new information on TGFs and gamma ray glows, allowing to confirm or invalidate theoretical and statistical results presented in this thesis, to explore the source geometries and time dynamics of these events, study the relation between TGFs and gamma ray glows, their impact on the thunderstorm electrical system and the runaway electron acceleration processes producing these events.

Étude du risque associé aux TGF et aux gamma ray glows pour le personnel navigant

Résumé du Chapitre 1 : Introduction

Les orages sont des perturbations atmosphériques engendrées par des nuages de type cumulonimbus, s'étendant de quelques centaines de mètres du sol jusqu'à la tropopause. L'étude des éclairs permet de caractériser ces orages sur l'ensemble du globe terrestre. Les orages sont aussi à l'origine de la production d'évènements de haute énergie, appelés flashs gamma terrestres (TGF) et gamma ray glows. Découverts dans les années 90, ces évènements ne sont pas encore compris dans leur entièreté, et soulèvent encore de nombreuses questions comme leur distribution spatiale et temporelle sur le globe, le mécanisme d'initiation de ces évènements ou encore le risque associé à l'exposition de ces évènements des passagers de vols commerciaux, particulièrement adressé dans cette thèse.

Les TGF sont des bouffées de photons de haute énergie, appelés rayonnement gamma, durant $\sim 100 \mu\text{s}$. Les énergies des photons produits peuvent atteindre >40 MeV. Leur production a été montrée comme étant liée à la présence d'éclairs intra-nuages de polarité positive (+IC). Découverts et détectés principalement par satellites (e.g., CGRO, Fermi ou ASIM sur la station spatiale internationale), on estime d'après ces mesures la génération de 10^{18} photons à leur source. D'autres mesures sont réalisées au sol, concernant les TGF inversés, dont le faisceau de photons est

Résumé en Français

dirigé vers le bas, et quelques rares mesures ont été effectuées par avion, par exemple lors du projet [ADELE](#). On estime que $<1\%$ des éclairs intra-nuages produisent un [TGF](#), ce qui représente $\sim 400,000$ [TGF](#) par an sur le globe, détectables par satellite. Les gamma ray glows sont des augmentations du rayonnement de fond dans les orages. Ils ont des durées beaucoup plus longues que les [TGF](#), de quelques secondes à quelques dizaines de minutes. Beaucoup moins fluents, ils sont rapidement atténués par l'atmosphère et ne peuvent pas être détectés par satellite. Ils sont généralement détectés par des mesures au sol, dans des endroits où la couche d'atmosphère entre l'orage et le détecteur est plus fine, c'est-à-dire à haute altitude, en montagne, ou au Japon où un climat spécial produit des orages à quelques dizaines de mètres du sol seulement. Il a été estimé conservativement que plus de 8% des orages produisent des glows.

Malgré le fait que ces événements aient des formes et des durées différentes, ils sont généralement étudiés ensemble car produits par les mêmes mécanismes physiques. En effet, leur rayonnement gamma est produit par rayonnement bremsstrahlung d'électrons relativistes. Ces électrons sont accélérés à des vitesses relativistes lorsqu'ils sont soumis à un champ d'amplitude supérieur à la force de friction qui s'applique sur eux lors de leur propagation dans l'air. Ils sont alors appelés électrons runaway, et vont produire des électrons secondaires, pouvant être eux aussi runaway, par collisions avec les molécules de l'atmosphère. L'ensemble de ce mécanisme est appelé avalanche d'électron runaway relativistes ([RREAs](#)). L'initiation des premiers électrons de haute énergie est encore sujette à discussion avec notamment l'existence de deux modèles principaux. L'un des modèles est basé sur la production d'électrons runaway thermiques dans le champ électrique inhomogène présent proche d'une tête d'éclair. Les [RREA](#) seraient alors accélérées dans ce même champ électrique. Un second modèle est basé sur le développement des [RREA](#) dans un champ électrique de grande échelle présent dans l'orage, les premiers électrons relativistes seraient alors apportés par des rayons cosmiques ou par des électrons thermiques accélérés dans une tête d'éclair.

Étant des phénomènes composés de particules ionisantes, la question de l'exposition supplémentaire générée par ces évènements pour le personnel navigant et les passagers de vols commerciaux se pose. Une première étude réalisée en 2010 par [Dwyer et al. \[2010\]](#) a montré que des fortes doses pouvaient être produites par les électrons sources des TGF. La nécessité d'évaluer précisément les risques radiologiques liés à ces évènements a donc mené Air France à entreprendre une étude sur le sujet avec la présente thèse, en association avec l'IRSN et le LPC2E.

Différents outils sont utilisés dans cette thèse pour répondre à cette question. D'abord, l'étude théorique de ces évènements et l'estimation des doses générées par les TGF à l'aide de simulations Monte Carlo est présentée dans le Chapitre 3. Une estimation de la probabilité pour un vol commercial de se trouver dans la source d'un tel évènement est présentée dans le Chapitre 4. Enfin, en parallèle de ces études théoriques, nous avons entrepris le développement d'un spectromètre gamma, afin de réaliser des mesures de gamma ray glows et de TGF, notamment par vol ballon. Ce développement ainsi que les premiers résultats sont présentés dans le Chapitre 5. Des prédictions sur les futures mesures lors des campagnes de mesures prévues sont présentées dans le Chapitre 6.

Résumé du Chapitre 2 : Méthodes

Les différentes méthodologies utilisées dans les chapitres suivants sont présentées dans ce chapitre.

D'abord, nous présentons les méthodes de calcul des doses générées par les TGF utilisées dans le Chapitre 3. Les doses équivalentes ambiantes prennent en compte le type de particules considérées, et sont exprimées en Sievert (Sv). À partir de simulation Monte Carlo principalement, nous calculons les fluences de chaque type de particule (électrons, photons et électron secondaires) lors d'un TGF. Les fluences sont ensuite multipliées par des coefficients de conversion fluences vers dose équivalente ambiante, afin d'estimer les doses associées. L'altitude de la source du TGF

Résumé en Français

étudié est fixée à 12 km (l'altitude source des TGF est estimée entre 10 et 15 km), et on fixe le nombre total de photons produits à 10^{18} . Deux types de modèles sont utilisés pour simuler la propagation des électrons dans l'air, en accord avec l'existence des deux principaux modèles proposés pour l'initiation des TGF. Le premier est un modèle Monte Carlo correspondant au développement des RREA dans le champ électrique d'une tête d'éclair. Le second correspond à une génération des premiers électrons dans une tête d'éclair, suivi du développement des RREA dans le fort champ électrique de l'orage présent sur plusieurs kilomètres. Un calcul de nombre d'électrons suivant un modèle exponentiel est alors utilisé. Concernant les photons, un code Monte Carlo est utilisé pour simuler leur propagation dans l'atmosphère, en prenant en compte trois types de collisions : l'absorption photo-électrique, la diffusion Compton et la production de pair électron-positron. Ce code est également utilisé pour estimer le nombre d'électrons secondaires produits par collision de ces photons avec des molécules de l'atmosphère.

La méthode utilisée pour estimer la probabilité qu'un vol commercial se trouve dans le faisceau d'un TGF est ensuite présentée. Le catalogue des TGF détectés par Fermi-GBM est utilisé pour calculer une carte de densité de TGF entre -26° et $+26^\circ$ de latitude. La carte de densité de TGF est corrigée afin de prendre en compte les différents biais introduits par la détection satellite, comme la dépendance en latitude de la probabilité de détection. Deux méthodes sont ensuite utilisées concernant les trajectoires des vols commerciaux. D'abord, on simule des trajectoires à partir d'une liste des plus gros aéroports du monde. Ensuite, des données de trajectoires de vols commerciaux de la compagnie Air France entre 2014 et 2016 sont utilisées. Le calcul des probabilités d'exposition est réalisé en pondérant le temps passé au dessus de chaque élément de surface du globe terrestre par la densité de TGF calculée précédemment.

Les différentes méthodes présentées dans ce chapitre sont des méthodes innovantes permettant de fournir des éléments de réponse à la problématique exposée dans cette thèse.

Résumé du Chapitre 3 : Estimation des Doses Associées aux TGF

Les résultats de l'étude théorique des doses générées par les différentes particules produites lors d'un TGF sont présentés dans ce chapitre. Les doses générées par les gamma ray glows sont estimées comme étant faibles. En effet, une exposition longue de 10 min près de la source d'une gamma ray glow délivrerait une dose de ~ 0.2 mSv, équivalente à la dose reçue lors d'une radiographie du thorax seulement. On se concentre alors dans ce chapitre aux doses délivrées par les TGF.

Concernant les électrons, les deux modèles utilisés estiment des doses approchant le Sievert, dose pour laquelle des effets immédiats comme des vomissements se manifesteraient. Ces fortes doses sont cependant estimées comme étant générées sur des régions restreintes typiquement de ~ 200 m de rayon. On estime que les photons génèreraient des doses plus faibles, avec l'estimation de la dose maximale délivrée de $90 \mu\text{Sv}$. Une telle dose reçue lors d'un vol long-courrier moyen de 10 h par un passager représenterait une augmentation de son exposition par un facteur 2.5.

Les résultats obtenus dans ce chapitre sont cohérents avec les précédentes estimations faites par [Dwyer et al. \[2010\]](#). De nouvelles informations sont apportées par notre étude en estimant les doses délivrées par les électrons en fonction de l'altitude dans l'avalanche, en utilisant deux modèles différents. Concernant le second modèle, on fait également varier les paramètres suivants : le champ électrique, la longueur de l'avalanche, l'altitude de la source ainsi que le diamètre de la source du TGF. Nous estimons également l'impact de la cabine de l'avion sur les doses délivrées. En modélisant la cabine d'un avion par une épaisseur de 7 mm d'aluminium, on estime que la dose délivrée par les électrons ne serait atténuée que de $\sim 30\%$. Concernant les photons, 90% des photons avec une énergie >1 MeV traversent complètement une telle épaisseur, et on peut donc estimer qu'il n'y aurait pas d'impact significatif sur la dose délivrée.

En conclusion, les photons génèreraient des doses faibles (<1 mSv). Les élec-

trons seraient, au contraire, source de doses beaucoup plus fortes, approchant voire atteignant 1 Sv, selon le modèle et les paramètres utilisés. Ces fortes doses seraient cependant générées sur des régions limitées, dans un rayon de ~ 200 m. Une précise évaluation des risques liés à ces événements est donc nécessaire, au vu de l'association d'un événement peu probable mais engendrant un fort impact négatif sur la santé. Une estimation de la probabilité qu'un vol commercial se trouve dans un rayon de 200 m autour de la source d'un TGF est donc présentée dans le prochain chapitre.

Résumé du Chapitre 4 : Risque pour un Vol Commercial d'être Touché par un TGF

Comme présenté dans le chapitre précédent, de fortes doses sont estimées comme étant générées par les électrons sources des TGF. Une estimation précise de la probabilité qu'un vol commercial se trouve à proximité de la source d'un TGF est donc nécessaire et présentée dans ce chapitre. La carte de densité de TGF présentée dans le Chapitre 2 est utilisée avec la simulation de trajectoires d'avions, puis avec les trajectoires réelles de vols commerciaux de la compagnie Air France.

Avec les trajectoires d'avion simulées, nous estimons d'abord la probabilité qu'un avion soit touché sur une trajectoire particulièrement exposée. La trajectoire dont la probabilité est la plus élevée est celle entre les aéroports d'Atlanta (Géorgie, USA) et Santiago (Chili). La probabilité sur cette trajectoire correspond à un vol touché par un TGF tous les 1.5 million de vols, correspondant à 1 vol tous les 250 ans en prenant en compte 16 vols par jour sur cette trajectoire. À partir de cette estimation d'une trajectoire particulièrement exposée, on estime la valeur haute du nombre de vols touchés par un TGF dans le monde, en supposant que toutes les trajectoires soient autant exposées. On obtient que 6.7 vols par an seraient touchés par un TGF dans le monde. En utilisant, au contraire, différentes probabilités en fonction des trajectoires et en prenant en compte le type de vol (long, moyen ou court courrier), on réduit cette estimation à un vol touché tous les 1.6 ans seulement.

En utilisant les données réelles de vol de la compagnie Air France, on estime qu'un vol de la compagnie serait touché par un TGF tous les 390 ans. La trajectoire la plus exposée pour la compagnie est la trajectoire entre les aéroports de Paris (France) et Johannesburg (Afrique du Sud), sur laquelle un vol serait touché tous les 3,600 ans. Ces données sont également utilisées pour trouver la distance minimale en temps réel entre un TGF et un avion Air France. Cette distance minimale est de 36 km, atteinte pour un seul des vols étudiés.

De fortes hypothèses ont été utilisées pour cette étude, par exemple l'utilisation d'une carte de densité basée sur les TGF détectés par satellite, qui supposent une fluence suffisante, ainsi que la non-prise en compte de l'altitude des TGF et des avions. Ces hypothèses ont cependant été faites afin de permettre une première estimation de ces probabilités. Les TGF de faible fluence ont été le sujet de plusieurs études, mais aucune conclusion précise n'a été faite pour estimer leur proportion. Si les TGF non détectables par satellite se trouvent être une grande proportion des TGF produits sur Terre, les résultats de cette étude ne seraient cependant pas impactés fortement puisque les fortes doses ont été estimées principalement pour les TGF détectable par satellite. L'étude de l'erreur faite en ne prenant pas en compte les altitudes des TGF et des avions résulte en une surestimation d'un facteur ~ 10 des probabilités dans ce chapitre.

En conclusion, on estime que la probabilité qu'un vol commercial se trouve à moins de 200 m de la source d'un TGF est faible. Un tel événement se produirait moins de tous les 2 ans, pour la méthode dont le but était d'estimer une limite haute, et moins de tous les 16 ans pour une estimation sur la globalité du transport aérien commercial.

Résumé du Chapitre 5 : Spectromètre Gamma : Développement et Mesures

Le développement instrumental d'un nouveau spectromètre gamma dont l'objectif est de détecter les gamma ray glows et les TGF au plus près des sources a été réalisé en parallèle des deux études présentées dans les chapitres précédents. Les glows étant des évènements plus fréquents que les TGF, et ayant été récemment détectées à 20 km d'altitude, leur détection et étude sont l'objectif principal de cet instrument. Cependant, l'instrument a été développé afin de pouvoir également détecter les TGF. En effet, des mesures au plus près des sources apporteraient de nouvelles informations nécessaires pour répondre aux questions encore présentes à propos de ces évènements, notamment avec des mesures sous ballon.

L'instrument est basé sur la détection des particules par des scintillateurs. Deux types de scintillateurs sont utilisés, un scintillateur BGO et un scintillateur plastique. L'association de ces deux types de scintillateurs permet d'identifier 3 types de particules : les photons, les électrons et les neutrons. Pour chaque particule détectée, le spectromètre fournit son temps d'arrivée, à 100 ns près en temps UTC, ainsi que son énergie, via la valeur de l'intégrale du pulse électrique associé. La fréquence maximale de comptes détectés par le détecteur est de 1 MHz, ce qui permet de pouvoir détecter le fort flux de particules produit par les TGF. Des énergies jusqu'à 30 MeV peuvent être mesurées. La haute précision UTC permet également la comparaison avec des données de réseaux éclairs, particulièrement intéressant pour la détection des TGF. Une méthode de discrimination appelée PSD est utilisée pour discriminer les neutrons des photons. Cette méthode a déjà été testée par vol ballon en temps clair, en mesurant le fond de rayonnement principalement dû aux rayons cosmiques.

Une adaptation du détecteur, développé d'abord comme étant complètement autonome, pour voler sous ballon dans des campagnes sans possibilité de récupération de l'instrument à la fin du vol a été réalisée. Deux différents modes de fonction-

nement ont été implémentés pour réduire la quantité de données produite. Un système de détection d'évènement en temps réel, par analyse du rayonnement mesuré, est également implémenté.

Plusieurs vols sous Ballon Léger Dilatable (BLD) ont été réalisés par temps clair afin de tester l'instrument en altitude. Ces vols ont permis de confirmer le bon fonctionnement de l'instrument, d'appliquer la méthode de PSD, et de détecter des effets instrumentaux indésirables. Ces effets instrumentaux sont maintenant ignorés par le système de détection d'évènement, afin de ne pas polluer les données envoyées au sol par satellite.

En conclusion, le spectromètre gamma développé pendant la thèse est capable de détecter les gamma ray glows et les TGF, et participera à différentes campagnes ballon telles que Stratéole-2, présentée dans ce chapitre, pour lesquelles les résultats sont attendus et prometteurs, considérant les caractéristiques des vols prévus.

Résumé du Chapitre 6 : Prédiction sur les mesures futures avec XStorm

Dans ce chapitre, une étude sur la possibilité de détection de gamma ray glows en fonction de l'altitude source et de l'altitude du détecteur est réalisée. Pour cela, nous utilisons le code Monte Carlo présenté dans le Chapitre 2 pour simuler la propagation de photons dans l'atmosphère. Des altitudes entre 1 et 20 km sont utilisées pour l'altitude de la source, et entre 0 et 30 km pour l'altitude du détecteur. Des vitesses initiales dirigées vers le haut et dirigées vers le bas sont utilisées, afin de modéliser différentes structures de charges présentes dans les orages. Les résultats sont présentés dans les Figures 6.1 et 6.2.

La mesure d'une gamma ray glow décrite par Kelley et al. [2015] est ensuite utilisée pour appliquer les résultats de la première partie de ce chapitre. Un flux de 1,100 électrons/cm²/s à la fin de l'avalanche d'électrons est reporté. Nous présentons le modèle que nous avons développé pour simuler le flux de photons produits par cette

Résumé en Français

avalanche, basé sur une distribution exponentielle des électrons dans l'avalanche. Une discrétisation d'Euler est utilisée pour propager les particules, avec un pas de temps de $0.1 \mu\text{s}$. Le flux de photons obtenu est de $340 \text{ photons/cm}^2/\text{s}$. Ce résultat est vérifié par les mesures décrites dans [Kelley et al. \[2015\]](#), ainsi que par un calcul analytique simple.

Ce flux de photons est ensuite utilisé avec les résultats de la première partie du chapitre, afin d'estimer les altitudes des sources qui seront détectables pendant les vols de la campagne Stratéole-2, qui se trouveront à 20 km. Nous montrons que seules les sources à partir de 14 km d'altitude seront détectables.

La détection des **TGF** étant un objectif secondaire du développement de XStorm, nous estimons ensuite la probabilité qu'un **TGF** soit détecté lors de la prochaine campagne. Pour cela, on utilise la carte de densité de **TGF** calculée pour un champ de vue de XStorm de 20 km autour de la source. Les trajectoires des 8 vols de la campagne de validation de Stratéole-2 réalisée en 2019 permettent de calculer la probabilité moyenne de détecter un **TGF** sur un tel vol. On estime finalement qu'un **TGF** pourra être détecté tous les ~ 2.3 vols sur cette campagne. Puisque nous prévoyons de livrer 4 instruments qui voleront sous 4 ballons différents, on estime pouvoir détecter ~ 2 **TGF** lors de la prochaine campagne.

Enfin, XStorm sera adapté pour réaliser des mesures au sol, en utilisant des scintillateurs avec une plus grande surface de détection ($3''$ de côté). Pour cela, on a évalué la possibilité de détecter une gamma ray glow en fonction de l'altitude du sol et de la source, en prenant en compte la radioactivité naturelle due au sol. La détection au sol est limitée par l'épaisseur de l'atmosphère entre le détecteur et la source, ainsi que par le rayonnement naturel émis par le sol. Pour les différentes altitudes du détecteur au sol, seules les sources de moins de ~ 3 km au dessus du détecteur sont détectables.

Résumé du Chapitre 7 : Conclusion Générale

La problématique exposée dans cette thèse est l'incertitude concernant l'importance de la contribution des doses générées par les TGF à l'exposition des personnels navigants. La diversité des outils utilisés dans cette thèse a permis d'apporter des éléments de réponse à cette problématique. D'abord, les simulations numériques de propagations de particules dans l'atmosphère terrestre ont permis d'estimer les doses générées par les TGF. Des doses supérieures aux limites annuelles des personnels navigants sont générées seulement par les électrons runaway à l'origine des TGF, mais dans des régions restreintes, de ~ 200 m de rayon. Ensuite, nous avons réalisé une étude statistique afin d'évaluer la probabilité qu'un vol commercial se trouve dans le faisceau d'électrons d'un TGF. En utilisant des données satellites de Fermi-GBM ainsi que des trajectoires de vols commerciaux simulées et réelles, cette probabilité est estimée comme étant faible, limitant à un avion tous les ~ 300 ans le nombre d'avions se retrouvant dans cette situation. Enfin, le développement instrumental d'un spectromètre gamma en parallèle de ces études a été entrepris. Les caractéristiques de ce détecteur ont été choisies afin de permettre au mieux la détection des gamma ray glows et des TGF à proximité.

Le développement de l'instrument étant finalisé, le détecteur est maintenant prêt à voler en conditions orageuses afin de pouvoir détecter ces événements. Des campagnes sont déjà prévues, OREO et Stratéole-2 notamment, pour lesquelles on a estimé la détectabilité des gamma ray glows et des TGF en fonction des configurations. Les futures mesures sont très prometteuses et permettront de continuer à apporter des éléments de réponse concernant la problématique de cette thèse, ainsi qu'à apporter de nouvelles informations sur la physique liée à ces événements, comme le lien entre les TGF, les gamma ray glows, le rayonnement cosmique et le système d'électrification des orages par exemple.

Appendices

XStorm packet encapsulation

XStorm front-end electronics produce data packets every second. Two channels are available on XStorm. Each detector produce one data frame per second. For each detector, the data packet contains several information as the time of the beginning of the corresponding frame, the presence or not of the PPS signal in the last second, the number of particles detected and reported in the frame, the sum of the integrals of the pulses reported in the frame, and for each particle the two integrals described in Figure 5.3 and the arrival time of the particle in respect with the time of the beginning of the frame.

Every 10 seconds, a frame containing housekeeping information is produced. The information available is the SiPM temperatures, SiPM voltages, and the board temperature. The board temperature can be useful in case of the absence of the PPS signal. In fact, the FPGA oscillator is subject to a weak frequency drift as a function of the temperature. This drift has been estimated to be $\sim 0.2 \mu\text{s}$ per second, at 20°C . On duration of the order of one second, the drift is not important, but on several seconds, we can need to correct the arrival time of the particles to get a μs resolution UTC, thus the board temperature data supplied.

The packet encapsulation follows the datagrams presented in Figure A.1.

Bibliography

- Abbasi, R. et al. (2017). The bursts of high energy events observed by the telescope array surface detector. *Physics Letters A*, 381(32):2565–2572. (Cited on pages 7 and 82.)
- Abbasi, R. U. et al. (2018). Gamma ray showers observed at ground level in coincidence with downward lightning leaders. *Journal of Geophysical Research: Atmospheres*, 123(13):6864–6879. (Cited on pages 7 and 82.)
- Albrechtsen, K. H., Østgaard, N., Berge, N., and Gjesteland, T. (2019). Observationally weak TGFs in the RHESSI data. *J. Geophys. Res.*, 124(1):287–298. (Cited on page 8.)
- Babich, L. P. (2006). Generation of neutrons in giant upward atmospheric discharges. *Soviet Journal of Experimental and Theoretical Physics Letters*, 84(6):285–288. (Cited on page 5.)
- Balanis, C. A. (1989). *Advanced Engineering Electromagnetics*, page 670. John Wiley. (Cited on page 31.)
- Bazelyan, E. and Raizer, Y. (2000). *Lightning Physics and Lightning Protection*. Taylor & Francis. (Cited on page 32.)
- Becker, H., Alexander, J., Atreya, S., Bolton, S., Brennan, M., Brown, S., Guillaume, A., Guillot, T., Ingersoll, A., Levin, S., Lunine, J., Aglyamov, Y., and Steffes, P. (2020). Small lightning flashes from shallow electrical storms on Jupiter. *Nature*, 584. (Cited on page 3.)
- Belz, J. W. et al. (2020). Observations of the origin of downward terrestrial gamma-ray flashes. *Journal of Geophysical Research: Atmospheres*, 125(23):e2019JD031940. e2019JD031940 10.1029/2019JD031940. (Cited on pages 7 and 82.)

Bibliography

- Berge, N. and Celestin, S. (2019). Constraining downward terrestrial gamma ray flashes using ground-based particle detector arrays. *Geophysical Research Letters*, 46(14):8424–8430. (Cited on page 7.)
- Berge, N., Celestin, S., Garnung, M. B., Xu, W., Marshall, R. A., and Cummer, S. A. (2022). Modeling low-frequency radio emissions from terrestrial gamma ray flash sources. *Journal of Geophysical Research: Atmospheres*, 127(5):e2021JD036040. e2021JD036040 2021JD036040. (Cited on page 15.)
- Berge, N. L., Celestin, S., Xu, W., Marshall, R. A., and Cummer, S. A. (2019). Constraining source properties using TGF-associated radio emissions. *AGU Fall Meeting, San Francisco, CA, USA*, (AE44A-06). (Cited on page 35.)
- Berger, M., Hubbell, J., Seltzer, S., Chang, J., Coursey, J., Sukumar, R., Zucker, D., , and Olsen, K. (2010). XCOM: Photon cross section database (version 1.5). *National Institute of Standards and Technology*. (Cited on pages xv and 37.)
- Berger, M. J., Coursey, J. S., Zucker, M. A., and Chang, J. (2005). Stopping-Power and Range Tables for Electrons, Protons, and Helium Ions. *Natl. Instit. of Stand. and Technol.* (Cited on pages 32 and 63.)
- Bertrand, G. H., Hamel, M., Normand, S., and Sguerra, F. (2015). Pulse shape discrimination between (fast or thermal) neutrons and gamma rays with plastic scintillators: State of the art. *Nuclear Instruments and Methods in Physics Research Section A: Accelerators, Spectrometers, Detectors and Associated Equipment*, 776:114–128. (Cited on page 88.)
- Bottollier-Depois, J.-F., Beck, P., Latocha, M., Mares, V., Matthiä, D., Rühm, W., and Wissmann, F. (2012). *Comparison of Codes Assessing Radiation Exposure of Aircraft Crew due to Galactic Cosmic*. Number 173. Luxembourg. (Cited on page 19.)
- Bottollier-Depois, J. F., Blanchard, P., Clairand, I., Dessarps, P., Fuller, N., Lantos,

- P., Saint-Lô, D., and Trompier, F. (2007). An operational approach for aircraft crew dosimetry: the SIEVERT system. *Radiation Protection Dosimetry*, 125(1-4):421–424. (Cited on page 19.)
- Bottollier-Depois, J.-F., Chau, Q., Bouisset, P., Kerlau, G., Plawinski, L., and Lebaron-Jacobs, L. (2000). Assessing exposure to cosmic radiation during long-haul flights. *Radiation Research*, 153(5):526 – 532. (Cited on page 59.)
- Bowers, G. S. (2017). *Observations of Positron and Neutron Emissions from Terrestrial Gamma-ray Flashes*. PhD thesis, UC Santa Cruz. (Cited on page 38.)
- Bowers, G. S., Smith, D. M., Kelley, N. A., Martinez-McKinney, G. F., Cummer, S. A., Dwyer, J. R., Heckman, S., Holzworth, R. H., Marks, F., Reasor, P., Gamache, J., Dunion, J., Richards, T., and Rassoul, H. K. (2018). A terrestrial gamma-ray flash inside the eyewall of hurricane Patricia. *J. Geophys. Res.*, 123(10):4977–4987. (Cited on pages 7 and 82.)
- Bowers, G. S., Smith, D. M., Martinez-McKinney, G. F., Kamogawa, M., Cummer, S. A., Dwyer, J. R., Wang, D., Stock, M., and Kawasaki, Z. (2017). Gamma ray signatures of neutrons from a terrestrial gamma ray flash. *Geophysical Research Letters*, 44(19):10,063–10,070. (Cited on pages 5, 50 and 82.)
- Briggs, M. S., Connaughton, V., Wilson-Hodge, C., Preece, R. D., Fishman, G. J., Kippen, R. M., Bhat, P. N., Paciesas, W. S., Chaplin, V. L., Meegan, C. A., von Kienlin, A., Greiner, J., Dwyer, J. R., and Smith, D. M. (2011). Electron-positron beams from terrestrial lightning observed with Fermi GBM. *Geophysical Research Letters*, 38(2). (Cited on page 6.)
- Briggs, M. S., Fishman, G. J., Connaughton, V., Bhat, P. N., Paciesas, W. S., Preece, R. D., Wilson-Hodge, C., Chaplin, V. L., Kippen, R. M., von Kienlin, A., Meegan, C. A., Bissaldi, E., Dwyer, J. R., Smith, D. M., Holzworth, R. H., Grove, J. E., and Chekhtman, A. (2010). First results on terrestrial gamma ray flashes

Bibliography

- from the Fermi Gamma-ray Burst Monitor. *J. Geophys. Res.*, 115(A7):A07323. (Cited on pages [xiii](#), [5](#), [6](#) and [7](#).)
- Briggs, M. S., Xiong, S., Connaughton, V., Tierney, D., Fitzpatrick, G., Foley, S., Grove, J. E., Chekhtman, A., Gibby, M., Fishman, G. J., McBreen, S., Chaplin, V. L., Guiriec, S., Layden, E., Bhat, P. N., Hughes, M., Greiner, J., Kienlin, A., Kippen, R. M., Meegan, C. A., Paciesas, W. S., Preece, R. D., Wilson-Hodge, C., Holzworth, R. H., and Hutchins, M. L. (2013). Terrestrial gamma-ray flashes in the Fermi era: Improved observations and analysis methods. *J. Geophys. Res.*, 118(6):3805–3830. (Cited on pages [8](#), [40](#), [42](#) and [43](#).)
- Brooks, F. D., Pringle, R. W., and Funt, B. L. (1960). Pulse shape discrimination in a plastic scintillator. *IRE Transactions on Nuclear Science*, 7(2/3):35–38. (Cited on page [87](#).)
- Carlson, B., Lehtinen, N., and Inan, U. (2010). Neutron production in terrestrial gamma ray flashes. *Journal of Geophysical Research*, 115:1–24. (Cited on page [5](#).)
- Celestin, S. and Pasko, V. P. (2010). Soft collisions in relativistic runaway electron avalanches. *J. Phys. D: Appl. Phys.*, 43(31):315206. (Cited on page [32](#).)
- Celestin, S. and Pasko, V. P. (2011). Energy and fluxes of thermal runaway electrons produced by exponential growth of streamers during the stepping of lightning leaders and in transient luminous events. *J. Geophys. Res.*, 116:A03315. (Cited on pages [14](#), [31](#), [32](#) and [52](#).)
- Celestin, S., Xu, W., and Pasko, V. P. (2012). Terrestrial gamma ray flashes with energies up to 100 MeV produced by nonequilibrium acceleration of electrons in lightning. *Journal of Geophysical Research: Space Physics*, 117(A5). (Cited on page [12](#).)
- Celestin, S., Xu, W., and Pasko, V. P. (2015). Variability in fluence and spectrum

- of high-energy photon bursts produced by lightning leaders. *J. Geophys. Res.*, 120(12):10,712–10,723. (Cited on pages 14, 32, 33 and 75.)
- Chilingarian, A. (2011). Particle bursts from thunderclouds: Natural particle accelerators above our heads. *Phys. Rev. D*, 83. (Cited on page 3.)
- Chilingarian, A., Mailyan, B., and Vanyan, L. (2012). Recovering of the energy spectra of electrons and gamma rays coming from the thunderclouds. *Atmospheric Research*, 114-115:1–16. (Cited on page 3.)
- Chilingarian, A., Mkrtchyan, H., Karapetyan, G., Chilingaryan, S., Sargsyan, B., and Arestakesyan, A. (2019). Catalog of 2017 thunderstorm ground enhancement (tge) events observed on aragats. *Scientific Reports*, 9:6253. (Cited on page 10.)
- Christian, H. J., Blakeslee, R. J., Boccippio, D. J., Boeck, W. L., Buechler, D. E., Driscoll, K. T., Goodman, S. J., Hall, J. M., Koshak, W. J., Mach, D. M., and Stewart, M. F. (2003). Global frequency and distribution of lightning as observed from space by the optical transient detector. *Journal of Geophysical Research: Atmospheres*, 108(D1):ACL 4–1–ACL 4–15. (Cited on pages xiii, 2 and 44.)
- Cieślak, M. J., Gamage, K. A. A., and Glover, R. (2019). Critical review of scintillating crystals for neutron detection. *Crystals*, 9(9). (Cited on page 88.)
- Clairand, I., Fuller, N., Bottollier-Depois, J.-F., and Trompier, F. (2009). The sievert system for aircrew dosimetry. *Radiation Protection Dosimetry*, (136 (4)). (Cited on pages xiv, 19 and 20.)
- Coleman, L. M. and Dwyer, J. R. (2006). Propagation speed of runaway electron avalanches. *Geophys. Res. Lett.*, 33(11):L11810. (Cited on pages 13, 14, 34 and 113.)
- Cook, A. F., I., Duxbury, T. C., and Hunt, G. E. (1979). A lower limit on the top of Jupiter’s haze layer. *Nature*, 280(5725):780–781. (Cited on page 3.)

Bibliography

- Cramer, E. S., Dwyer, J. R., Arabshahi, S., Vodopyanov, I. B., Liu, N., and Rassoul, H. K. (2014). An analytical approach for calculating energy spectra of relativistic runaway electron avalanches in air. *Journal of Geophysical Research (Space Physics)*, 119(9):7794–7823. (Cited on page 12.)
- Cummer, S. A., Briggs, M. S., Dwyer, J. R., Xiong, S., Connaughton, V., Fishman, G. J., Lu, G., Lyu, F., and Solanki, R. (2014). The source altitude, electric current, and intrinsic brightness of terrestrial gamma ray flashes. *Geophys. Res. Lett.*, 41(23):8586–8593. (Cited on pages 5, 31 and 75.)
- Cummer, S. A., Lu, G., Briggs, M. S., Connaughton, V., Xiong, S., Fishman, G. J., and Dwyer, J. R. (2011). The lightning-TGF relationship on microsecond timescales. *Geophys. Res. Lett.*, 38(14):L14810. (Cited on pages 31 and 75.)
- Cummer, S. A., Lyu, F., Briggs, M. S., Fitzpatrick, G., Roberts, O. J., and Dwyer, J. R. (2015). Lightning leader altitude progression in terrestrial gamma-ray flashes. *Geophys. Res. Lett.*, 42(18):7792–7798. (Cited on pages 5, 31 and 75.)
- Dwyer, J. (2007). Relativistic breakdown in planetary atmospheres. *Physics of Plasmas*, 14:042901–042901. (Cited on page 16.)
- Dwyer, J. R. (2003). A fundamental limit on electric fields in air. *Geophys. Res. Lett.*, 30(20):2055. (Cited on pages xv, 13, 16, 34 and 35.)
- Dwyer, J. R. (2008). Source mechanisms of terrestrial gamma-ray flashes. *J. Geophys. Res.*, 113(D10):D10103. (Cited on pages 14 and 16.)
- Dwyer, J. R. (2012). The relativistic feedback discharge model of terrestrial gamma ray flashes. *Journal of Geophysical Research: Space Physics*, 117(A2). (Cited on page 16.)
- Dwyer, J. R. and Babich, L. P. (2011). Low-energy electron production by relativistic runaway electron avalanches in air. *Journal of Geophysical Research: Space Physics*, 116(A9). (Cited on page 12.)

- Dwyer, J. R. and Cummer, S. A. (2013). Radio emissions from terrestrial gamma-ray flashes. *Journal of Geophysical Research: Space Physics*, 118(6):3769–3790. (Cited on page 16.)
- Dwyer, J. R., Rassoul, H. K., Al-Dayeh, M., Caraway, L., Wright, B., Chrest, A., Uman, M. A., Rakov, V. A., Rambo, K. J., Jordan, D. M., Jerauld, J., and Smyth, C. (2004). A ground level gamma-ray burst observed in association with rocket-triggered lightning. *Geophysical Research Letters*, 31(5). (Cited on page 7.)
- Dwyer, J. R., Schaal, M. M., Cramer, E., Arabshahi, S., Liu, N., Rassoul, H. K., Hill, J. D., Jordan, D. M., and Uman, M. A. (2012). Observation of a gamma-ray flash at ground level in association with a cloud-to-ground lightning return stroke. *Journal of Geophysical Research: Space Physics*, 117(A10). (Cited on page 7.)
- Dwyer, J. R. and Smith, D. M. (2005). A comparison between Monte Carlo simulations of runaway breakdown and terrestrial gamma-ray flash observations. *Geophysical Research Letters*, 32(22). (Cited on pages xiii, 4, 5 and 9.)
- Dwyer, J. R., Smith, D. M., and Cummer, S. A. (2012). High-Energy Atmospheric Physics: Terrestrial Gamma-Ray Flashes and Related Phenomena. *Space Science Reviews*, 173(1-4):133–196. (Cited on pages 12, 14 and 110.)
- Dwyer, J. R., Smith, D. M., Hazelton, B. J., Grefenstette, B. W., Kelley, N. A., Lowell, A. W., Schaal, M. M., and Rassoul, H. K. (2015). Positron clouds within thunderstorms. *Journal of Plasma Physics*, 81(4):475810405. (Cited on page 5.)
- Dwyer, J. R., Smith, D. M., Uman, M. A., Saleh, Z., Grefenstette, B., Hazelton, B., and Rassoul, H. K. (2010). Estimation of the fluence of high-energy electron bursts produced by thunderclouds and the resulting radiation doses received in aircraft. *J. Geophys. Res.*, 115(D9). (Cited on pages 4, 17, 25, 30, 36, 60, 63, 123, 129 and 131.)
- Eack, K. B. and Beasley, W. H. (2015). Long-duration X-ray emissions observed

Bibliography

- in thunderstorms. *Journal of Geophysical Research (Atmospheres)*, 120(14):6887–6897. (Cited on page 10.)
- Eack, K. B., Beasley, W. H., Rust, W. D., Marshall, T. C., and Stolzenburg, M. (1996). Initial results from simultaneous observation of x-rays and electric fields in a thunderstorm. *Journal of Geophysical Research: Atmospheres*, 101(D23):29637–29640. (Cited on page 9.)
- EljenTechnology (2021). *EljenTechnology.com*. <https://eljentechnology.com/products/plastic-scintillators/ej-276> [Accessed: 2022-05]. (Cited on page 90.)
- Enoto, T., Wada, Y., Furuta, Y., Nakazawa, K., T., Y., Okuda, K., Makishima, K., Sato, M., Sato, Y., Nakano, T., D., U., and H., T. (2017). Photonuclear reactions triggered by lightning discharge. *Nature*, 551:481–484. (Cited on pages 5, 50, 82 and 97.)
- Fischer, G., Desch, M., Zarka, P., Kaiser, M., Gurnett, D., Kurth, W., Macher, W., Rucker, H., Lecacheux, A., Farrell, W., and Cecconi, B. (2006). Saturn lightning recorded by Cassini/RPWS in 2004. *Icarus*, 183(1):135–152. (Cited on page 3.)
- Fisher, F. A., Plumer, J. A., and Perala, R. A. (1999). Lightning protection of aircraft. *Lightning Technol.* (Cited on page 68.)
- Fishman, G. J., Bhat, P. N., Mallozzi, R., Horack, J. M., Koshut, T., Kouveliotou, C., Pendleton, G. N., Meegan, C. A., Wilson, R. B., and Paciesas, W. S. (1994). Discovery of Intense Gamma-Ray Flashes of Atmospheric Origin. *Science*, 264(5163):1313–1316. (Cited on pages 3, 4 and 6.)
- Fishman, G. J., Briggs, M. S., Connaughton, V., Bhat, P. N., Paciesas, W. S., von Kienlin, A., Wilson-Hodge, C., Kippen, R. M., Preece, R., and Meegan, C. A. (2011). Temporal properties of the terrestrial gamma-ray flashes from the Gamma-

- Ray Burst Monitor on the Fermi Observatory. *J. Geophys. Res.*, 116(A7):A07304.
(Cited on pages 5 and 93.)
- flightconnections.com (2021). *flightconnections.com*. <https://www.flightconnections.com/flights-from-mex-to-bog> [Accessed: 2021-08].
(Cited on page 74.)
- flights.com (2021). *flights.com*. <https://www.flights.com> [Accessed: 2021-08].
(Cited on page 69.)
- Gjesteland, T., Østgaard, N., Collier, A. B., Carlson, B. E., Cohen, M. B., and Lehtinen, N. G. (2011). Confining the angular distribution of terrestrial gamma ray flash emission. *Journal of Geophysical Research: Space Physics*, 116(A11).
(Cited on page 8.)
- Gjesteland, T., Østgaard, N., Laviola, S., Miglietta, M. M., Arnone, E., Marisaldi, M., Fuschino, F., Collier, A. B., Fabr o, F., and Montanya, J. (2015). Observation of intrinsically bright terrestrial gamma ray flashes from the mediterranean basin. *J. Geophys. Res.*, 120(23):12,143–12,156. (Cited on pages 5, 7, 31 and 62.)
- Goto, Y. and Narita, K. (1992). Observations of winter lightning to an isolate tower. *Journal of Atmospheric Electricity*, 12(1):57–60. (Cited on page 11.)
- Grodzicka-Kobylka, M., Szczesniak, T., Moszyński, M., Brylew, K., Swiderski, L., Valiente-Dobón, J. J., Schotanus, P., Grodzicki, K., and Trzaskowska, H. (2020). Fast neutron and gamma ray pulse shape discrimination in EJ-276 and EJ-276G plastic scintillators. *Journal of Instrumentation*, 15(3):P03030. (Cited on page 88.)
- Grodzicka-Kobylka, M., Szczesniak, T., Swiderski, L., Brylew, K., Moszyński, M., Valiente-Dobón, J. J., Schotanus, P., Grodzicki, K., Mazerewicz, P., Szymanowski, J., and Mianowska, Z. (2021). Comparison of detectors with pulse shape discrimination capability for simultaneous detection of gamma-rays, slow and fast

Bibliography

- neutrons. *Nuclear Instruments and Methods in Physics Research A*, 1019:165858. (Cited on page 88.)
- Gurevich, A., Milikh, G., and Roussel-Dupre, R. (1992). Runaway electron mechanism of air breakdown and preconditioning during a thunderstorm. *Physics Letters A*, 165:463–468. (Cited on page 13.)
- Gurnett, D. A., Kurth, W. S., Hospodarsky, G. B., Persoon, A. M., Averkamp, T. F., Cecconi, B., Lecacheux, A., Zarka, P., Canu, P., Cornilleau-Wehrlin, N., Galopeau, P., Roux, A., Harvey, C., Louarn, P., Bostrom, R., Gustafsson, G., Wahlund, J.-E., Desch, M. D., Farrell, W. M., Kaiser, M. L., Goetz, K., Kellogg, P. J., Fischer, G., Ladreiter, H.-P., Rucker, H., Alleyne, H., and Pedersen, A. (2005). Radio and plasma wave observations at Saturn from Cassini’s approach and first orbit. *Science*, 307(5713):1255–1259. (Cited on page 3.)
- Hazelton, B. J., Grefenstette, B. W., Smith, D. M., Dwyer, J. R., Shao, X.-M., Cummer, S. A., Chronis, T., Lay, E. H., and Holzworth, R. H. (2009). Spectral dependence of terrestrial gamma-ray flashes on source distance. *Geophysical Research Letters*, 36(1). (Cited on page 8.)
- heavens above.com (2021). *heavens-above.com*. <https://heavens-above.com/orbit.aspx?satid=33053> [Accessed: 2021-08]. (Cited on page 41.)
- Hess, V. F. (1912). Über Beobachtungen der durchdringenden Strahlung bei sieben Freiballonfahrten. *Phys. Z.*, 13:1084–1091. (Cited on page 17.)
- ICRP (2007). *The 2007 Recommendations of the International Commission on Radiological Protection*. Number ICRP Publication 103. (Cited on page 28.)
- ICRP (2016). *Radiological protection from cosmic radiation in aviation*. Number ICRP Publication 132. (Cited on page 18.)
- Kelley, N., Smith, D., Dwyer, J., Splitt, M., Lazarus, S., Martinez-McKinney, F., Hazelton, B., Grefenstette, B., Lowell, A., and Rassoul, H. (2015). Relativistic

- electron avalanches as a thunderstorm discharge competing with lightning. *Nature Communications*, 6. (Cited on pages xxii, 9, 10, 11, 35, 50, 81, 110, 113, 114, 116, 117, 118, 120, 121, 125, 135 and 136.)
- Kim, Y.-K., Santos, J. P., and Parente, F. (2000). Extension of the binary-encounter-dipole model to relativistic incident electrons. *Phys. Rev. A*, 62(5):052710. (Cited on page 32.)
- Knoll, G. F. (1989). *Radiation detection and measurement / Glenn F. Knoll*. Wiley New York, 2nd ed. edition. (Cited on page 87.)
- Lehtinen, N. G. (2000). *Relativistic runaway electrons above thunderstorms*. PhD thesis, STANFORD UNIVERSITY. (Cited on page 52.)
- Lindanger, A., Marisaldi, M., Sarria, D., Østgaard, N., Lehtinen, N., Skeie, C. A., Mezentzev, A., Kochkin, P., Ullaland, K., Yang, S., Genov, G., Carlson, B. E., Köhn, C., Navarro-Gonzalez, J., Connell, P., Reglero, V., and Neubert, T. (2021). Spectral analysis of individual terrestrial gamma-ray flashes detected by ASIM. *Journal of Geophysical Research: Atmospheres*, 126(23):e2021JD035347. e2021JD035347 2021JD035347. (Cited on pages 7 and 8.)
- Lu, G., Blakeslee, R. J., Li, J., Smith, D. M., Shao, X.-M., McCaul, E. W., Buechler, D. E., Christian, H. J., Hall, J. M., and Cummer, S. A. (2010). Lightning mapping observation of a terrestrial gamma-ray flash. *Geophys. Res. Lett.*, 37(11):L11806. (Cited on page 5.)
- Lu, G., Cummer, S. A., Li, J., Han, F., Smith, D. M., and Grefenstette, B. W. (2011). Characteristics of broadband lightning emissions associated with terrestrial gamma ray flashes. *Journal of Geophysical Research: Space Physics*, 116(A3). (Cited on page 5.)
- Mailyan, B. G., Briggs, M. S., Cramer, E. S., Fitzpatrick, G., Roberts, O. J., Stanbro, M., Connaughton, V., McBreen, S., Bhat, P. N., and Dwyer, J. R. (2016).

Bibliography

- The spectroscopy of individual terrestrial gamma-ray flashes: Constraining the source properties. *J. Geophys. Res.*, 121(11):11,346–11,363. (Cited on pages 5, 7, 8, 31 and 62.)
- Mailyan, B. G., Xu, W., Celestin, S., Briggs, M. S., Dwyer, J. R., Cramer, E. S., Roberts, O. J., and Stanbro, M. (2019). Analysis of individual terrestrial gamma-ray flashes with lightning leader models and Fermi Gamma-ray Burst Monitor data. *J. Geophys. Res.*, 124(8):7170–7183. (Cited on pages 5, 7, 8, 31 and 62.)
- Marisaldi, M., Galli, M., Labanti, C., Østgaard, N., Sarria, D., Cummer, S. A., Lyu, F., Lindanger, A., Campana, R., Ursi, A., Tavani, M., Fuschino, F., Argan, A., Trois, A., Pittori, C., and Verrecchia, F. (2019). On the high-energy spectral component and fine time structure of terrestrial gamma ray flashes. *Journal of Geophysical Research: Atmospheres*, 124(14):7484–7497. (Cited on page 17.)
- Marisaldi, M., Smith, D. M., Brandt, S., Briggs, M. S., Budtz-Jørgensen, C., Campana, R., Carlson, B. E., Celestin, S., Connaughton, V., and Cummer, S. A. (2015). High-energy radiation from thunderstorms and lightning with LOFT. *arXiv e-prints*. (Cited on page 5.)
- Marisaldi, M., Tavani, M., Argan, A., Trois, A., Giuliani, A., Labanti, C., Fuschino, F., Bulgarelli, A., Longo, F., and Barbiellini, G. (2010). Gamma-ray Localization of Terrestrial Gamma-ray Flashes by AGILE. In *AGU Fall Meeting Abstracts*, volume 2010, pages AE11A–0330. (Cited on pages 5 and 6.)
- Marshall, T. C., McCarthy, M. P., and Rust, W. D. (1995). Electric field magnitudes and lightning initiation in thunderstorms. *Journal of Geophysical Research: Atmospheres*, 100(D4):7097–7103. (Cited on page 13.)
- McCarthy, M. and Parks, G. K. (1985). Further observations of X-rays inside thunderstorms. *Geophysical Research Letters*, 12(6):393–396. (Cited on pages xiv, 8 and 10.)

- McTague, L. E., Cummer, S. A., Briggs, M. S., Connaughton, V., Stanbro, M., and Fitzpatrick, G. (2015). A lightning-based search for nearby observationally dim terrestrial gamma ray flashes. *J. Geophys. Res.*, 120(23):12,003–12,017. (Cited on page 8.)
- Millikan, R. A. and Bowen, I. S. (1926). High Frequency Rays of Cosmic Origin I. Sounding Balloon Observations at Extreme Altitudes. *Physical Review*, 27(4):353–361. (Cited on page 17.)
- Moss, G. D., Pasko, V. P., Liu, N., and Veronis, G. (2006). Monte Carlo model for analysis of thermal runaway electrons in streamer tips in transient luminous events and streamer zones of lightning leaders. *Journal of Geophysical Research: Space Physics*, 111(A2). (Cited on page 14.)
- Neubert, T., Ostgaard, N., Reglero, V., Blanc, E., Chanrion, O., Oxborrow, C., Orr, A., Tacconi, M., Hartnack, O., and Bhandari, D. (2019). The ASIM Mission on the international space station. *Space Science Reviews*, 215. (Cited on page 65.)
- ONSEMI (2021). *Introduction to the Silicon Photomultiplier*. <https://www.onsemi.com/pub/Collateral/AND9770-D.PDF> [Accessed: 2022-05]. (Cited on page 90.)
- Østgaard, N., Albrechtsen, K. H., Gjesteland, T., and Collier, A. (2015). A new population of terrestrial gamma-ray flashes in the RHESSI data. *Geophys. Res. Lett.*, 42(24):10,937–10,942. (Cited on page 8.)
- Østgaard, N., Christian, H. J., Grove, J. E., Sarria, D., Mezentsev, A., Kochkin, P., Lehtinen, N., Quick, M., Al-Nussirat, S., Wulf, E., Genov, G., Ullaland, K., Marisaldi, M., Yang, S., and Blakeslee, R. J. (2019a). Gamma ray glow observations at 20-km altitude. *Journal of Geophysical Research: Atmospheres*, 124(13):7236–7254. (Cited on pages 11, 23, 50, 80, 81, 117 and 121.)
- Østgaard, N., Gjesteland, T., Hansen, R. S., Collier, A. B., and Carlson, B. (2012).

Bibliography

- The true fluence distribution of terrestrial gamma flashes at satellite altitude. *J. Geophys. Res.*, 117(A3). (Cited on page 8.)
- Østgaard, N., Gjesteland, T., Stadsnes, J., Connell, P. H., and Carlson, B. (2008). Production altitude and time delays of the terrestrial gamma flashes: Revisiting the Burst and Transient Source Experiment spectra. *J. Geophys. Res.*, 113(A2):A02307. (Cited on pages 36 and 110.)
- Østgaard, N., Neubert, T., Reglero, V., Ullaland, K., Yang, S., Genov, G., Marisaldi, M., Mezentsev, A., Kochkin, P., Lehtinen, N., Sarria, D., Qureshi, B. H., Solberg, A., Maiorana, C., Albrechtsen, K., Budtz-Jørgensen, C., Kuvvetli, I., Christiansen, F., Chanrion, O., Heumesser, M., Navarro-Gonzalez, J., Connell, P., Eyles, C., Christian, H., and Al-nussirat, S. (2019b). First 10 months of TGF observations by ASIM. *J. Geophys. Res.*, 124(24):14024–14036. (Cited on page 6.)
- ourairports.com (2021). *ourairports.com*. <http://ourairports.com/data/airports.csv> [Accessed: 2021-08]. (Cited on page 45.)
- Pallu, M., Celestin, S., Trompier, F., and Klerlein, M. (2021). Estimation of Radiation Doses Delivered by Terrestrial Gamma Ray Flashes Within Leader Based Production Models. *Journal of Geophysical Research (Atmospheres)*, 126(8):e33907. (Cited on pages xvi, xvii, xviii, 49, 51, 53, 55, 56, 58, 64, 75 and 81.)
- Pelliccioni, M. (2000). Overview of fluence-to-effective dose and fluence-to-ambient dose equivalent conversion coefficients for high energy radiation calculated using the FLUKA code. *Radiation Protection Dosimetry*, 88:279–297. (Cited on pages xv, 28 and 30.)
- Rakov, V. A. and Uman, M. A. (2007). *Lightning: Physics and Effects*, page 670. Cambridge University Press. (Cited on page 11.)

- Regener, E. and Pfozter, G. (1934). Intensity of the Cosmic Ultra-Radiation in the Stratosphere with the Tube-Counter. *Nature*, 134:325. (Cited on page 102.)
- Roberts, O. J., Fitzpatrick, G., Stanbro, M., McBreen, S., Briggs, M. S., Holzworth, R. H., Grove, J. E., Chekhtman, A., Cramer, E. S., and Mailyan, B. G. (2018). The first Fermi-GBM terrestrial gamma ray flash catalog. *Journal of Geophysical Research: Space Physics*, 123(5):4381–4401. (Cited on pages 39, 72 and 77.)
- Roussel-Dupré, R. and Gurevich, A. V. (1996). On runaway breakdown and upward propagating discharges. *Journal of Geophysical Research: Space Physics*, 101(A2):2297–2311. (Cited on page 12.)
- Rutjes, C., Diniz, G., Ferreira, I. S., and Ebert, U. (2017). Tgf afterglows: A new radiation mechanism from thunderstorms. *Geophysical Research Letters*, 44(20):10,702–10,712. (Cited on pages 5 and 82.)
- Saint-Gobain (2021). *Efficiency Calculations for Selected Scintillators*. <https://www.crystals.saint-gobain.com/radiation-detection-scintillators/crystal-scintillators/bgo-bismuth-germanate> [Accessed: 2022-05]. (Cited on page 102.)
- Sarria, D., Kochkin, P., Østgaard, N., Lehtinen, N., Mezentsev, A., Marisaldi, M., Carlson, B. E., Maiorana, C., Albrechtsen, K., Neubert, T., Reglero, V., Ullaland, K., Yang, S., Genov, G., Qureshi, B. H., Budtz-Jørgensen, C., Kuvvetli, I., Christiansen, F., Chanrion, O., Heumesser, M., Dimitriadou, K., Navarro-González, J., Connell, P., and Eyles, C. (2019). The First Terrestrial Electron Beam Observed by the Atmosphere-Space Interactions Monitor. *J. Geophys. Res.*, 124(12):10497–10511. (Cited on page 62.)
- Sato, T. (2015). Analytical model for estimating terrestrial cosmic ray fluxes nearly anytime and anywhere in the world: Extension of PARMA/EXPACS. *PLOS ONE*, 10(12):1–33. (Cited on pages 102 and 106.)

Bibliography

- Shao, X.-M., Hamlin, T., and Smith, D. M. (2010). A closer examination of terrestrial gamma-ray flash-related lightning processes. *J. Geophys. Res.*, 115(9):A00E30. (Cited on page 5.)
- Skeltved, A. B., Østgaard, N., Carlson, B., Gjesteland, T., and Celestin, S. (2014). Modeling the relativistic runaway electron avalanche and the feedback mechanism with GEANT4. *Journal of Geophysical Research: Space Physics*, 119(11):9174–9191. (Cited on pages 16 and 34.)
- Skeltved, A. B., Østgaard, N., Mezentsev, A., Lehtinen, N., and Carlson, B. (2017). Constraints to do realistic modeling of the electric field ahead of the tip of a lightning leader. *J. Geophys. Res.*, 122(15):8120–8134. (Cited on page 32.)
- Smith, D. M., Bowers, G. S., Kamogawa, M., Wang, D., Ushio, T., Ortberg, J., Dwyer, J. R., and Stock, M. (2018). Characterizing upward lightning with and without a terrestrial gamma ray flash. *Journal of Geophysical Research: Atmospheres*, 123(20):11,321–11,332. (Cited on pages 80 and 81.)
- Smith, D. M., Buzbee, P., Aron-Dine, S., Kelley, N. A., Holzworth, R. H., Hutchins, M. L., and Dwyer, J. R. (2014). Constraining faint terrestrial gamma-ray flashes with stacking analyses. *Fall Meeting, AGU, San Francisco, Calif., 17 Dec. 2014*, (AE33A-07). (Cited on page 8.)
- Smith, D. M., Buzbee, P., Kelley, N. A., Infanger, A., Holzworth, R. H., and Dwyer, J. R. (2016). The rarity of terrestrial gamma-ray flashes: 2. RHESSI stacking analysis. *Journal of Geophysical Research: Atmospheres*, 121(19):11,382–11,404. (Cited on page 8.)
- Smith, D. M., Dwyer, J. R., Hazelton, B. J., Grefenstette, B. W., Martinez-McKinney, G. F. M., Zhang, Z. Y., Lowell, A. W., Kelley, N. A., Splitt, M. E., Lazarus, S. M., Ulrich, W., Schaal, M., Saleh, Z. H., Cramer, E., Rassoul, H., Cummer, S. A., Lu, G., Shao, X.-M., Ho, C., Hamlin, T., Blakeslee, R. J., and

- Heckman, S. (2011a). A terrestrial gamma ray flash observed from an aircraft. *J. Geophys. Res.*, 116(D20). (Cited on pages 7, 44 and 82.)
- Smith, D. M., Dwyer, J. R., Hazelton, B. J., Grefenstette, B. W., Martinez-McKinney, G. F. M., Zhang, Z. Y., Lowell, A. W., Kelley, N. A., Splitt, M. E., Lazarus, S. M., Ulrich, W., Schaal, M., Saleh, Z. H., Cramer, E., Rassoul, H. K., Cummer, S. A., Lu, G., and Blakeslee, R. J. (2011b). The rarity of terrestrial gamma-ray flashes. *Geophysical Research Letters*, 38(8). (Cited on page 44.)
- Smith, D. M., Kelley, N. A., Buzbee, P., Infanger, A., Splitt, M., Holzworth, R. H., and Dwyer, J. R. (2020). Special classes of terrestrial gamma ray flashes from RHESSI. *Journal of Geophysical Research: Atmospheres*, 125(20):e2020JD033043. e2020JD033043 10.1029/2020JD033043. (Cited on page 62.)
- Smith, D. M., Lopez, L. I., Lin, R. P., and Barrington-Leigh, C. P. (2005). Terrestrial Gamma-Ray Flashes Observed up to 20 MeV. *Science*, 307(5712):1085–1088. (Cited on page 6.)
- Stanley, M. A., Shao, X.-M., Smith, D. M., Lopez, L. I., Pongratz, M. B., Harlin, J. D., Stock, M., and Regan, A. (2006). A link between terrestrial gamma-ray flashes and intracloud lightning discharges. *Geophys. Res. Lett.*, 33(6):L06803. (Cited on page 5.)
- statista.com (2021). *statista.com*. <https://www.statista.com/statistics/564769/airline-industry-number-of-flights/> [Accessed: 2021-08]. (Cited on pages xvi, 45 and 69.)
- Takeuti, T., Nakano, M., Nagatani, M., and Nakada, H. (1973). On lightning discharges in winter thunderstorms. *J. Meteor. Soc. Japan*, 51:494–496. (Cited on page 11.)
- Tavani, M., Argan, A., Pesoli, A., Palma, F., Gerardin, S., Bagatin, M., Trois, A., Picozza, P., Benvenuti, P., Flamini, E., Marisaldi, M., Pittori, C., and Giommi,

Bibliography

- P. (2013). Possible effects on avionics induced by terrestrial gamma-ray flashes. *Natural Hazards and Earth System Sciences*, 13:7023-. (Cited on page 16.)
- Tavani, M., Marisaldi, M., Labanti, C., Fuschino, F., Argan, A., Trois, A., Giommi, P., Colafrancesco, S., Pittori, C., Palma, F., Trifoglio, M., Gianotti, F., Bulgarelli, A., Vittorini, V., Verrecchia, F., Salotti, L., Barbiellini, G., Caraveo, P., Cattaneo, P. W., and Zanello, D. (2011). Terrestrial gamma-ray flashes as powerful particle accelerators. *Physical review letters*, 106:018501. (Cited on page 17.)
- Torii, T., Sugita, T., Kamogawa, M., Watanabe, Y., and Kusunoki, K. (2011). Migrating source of energetic radiation generated by thunderstorm activity. *Geophysical Research Letters*, 38(24). (Cited on page 81.)
- Trompier, F., Fuller, N., Bonnotte, F., Desmaris, G., Musso, A., Cale, E., and Bottollier-Depois, J.-F. (2014). Impact of TGF for aircrew dosimetry: analysis of continuous onboard measurements. *EGU*, (14895). (Cited on page 65.)
- Tsuchiya, H., Enoto, T., Yamada, S., Yuasa, T., Kawaharada, M., Kitaguchi, T., Kokubun, M., Kato, H., Okano, M., Nakamura, S., et al. (2007). Detection of high-energy gamma rays from winter thunderclouds. *Physical review letters*, 99(16):165002. (Cited on page 9.)
- Tsuchiya, H., Enoto, T., Yamada, S., Yuasa, T., Nakazawa, K., Kitaguchi, T., Kawaharada, M., Kokubun, M., Kato, H., Okano, M., and Makishima, K. (2011). Long-duration γ ray emissions from 2007 and 2008 winter thunderstorms. *Journal of Geophysical Research (Atmospheres)*, 116(D9):D09113. (Cited on page 9.)
- U.S. Standard Atmosphere, . (1976). *United States Committee on Extension to the Standard Atmosphere*. NOAA - SIT 76-1562. National Oceanic and Atmospheric Administration. (Cited on page 37.)
- Wada, Y., Enoto, T., Nakamura, Y., Furuta, Y., Yuasa, T., Nakazawa, K., Morimoto, T., Sato, M., Matsumoto, T., Yonetoku, D., Sawano, T., Sakai, H., Kamo-

- gawa, M., Ushio, T., Makishima, K., and Tsuchiya, H. (2019). Gamma-ray glow preceding downward terrestrial gamma-ray flash. *Communications Physics*, 2:67. (Cited on pages 5, 11, 80 and 81.)
- Wilkerson, J., Jacobson, M., A, M., Balasubramanian, S., Wayson, R., G, F., Naiman, A., and Lele, S. (2010). Analysis of emission data from global commercial aviation: 2004 and 2006. *ATMOSPHERIC CHEMISTRY AND PHYSICS*, 2010:2945–2983. (Cited on pages 45 and 71.)
- Wilson, C. T. R. (1924). The electric field of a thundercloud and some of its effects. *Proceedings of the Physical Society of London*, 37(1):32D–37D. (Cited on page 2.)
- Yair, Y., Fischer, G., Simões, F., Renno, N., and Zarka, P. (2008). *Updated Review of Planetary Atmospheric Electricity*, pages 29–49. Springer New York, New York, NY. (Cited on page 3.)
- Zarka, P., Farrell, W., Kaiser, M., Blanc, E., and Kurth, W. (2004). Study of solar system planetary lightning with LOFAR. *Planetary and Space Science*, 52(15):1435–1447. (Cited on page 3.)

Mélody PALLU

Étude des doses pour le personnel navigant de l'aviation civile liées aux flashs gamma terrestres et autres phénomènes électriques atmosphériques

Résumé :

Les orages sont le lieu de production d'évènements de haute énergie découverts dans les années 90, appelés flashs gamma terrestres (TGF), et gamma ray glows. Les TGF sont des bouffées de photons gamma, détectables par satellite, dont la durée est de moins de 100 μ s. Les énergies des photons produits peuvent atteindre ~ 40 MeV. Quant aux gamma ray glows, elles sont des augmentations du rayonnement de fond dans les orages, sur des durées plus longues (quelques secondes à dizaines de minutes) mais générant des flux de photons beaucoup moins importants. Ces deux types d'évènements sont produits par les mêmes mécanismes physiques impliquant des électrons de haute énergie, appelés avalanches d'électrons runaway relativistes.

Ces évènements sont produits à des altitudes entre 10 et 15 km, coïncidant avec les altitudes des vols commerciaux. Dans cette thèse, nous adressons le problème d'une exposition supplémentaire due à ces évènements pour les passagers et le personnel navigant de l'aviation civile. Nous avons entrepris différents moyens d'étude afin d'apporter une réponse à cette problématique, en s'appuyant sur diverses méthodes. D'abord, l'estimation théorique des doses générées par les TGF à l'aide de simulation numériques montre que de fortes doses sont générées par les électrons source, cependant dans des régions compactes. Dans un second temps, une étude statistique estime que la probabilité qu'un avion commercial soit touché par la source d'un TGF, en utilisant des données satellites et des trajectoires d'avion, est faible. Enfin, nous présentons le développement d'un spectromètre gamma et les prédictions des mesures futures concernant les TGF et les gamma ray glows.

Mots clés : TGF, doses, aviation civile, spectrométrie gamma, électrodynamique atmosphérique de haute énergie

Estimation of the radiation risk to aircrew and aircraft passengers associated with atmospheric electricity events such as Terrestrial Gamma ray Flashes and Gamma ray Glows

Summary:

Thunderstorms produce high-energy events discovered in the 1990's, named terrestrial gamma ray flashes (TGFs) and gamma ray glows. TGFs are bursts of gamma rays, detectable by satellite, which last less than 100 μ s. The energy of produced photons can reach ~ 40 MeV. Concerning gamma ray glows, they are increases of the background radiation level in thunderstorms, with longer durations (from seconds to tens of minutes) but generating photon fluxes less important. Both events are produced by the same physical processes implying high-energy electrons, named relativistic runaway electron avalanches (RREAs).

Those events are produced between 10 and 15 km of altitude, being coincident with commercial flight altitudes. In this thesis, we address the possible additional exposure due to these events for passengers and commercial aircrews. We performed several set of tools to answer this problematic. First, the theoretical estimation of radiation doses delivered by TGFs using numerical simulations shows that high doses are generated by source electrons, however in compact regions. Then, a statistical study estimates the probability for an aircraft to be hit by a TGF, using satellite data and flight routes, is weak. Finally, we present the development of a gamma ray spectrometer to detect these events in close proximity and predictions on the future measurements that will be performed for TGFs and gamma ray glows.

Keywords: TGFs, doses, aircrew, gamma spectrometry, high energy atmospheric electrodynamic



Laboratoire de Physique et Chimie
de l'Environnement et de l'Espace (LPC2E),
3A Avenue de la Recherche Scientifique,
45071, Orléans, CEDEX 02, France



